Fully Kinetic Ion Models for Magnetized Plasma Simulations

by

Benjamin J. Sturdevant

B.S., University of Wisconsin, 2009

M.S., University of Colorado, 2012

A thesis submitted to the

Faculty of the Graduate School of the

University of Colorado in partial fulfillment

of the requirements for the degree of

Doctor of Philosophy

Department of Applied Mathematics

2016

This thesis entitled:
Fully Kinetic Ion Models for Magnetized Plasma Simulations
written by Benjamin J. Sturdevant
has been approved for the Department of Applied Mathematics

Prof. Scott E. Parker

Dr. Yang Chen

Date

The final copy of this thesis has been examined by the signatories, and we find that both the content and the form meet acceptable presentation standards of scholarly work in the above mentioned discipline.

Sturdevant, Benjamin J. (Ph.D., Applied Mathematics)

Fully Kinetic Ion Models for Magnetized Plasma Simulations

Thesis directed by Prof. Scott E. Parker

This thesis focuses on the development of simulation models, based on fully resolving the gyro-motion of ions with the Lorentz force equations of motion, for studying low-frequency phenomena in well-magnetized plasma systems. Such models, known as fully kinetic ion models, offer formal simplicity over higher order gyrokinetic ion models and may provide an important validation tool or replacement for gyrokinetic ion models in applications where the gyrokinetic ordering assumptions are in question. Methods for dealing with the added difficulty of resolving the short time scales associated with the ion gyro-motion in fully kinetic ion models are explored with the use of graphics processing units (GPUs) and advanced time integration algorithms, including sub-cycling, orbit averaging and variational integrators. Theoretical work is performed to analyze the effects of the ion Bernstein modes, which are known to cause difficulties in simulations based on fully kinetic ion models. In addition, the first simulation results for the ion temperature gradient driven instability in toroidal geometry using a fully kinetic ion model are presented. Finally, during the course of this work, a method for analyzing the effects of a finite time step size and spatial grid in the δf approach to the particle-in-cell method was developed for the first time. This method was applied to an implicit time integration scheme and has revealed some unusual numerical properties related to the δf method.

Dedication

I dedicate this thesis to my wife, Robin.

Acknowledgements

I would like to first express my sincere gratitude to my thesis advisor Scott Parker. Scott has been immensely supportive and has taught me much about what it means to be a good scientist. A special thanks to Tom Manteuffel for his insightful questions and interest in this work and to Yang Chen for his willingness to share his vast knowledge of numerical algorithms. I would like to thank the rest of my committee for their helpful comments and the unique prospectives they brought to this research.

I have many family members to thank for their support and encouragement. I thank my parents, Dean and Cathy Sturdevant, and my siblings Kiara, Shevonne, Sam, Steve, Victoria, and Isaac. I thank Milly Hoffman (Granny) who has demonstrated an unparalleled example of a good work ethic throughout my life. I thank Nevin and Tammy Werron and Sue and Sanjib Bhuyan for their interest in my education and career development. Finally, I thank my wife Robin for her patience and understanding throughout this process.

Contents

Chapter

Tables

Table

Figures

Figure

Chapter 1

Introduction

1.1 Background

There are several characteristics of plasmas which make their study extremely challenging. A plasma consists of a large number of charged particles interacting through mean, self-generated fields, yielding immensely complex behaviors. Phenomena in a plasma is nonlinear and characterized by time and spatial scales spanning many orders of magnitude. A further challenge comes from the fact that collisions often play only a weak role in plasma dynamics. In weakly collisional plasmas, there are important effects due to variations in the particle velocities which are not captured in a fluid description. To account for velocity variations, the appropriate setting in which to study a plasma is a six dimensional phase space, consisting of three spatial dimensions and three velocity dimensions. Models which treat a plasma as a fluid over phase space, i.e. including both space and velocity coordinates as independent variables, are known as kinetic models. Analytical methods alone are generally insufficient to investigate behaviors in kinetic plasma models. Computer simulations have therefore emerged as an indispensable tool.

An application area which has driven much of the research in plasma physics is the potential for harnessing energy from thermonuclear fusion. The pursuit of fusion energy is one of the most ambitious programs of scientific research and development that has been attempted. Production of controlled fusion reactions requires the generation of a very hot plasma in a laboratory setting. Confining such a plasma is a challenging endeavour, however, since direct contact with material surfaces would rapidly cool the plasma, making fusion processes unsustainable. One promising

method for plasma confinement is to impose a strong, external magnetic field on the plasma, which restricts the motion of the particles to be mainly parallel to the field. To confine the particles along the magnetic field, field lines are configured to follow helical paths, winding around a toroidal surface. This closed, toroidal magnetic field configuration is the basis for tokamak and stellarator confinement devices.

On long time scales, for which collisional effects play an important role, a plasma will relax to a unique thermodynamic equilibrium state in which all particle species can be described by spatially homogeneous Maxwellian distribution functions, as is guaranteed by the Boltzmann H theorem [1]. On time scales which are short compared to collisional times, however, magnetically confined plasmas can exist in a wide variety of stationary states, or metaequilibria, which may include density and temperature gradients [2, 3]. The inhomogeneities of these states are a source of free energy from which instabilities may arise. Instabilities in confined plasmas can lead to turbulence, causing particles and energy to escape from the system at rates much greater than models of ordinary collisional processes predict [4, 5]. Understanding the physical mechanisms causing the onset of turbulence and the resulting transport levels has, therefore, been a high priority area of magnetic confinement fusion research.

The most violent pressure driven instabilities in a magnetically confined plasma can be described by single fluid magnetohydrodynamic (MHD) theory. Turbulent transport, however, is known to subsist even when the MHD modes have been suppressed. This turbulence originates from a set of modes known as microinstabilities, which are characterized by frequencies that are small compared with the gyro-frequencies, long length scales parallel to the magnetic field, and perpendicular length scales comparable to the gyro-radii. There are many factors which make the study of microinstabilities and the resulting turbulence challenging, the most obvious being the intrinsically nonlinear nature of turbulence. Even in the linear regime, however, microinstabilities are strongly influenced by kinetic effects, including wave-particle resonances and finite Larmor radius (FLR) effects. The complex geometries of plasma confinement devices adds further difficulty for theoretical work.

A major breakthrough in the field of microinstabilities was the development of gyrokinetics (GK) [6–8]. The GK approach takes advantage of the large scale separations and anisotropies characteristic of magnetized plasmas to analytically reduce the plasma kinetic model. A physical picture of the GK model is to treat gyrating particles as slowly drifting rings of charge in spatially varying fields. Mathematically, the dynamics of the plasma kinetic equations are simplified by averaging over the gyro-phase and dropping terms that are higher order in the GK ordering assumptions. The gyro-averaging procedure eliminates the time scale associated with the gyro-motion while retaining important FLR effects. Turbulence simulations based on the nonlinear GK equations are the subject of intensive computational studies. The development of particle simulation methods for the nonlinear GK equations [9,10] and the availability of modern powerful computers have allowed, for the first time, turbulent transport simulations which produce qualitatively similar results to that observed in present day plasma confinement experiments.

1.2 Motivation for Fully Kinetic Ion Models

A key advantage for using GK models for the ions in a plasma, as opposed to models based on the original kinetic equations, is that the analytical elimination of the ion gyration time-scale in GK models relaxes time step size constraints in numerical implementations. Gyrokinetic theory, however, is based on a number of ordering assumptions which must hold to ensure the accuracy of the model. In certain applications where GK ordering assumptions may be in question, for example, in the tokamak edge pedestal region where gradient scale lengths can be comparable to the ion gyroradius, higher order terms may be important. Extending GK ion models for such applications, however, can be non-trivial and leads to challenging numerical implementations [11–14]. As GK is begin relied upon in more areas of application, it becomes important to understand the basic limitations of the ordering assumptions.

There has been recent interest in developing models using the full Lorentz force equations of motion for ions [15–17]. Such models, known as fully kinetic (FK) ion models, offer formal simplicity over GK models and can provide an important validation tool or replacement for GK ion

models in applications where higher order terms may be important. A further motivation for the development of FK ion models is a modern progression of using GK codes for simulating physical phenomena whose resolution requires time step sizes close to that needed to fully resolve the ion gyro-motion. The use of FK ion models, therefore, may be feasible without a large increase in computational effort from what is already used in modern GK codes. Finally, algorithmic advances in particle integration schemes in addition to recent efforts in optimizing particle-in-cell (PIC) algorithms for modern computing architectures, such as graphics processing units (GPUs), holds promise for handling the more expensive particle integration of the FK ion model [18–21].

1.3 Overview of Thesis

In this thesis, we explore the development of FK ion models to be used in the study of low-frequency phenomena in well magnetized plasmas. Chapter 2 introduces the plasma physics background of relevance to this work in addition to the PIC simulation method. Chapter 3 presents FK ion and GK ion models for a microinstability due to equilibrium gradients in the ion temperature known as the ion temperature gradient (ITG) instability. A rigorous comparison of the linear dispersion properties of both models is performed and numerical simulation results based on the δf PIC method are presented for the FK ion model, assuming a uniform magnetic field. Finally, it is shown how the model can be extended for magnetic fields with weak inhomogeneities, which is of use for models in the more realistic toroidal geometry. Chapter 4 explores advanced time integration algorithms and the implementation of the FK ion model on GPUs. In addition, theory is derived to analyze the ion Bernstein modes, which were found to cause difficulties in simulations using the FK ion model. The work from Chapter 4 has been published in [22]. In Chapter 5, we present a FK ion simulation model for the ITG instability in a toroidal magnetic field. The first simulation results using such a model are presented and compared to the global gyrokinetic GEM code. In Chapter 6, we derive for the first time a method for analyzing the effects of a finite time step size and spatial grid in the δf PIC method. A complete analysis is performed for an implicit time integration scheme and is compared to an equivalent full-f analysis and implementation.

The work from Chapter 6 has been published in [23]. Chapter 7 provides conclusions and further discussion.

Chapter 2

Basic Concepts

2.1 Plasma Physics Basics

Fundamentally, a plasma is an ionized gas; that is, one in which a fraction of the constituent atoms have dissociated into positively charged ions and negatively charged electrons. Commonly referred to as the "fourth state of matter", the tendency for a plasma to generate and respond to electromagnetic forces yields complex properties distinct from matter found in solid, liquid, or gaseous states. In a plasma, charge separations between ions and electrons, in addition to flows of charged particles, generate electric and magnetic fields. The electric and magnetic fields in turn dictate the motion of the charged particles making up the plasma, resulting in a large range of intricate behaviors.

Any gas containing charged particles could, in a sense, be considered a plasma. Research in plasma physics, however, focuses on a specific regime in which charged particles occur in sufficient number to make the collective effects of self-generated fields important for statistical properties, yet the particles are dilute enough that short range forces due to near-neighbor particles (i.e. collisions) play only a weak role. In addition, a plasma is considered to consist of equal numbers of positive and negative charges, as is the case when a neutral gas is ionized. In such a system, the mobility of the electrons prevents local bunching of same sign charges. Electrons are attracted to regions of high ion concentrations, quickly streaming in to shield their electric field from the bulk of the plasma. Similarly, strong electric fields resulting from high concentrations of electrons are prevented by repulsion.

The tendency for a plasma to electrically neutralize itself on a macroscopic scale is known as "quasi-neutrality" and is an important characteristic of the plasmas we consider. Quantitative descriptions of the neutralizing property of plasmas can be found in a number of plasma textbooks including [2, 24–26], the key result being the definition of the electron Debye length, denoted λ_D. The electron Debye length characterizes the alteration of the Coulomb force in a plasma. In a vacuum, the electrostatic potential due to a particle of charge q varies with the distance from the particle, r, as

$$\phi(r) = \frac{1}{4\pi\epsilon_0}\frac{q}{r}, \tag{2.1}$$

where $\epsilon_0 = 8.854 \times 10^{-12}$ F/m is the permittivity of free space. For a charged particle immersed in a plasma, however, shielding properties due mainly to the mobility of electrons gives rise to an exponentially decaying potential as

$$\phi(r) = \frac{1}{4\pi\epsilon_0}\frac{q}{r}e^{-\frac{r}{\lambda_D}}.$$

An expression for λ_D may be given in terms of the electron density n_e, electron temperature T_e, Boltzmann's constant $k = 1.381 \times 10^{-23}$ J/°K, the elementary charge $e = 1.602 \times 10^{-19}$ C, and ϵ_0 as

$$\lambda_D = \left(\frac{\epsilon_0 k T_e}{n_e e^2}\right)^{1/2}.$$

As the electron density increases, λ_D decreases, as there are more electrons available for shielding. This expression also indicates that the thermal motion of the electrons is necessary to establish a shielding region of finite width, since taking $T_e \to 0$ yields a shielding cloud that has collapsed into an infinitesimal region around the test charge. To be in the quasi-neutral regime requires the dimensions of the plasma system, characterized by length L, to be much larger than the electron Debye length

$$L \gg \lambda_D,$$

meaning the bulk of the plasma does not experience large electric fields due to high concentrations of like charges.

Related to the electron Debye length is a dimensionless parameter Λ, known as the plasma parameter, which is defined as

$$\Lambda = \frac{4}{3}\pi\lambda_D^3 n_e.$$

It is clear that this parameter gives the typical number of electrons found in a sphere with a radius of electron Debye length. Perhaps more importantly, Λ gives a measure of the dominance of collective effects in a plasma over discrete particle effects. This becomes more transparent when Λ is expressed as

$$\Lambda = \frac{4}{3}\pi\left(\frac{\epsilon_0 kT_e}{e^2 n_e^{1/3}}\right)^{3/2}. \tag{2.2}$$

The average distance between particles is given by $a \equiv n_e^{1/3}$, and the corresponding electrostatic potential energy between two particles at this distance can be obtained from Eq.(2.1). Furthermore, from statistical physics, the kinetic energy of a particle is of order kT_e. Hence the expression in parentheses in Eq.(2.2) scales with the ratio of mean kinetic energy to inter-particle potential energy within a Debye sphere. A plasma is said to be strongly coupled when $\Lambda \ll 1$, characterized by large inter-particle potentials and sparsely populated Debye spheres. Such plasmas tend to have low temperatures and high densities with collisions playing a dominant role. On the other hand, a weakly coupled plasma is one for which $\Lambda \gg 1$. Plasma physics focuses almost exclusively on the weakly coupled state.

2.2 A Microscopic Description of a Plasma

Maxwell's equations form the foundation of the classical theory of electricity and magnetism and are therefore central to the study of plasmas. This is a set of four equations describing the generation of electric and magnetic fields due to charge and current densities in addition to changes

of each other. In differential form, Maxwell's equations are

$$\nabla \cdot \mathbf{E} = \frac{\rho}{\epsilon_0} \tag{2.3}$$

$$\nabla \times \mathbf{E} = -\frac{\partial \mathbf{B}}{\partial t} \tag{2.4}$$

$$\nabla \cdot \mathbf{B} = 0 \tag{2.5}$$

$$\nabla \times \mathbf{B} = \mu_0 \left(\mathbf{J} + \epsilon_0 \frac{\partial \mathbf{E}}{\partial t} \right), \tag{2.6}$$

where $\mathbf{E}$ is the electric field, $\mathbf{B}$ the magnetic field, ρ and $\mathbf{J}$ the charge and current densities, respectively, and $\mu_0 = 4\pi \times 10^{-7}$ N/A^2 the permeability of free space. As given, Maxwell's equations are not closed. Remaining to be specified are the charge and current densities. Plasma physics models may be viewed as a closure of Maxwell's equations, specifying ρ and $\mathbf{J}$ in terms of $\mathbf{E}$ and $\mathbf{B}$.

To begin the task of closure, we index each species of charged particles in a plasma, e.g. protons and electrons, with α and assume that the α^{th} species consists of N_α particles of charge and mass q_α and m_α, respectively. In addition, the individual particles in species α are indexed by $p_\alpha = 1, ..., N_\alpha$. The state of the p_α^{th} particle at a given time is completely specified by a position vector $\mathbf{x}_{p_\alpha} \in \mathbb{R}^3$ and velocity vector $\mathbf{v}_{p_\alpha} \in \mathbb{R}^3$. Given this information for each particle, the state of the plasma system is described by microscopic distribution functions, $\mathcal{F}_\alpha^M$, for each species, defined over a six dimensional phase space $(\mathbf{x}, \mathbf{v}) \in \mathbb{R}^6$. An explicit representation for $\mathcal{F}_\alpha^M$ is formally given by the so called Klimontovich-Dupree representation as

$$\mathcal{F}_\alpha^M(\mathbf{x}, \mathbf{v}) = \sum_{p_\alpha=1}^{N_\alpha} \delta_X^3(\mathbf{x} - \mathbf{x}_{p_\alpha}) \delta_V^3(\mathbf{v} - \mathbf{v}_{p_\alpha}), \tag{2.7}$$

where δ_X and δ_V are dimensional Dirac delta functions with units of length^{-1} and velocity^{-1} respectively. Note that the integration of Eq.(2.7) over all phase space gives

$$\int_{\mathbb{R}^3 \times \mathbb{R}^3} \mathcal{F}_\alpha^M(\mathbf{x}, \mathbf{v}) d^3x d^3v = N_\alpha.$$

Closure of Maxwell's equations is straight forward, provided the complete particle information is known. In particular, the charge and current densities can be computed from $\mathcal{F}_\alpha^M$ by taking

moments with respect to the velocity variable. We have

$$\rho^M(\mathbf{x}) = \sum_\alpha q_\alpha \int_{\mathbb{R}^3} \mathcal{F}_\alpha^M(\mathbf{x},\mathbf{v}) d^3v \tag{2.8}$$

$$\mathbf{J}^M(\mathbf{x}) = \sum_\alpha q_\alpha \int_{\mathbb{R}^3} \mathbf{v}\mathcal{F}_\alpha^M(\mathbf{x},\mathbf{v}) d^3v, \tag{2.9}$$

where we have used the superscript M to indicate that these quantities were calculated from the microscopic distribution function. Finally, to be determined is the evolution of $\mathcal{F}_\alpha^M$ in time. From classical electrodynamics, the motion of the p_α^{th} particle due to an electromagnetic field is governed by the Lorentz force together with Newton's second law of motion

$$\frac{d}{dt}\mathbf{x}_{p_\alpha} = \mathbf{v}_{p_\alpha} \tag{2.10}$$

$$\frac{d}{dt}\mathbf{v}_{p_\alpha} = \frac{q_\alpha}{m_\alpha}\left(\mathbf{E}^M(\mathbf{x}_{p_\alpha}) + \mathbf{v}_{p_\alpha} \times \mathbf{B}^M(\mathbf{x}_{p_\alpha})\right), \tag{2.11}$$

where again, the superscript M is to indicate that the fields come from solving Eqs.(2.3)–(2.6) with the sources terms given by $\rho = \rho^M$ and $\mathbf{J} = \mathbf{J}^M$. By formally taking the partial derivative with respect to time of Eq.(2.7), the chain rule together with properties of the Dirac delta function and Eqs.(2.10)–(2.11) yields

$$\frac{\partial \mathcal{F}_\alpha^M}{\partial t} + \mathbf{v}\cdot\nabla\mathcal{F}_\alpha^M + \mathbf{a}_\alpha^M \cdot \nabla_{\mathbf{v}}\mathcal{F}_\alpha^M = 0, \tag{2.12}$$

where

$$\mathbf{a}_\alpha^M = \frac{q_\alpha}{m_\alpha}\left(\mathbf{E}^M + \mathbf{v}\times\mathbf{B}^M\right).$$

At this point, a closed system is determined from Maxwell's equations along with Eqs.(2.8)–(2.9) and Eq.(2.12). This provides a complete description of the plasma; however, such a system assumes detailed knowledge of individual particles. Specifically, treating Eq.(2.12) as an initial value problem requires $6N_\alpha$ initial conditions on the particles of species α by the assumed form Eq.(2.7) from which Eq.(2.12) was derived. Hence, any solution to this closed system is equivalent to evolving the trajectories in time of $6\sum_\alpha N_\alpha$ equations of the form Eqs.(2.10)–(2.11) coupled to Maxwell's equations through Eqs.(2.8)–(2.9). Considering the large number of particle present in a plasma, for example $N_\alpha \sim 10^{20}$ m^{-3} in a typical fusion plasma, following this approach is a daunting task.

This system does, however, provide a starting point for deriving kinetic models based on statistical averaging, which is considered next.

2.3 Kinetic Theory

A more tractable approach to the closure of Maxwell's equations is to take the ensemble average of the microscopic system. That is, we average over an infinite number of realizations of a plasma such that each realization contains the same number of particles and macroscopic parameters (density, temperature, etc.), but the actual positions and velocities of particles vary randomly for each realization. Let us denote the ensemble averaging procedure by $\langle\cdot\rangle$ and the ensemble averaged distribution function by f_α. That is

$$f_\alpha = \langle \mathcal{F}_\alpha^M \rangle.$$

The microscopic distribution function can then be written as

$$\mathcal{F}_\alpha^M = f_\alpha + \delta f_\alpha,$$

where

$$\delta f_\alpha = \mathcal{F}_\alpha^M - f_\alpha$$

represents the part of the microscopic distribution function that fluctuates between realizations, accounting for the discrete particle effects. Similarly, the microscopic electric and magnetic fields, charge and current densities are decomposed as

$$\mathbf{E}^M = \mathbf{E} + \delta\mathbf{E}$$

$$\mathbf{B}^M = \mathbf{B} + \delta\mathbf{B}$$

$$\rho^M = \rho + \delta\rho$$

$$\mathbf{J}^M = \mathbf{J} + \delta\mathbf{J},$$

where the first terms on the right hand side now represent the ensemble averaged quantities. Averaging of Maxwell's equations preserves the form of Eqs.(2.3)–(2.6), where the equations are

now expressed in terms of the ensemble averaged quantities. Averaging on Eq.(2.12), however, does not lead to a simple form, since correlations in the microscopic system prevent a separation of the averaged and fluctuating parts in the third term. In particular,

$$\langle \mathbf{a}_\alpha^M \cdot \nabla_{\mathbf{v}} \mathcal{F}_\alpha^M \rangle \neq \langle \mathbf{a}_\alpha^M \rangle \cdot \nabla_{\mathbf{v}} f_\alpha.$$

We may write

$$\langle \mathbf{a}_\alpha^M \cdot \nabla_{\mathbf{v}} \mathcal{F}_\alpha^M \rangle = \langle \mathbf{a}_\alpha^M \rangle \cdot \nabla_{\mathbf{v}} f_\alpha - C_\alpha(f_{\alpha'}),$$

where C_α is known as the collision operator and accounts for the microscopic correlations. With this, we can write the ensemble average of Eq.(2.12) as

$$\frac{\partial f_\alpha}{\partial t} + \mathbf{v} \cdot \nabla f_\alpha + \mathbf{a}_\alpha \cdot \nabla_{\mathbf{v}} f_\alpha = C_\alpha(f_{\alpha'}), \tag{2.13}$$

where

$$\mathbf{a}_\alpha = \frac{q_\alpha}{m_\alpha} \left(\mathbf{E} + \mathbf{v} \times \mathbf{B} \right).$$

This form is known as the plasma kinetic equation, and is the starting point for most plasma models. Various approximations for the collision operator in Eq.(2.13) exist, yielding different plasma kinetic models. The importance of this term, however, is expected to scale with the plasma parameter Λ given its interpretation of measuring mean kinetic energy to inter-particle potential energy. In some situations, there is a large time scale separation between the collisional processes and collective behaviors in a plasma, and it is appropriate to neglect the collision operator altogether. In this case, we are left with

$$\frac{\partial f_\alpha}{\partial t} + \mathbf{v} \cdot \nabla f_\alpha + \frac{q_\alpha}{m_\alpha} \left(\mathbf{E} + \mathbf{v} \times \mathbf{B} \right) \cdot \nabla_{\mathbf{v}} f_\alpha = 0, \tag{2.14}$$

which is known as the Vlasov equation and is the central equation for the work in this thesis.

We note that the Vlasov equation shares the same form as Eq.(2.12). The solution f_α, however, is assumed to be in a smoother function space than $\mathcal{F}_\alpha^M$ due to the ensemble averaging procedure and no longer contains individual particle information. The function $f_\alpha(\mathbf{x}, \mathbf{v}, t)$ is non-negative and defined over the six dimensional phase space and time interval $\mathbb{X} \times \mathbb{V} \times [0, T]$, where

$\mathbb{X} \subset \mathbb{R}^3$ and $\mathbb{V} = \mathbb{R}^3$ is the space of possible velocities. The quantity $f_\alpha(\mathbf{x}, \mathbf{v}, t) d^3x d^3v$ represents the expected number of particles of species α found in the volume $d^3x d^3v$ centered at $(\mathbf{x}, \mathbf{v})$ at time t, and the normalization is taken such that

$$\int_{\mathbb{X}\times\mathbb{V}} f_\alpha d^3x d^3v = N_\alpha.$$

For given electric and magnetic fields, Eq.(2.14) is a first order, linear, hyperbolic partial differential equation. In addition, Eq.(2.14) expresses the conservation of particles over phase space. To see this, we first define the phase space velocity by

$$\mathbf{U} \equiv \begin{pmatrix} \mathbf{v} \\ \frac{q_\alpha}{m_\alpha}(\mathbf{E} + \mathbf{v} \times \mathbf{B}) \end{pmatrix}$$

and the phase space gradient operator by

$$\nabla_{\mathbf{Z}} \equiv \begin{pmatrix} \nabla \\ \nabla_{\mathbf{v}} \end{pmatrix}.$$

It can be shown that $\nabla_{\mathbf{Z}} \cdot \mathbf{U} = 0$, allowing Eq.(2.14) to be written in conservative form as

$$\frac{\partial f_\alpha}{\partial t} + \nabla_{\mathbf{Z}} \cdot (\mathbf{U} f_\alpha) = 0.$$

Integrating over an arbitrary phase space volume $V \subset \mathbb{X} \times \mathbb{V}$ and applying the divergence theorem yields

$$\frac{\partial}{\partial t} \int_V f_\alpha d^3x d^3v = -\int_{\delta V} f_\alpha \mathbf{U} \cdot \mathbf{n} dS, \tag{2.15}$$

where δV is the boundary of V, $\mathbf{n}$ is the outward pointing unit normal field of δV, and dS is a differential surface area element of δV. Equation (2.15) states that the rate of change of the number of particles contained in V is due to the number particles passing through the boundary surface δV per unit time.

For a self consistent plasma model, the fields are obtained from Maxwell's equations, with ρ and $\mathbf{J}$ from the plasma model. The coupling again is through the velocity moments of f_α as

$$\rho(\mathbf{x}) = \sum_\alpha q_\alpha \int_{\mathbb{V}} f_\alpha(\mathbf{x}, \mathbf{v}) d^3v \tag{2.16}$$

$$\mathbf{J}(\mathbf{x}) = \sum_\alpha q_\alpha \int_{\mathbb{V}} \mathbf{v} f_\alpha(\mathbf{x}, \mathbf{v}) d^3v, \tag{2.17}$$

resulting in a closed model described by the nonlinear system of partial integro-differential equations Eqs.(2.3)–(2.6), Eq.(2.14), and Eqs.(2.16)–(2.17).

2.4 Magnetized Plasmas

Of particular importance in application, specifically in the confinement of a plasma, is the magnetic field. In confinement applications, often a strong auxiliary field is imposed on the plasma to restrict the particle motion to be mainly along the direction of the magnetic field. As an introduction to the basic concepts of charged particle motion in a magnetic field, it is useful to consider the Lorentz force equations of motion for a particle with charge q and mass m in a uniform $\mathbf{B}$ field with $\mathbf{E} = \mathbf{0}$. In this case, we have

$$\begin{aligned} \frac{d\mathbf{x}}{dt} &= \mathbf{v} \\ \frac{d\mathbf{v}}{dt} &= \frac{q}{m}\left(\mathbf{v} \times \mathbf{B}\right), \end{aligned}$$

whose analytical solution can be written as

$$\begin{aligned} \mathbf{v}(t) &= v_\perp \left(\cos\left(\Omega t - \varphi\right)\mathbf{e}_1 + \sin\left(\Omega t - \varphi\right)\mathbf{e}_2\right) + v_\parallel \hat{\mathbf{b}} \\ \mathbf{x}(t) &= \mathbf{R} + \frac{v_\perp}{\Omega}\left(\cos\left(\Omega t - \varphi\right)\mathbf{e}_2 - \sin\left(\Omega t - \varphi\right)\mathbf{e}_1\right) + v_\parallel t \hat{\mathbf{b}}. \end{aligned} \tag{2.18}$$

In this expression, we write $\mathbf{B} = B\hat{\mathbf{b}}$, where B is the magnitude of $\mathbf{B}$ and $\hat{\mathbf{b}}$ is the unit vector parallel to $\mathbf{B}$. The vectors $\mathbf{e}_1$, $\mathbf{e}_2$, and $\hat{\mathbf{b}}$ form an orthonormal basis such that $\mathbf{e}_1 \times \mathbf{e}_2 = \hat{\mathbf{b}}$. The parameter Ω has been defined as

$$\Omega = \frac{qB}{m},$$

and $v_\perp$, $v_\parallel$, φ, and $\mathbf{R}$ are constants of motion, which can be determined from the initial conditions. From Eq.(2.18), we see that the particle motion perpendicular to $\hat{\mathbf{b}}$ is characterized by circular orbits centered around $\mathbf{R}$ with frequency Ω and radius $v_\perp/\Omega$. This motion is known at the gyro-motion of the particle. Parallel to $\hat{\mathbf{b}}$, the particle is freely streaming with velocity $v_\parallel$. This simple example motivates much of the terminology associated with magnetized plasmas. In particular, Ω

is known as the gyro-frequency, φ is the gyro-phase, $v_\parallel$ and $v_\perp$ are the parallel and perpendicular velocities, respectively, $\mathbf{R}$ is the guiding center, and $\rho \equiv v_\perp/\Omega$ is the gyro-radius.

2.4.1 Drift Motions

When a perpendicular electric field or a weakly inhomogeneous magnetic field is considered, the main modification to the motion is addition of slow perpendicular drifts of the guiding center $\mathbf{R}$. In this case, perturbative techniques can be employed to take advantage of scale separations between field inhomogeneities and the spatial and temporal scales of the gyro-motion to simplify the particle dynamics. This is a well established field known as guiding center theory [27–31]. The guiding center drift motions that are most relevant to this work consist of the so called $E \times B$ drift, denoted $\mathbf{v}_E$, the magnetic drifts, denoted $\mathbf{v}_D$, and the polarization drift, denoted $\mathbf{v}_{\text{pol}}$. The $E \times B$ drift is due to an electric field perpendicular to $\mathbf{B}$ and is given by

$$\mathbf{v}_E = \frac{\mathbf{E} \times \mathbf{B}}{B^2},$$

showing a perpendicular electric field to cause particles to drift in a direction that is perpendicular to both $\mathbf{E}$ and $\mathbf{B}$. It is noted that this drift is independent of q, m, and $v_\perp$, meaning the magnitude and direction of the drift is the same for all charged particle species. The magnetic drifts occur for particles in a magnetic field with a spatially varying magnitude or a nonzero curvature. The magnetic drifts can be written as

$$\mathbf{v}_D = \mathbf{v}_{\nabla B} + \mathbf{v}_{\mathbf{R}},$$

where $\mathbf{v}_{\nabla B}$ is known as the *grad-B-drift* and $\mathbf{v}_{\mathbf{R}}$ is the *curvature drift*. These are given as

$$\mathbf{v}_{\nabla B} = \frac{m v_\perp^2}{2qB} \hat{\mathbf{b}} \times \frac{\nabla B}{B}$$

and

$$\mathbf{v}_{\mathbf{R}} = \frac{m v_\parallel^2}{qB} \hat{\mathbf{b}} \times \left(\hat{\mathbf{b}} \cdot \nabla \right) \hat{\mathbf{b}}.$$

The magnetic drifts are perpendicular to both $\hat{\mathbf{b}}$ and to the direction in which $\mathbf{B}$ varies. In addition, there is dependence on q, m, $v_\parallel$ and $v_\perp$. Oppositely charged particles will drift in opposite directions,

and particles with greater speeds will experience larger drifts. Finally, we consider the polarization drift, which is due to a time varying perpendicular electric field. The polarization drift is given by

$$\mathbf{v}_{\text{pol}} = \frac{m}{qB}\frac{d}{dt}\left(\frac{\mathbf{E}}{B}\right),$$

which is dependent on m and q.

2.4.2 Gyrokinetics

For phenomena in magnetized plasmas occurring at frequencies which are low compared to the gyro-frequency, there exists an asymptotic reduction to the Vlasov-Maxwell system known as gyrokinetics [6–10]. Gyrokinetics takes a perturbative expansion of the system in the following quantities, which are assumed to be small

$$\frac{\omega}{\Omega_i} \sim \frac{\rho_i}{L_{eq}} \sim \frac{\rho_i}{L_B} \sim k_\parallel \rho_i \sim \frac{e\phi}{T_e} \sim \frac{\delta B}{B_0} \sim O(\epsilon), \qquad \epsilon \ll 1.$$

Here, ω is representative of a frequency on which the phenomena of interest occurs, Ω_i and ρ_i are the gyro-frequency and gyro-radius of a typical ion, respectively, L_{eq} is representative of the plasma equilibrium gradient scale length, L_B is representative of the background magnetic field gradient scale length, $k_\parallel$ is representative of a wave number parallel to the magnetic field, δB represents the magnitude of the self generated part of the magnetic field, and B_0 the magnitude of the background magnetic field. The electron temperature is again denoted by T_e, but here we take this quantity to include Boltzmann's constant in its definition, giving T_e units of energy. This convention for temperature is taken for the remainder of this thesis. A change of variables is performed to express Eq.(2.14) in terms of the guiding center coordinate $\mathbf{R}$ defined by

$$\mathbf{R} = \mathbf{x} - \boldsymbol{\rho},$$

where

$$\boldsymbol{\rho} = \frac{m}{q}\frac{\mathbf{v}_\perp \times \hat{\mathbf{b}}}{B},$$

with

$$\mathbf{v}_\perp = v_\perp \left(\cos(\varphi)\mathbf{e}_1 + \sin(\varphi)\mathbf{e}_2\right).$$

After averaging over the gyro-phase and taking the resulting equation to first order in ϵ, the gyrokinetic Vlasov equation is obtained, which describes the evolution of a distribution function of guiding centers $\bar{f}$ as

$$\frac{\partial \bar{f}}{\partial t} + \left(v_{\parallel} \hat{\mathbf{b}} + \mathbf{v}_E + \mathbf{v}_D \right) \cdot \frac{\partial \bar{f}}{\partial \mathbf{R}} + \frac{dv_{\parallel}}{dt} \frac{\partial \bar{f}}{\partial v_{\parallel}} = 0$$
$$\frac{dv_{\parallel}}{dt} = \frac{q}{m} \langle \mathbf{E} \rangle \cdot \hat{\mathbf{b}} + \langle \mathbf{E} \rangle \cdot \frac{v_{\parallel}}{B} \hat{\mathbf{b}} \times \left(\hat{\mathbf{b}} \cdot \frac{\partial}{\partial \mathbf{R}} \right) \hat{\mathbf{b}} - \frac{v_{\perp}^2}{2} \hat{\mathbf{b}} \cdot \frac{\partial \ln B}{\partial \mathbf{R}},$$

where $\langle \mathbf{E} \rangle$ denotes the electric field averaged over the gyro-phase and is used in evaluating $\mathbf{v}_E$. A similar averaging operator is used in evaluating velocity moments in the gyrokinetic model to account for all guiding centers which contribute to the moment at a particle coordinate $\mathbf{x}$. Explicit forms for these operators are given in Chapter 3, where a gyrokinetic ion model is considered for the ion temperature gradient instability.

2.5 The Particle-in-Cell method

The particle-in-cell (PIC) method is a numerical technique to approximate the behavior of a collisionless plasma described by the Vlasov equation Eq.(2.14), through the use of a large set of finite sized computational particles [32–34]. Although most derivations are based on arguments from the physical interpretation of the system, there has been some work done in establishing a firm mathematical foundation for the PIC method, including a convergence theory of the approximate particle distribution function in the setting of distributional spaces [35–37]. Here, we present the basic elements for two variations of the PIC approximation to Eq.(2.14) - the conventional full-f method and the δf method. While we present each method for the Vlasov-Maxwell system, it should be clear how these methods can be applied to variations of this system. For simplicity, we consider a rectangular computational domain $D \subset \mathbb{R}^3$ for the spatial portion of phase space with a uniformly discretized grid. We introduce a multi-index $\mathbf{j}$ defined by $\mathbf{j} = [j_x, j_y, j_z]^T$ with $0 \leq j_x \leq N_x$, $0 \leq j_y \leq N_y$, and $0 \leq j_z \leq N_z$ for $N_x, N_y, N_z \in \mathbb{N}$ and denote grid points by $\mathbf{X}_{\mathbf{j}}$,

where

$$\mathbf{X_j} = \begin{bmatrix} \Delta x & 0 & 0 \\ 0 & \Delta y & 0 \\ 0 & 0 & \Delta z \end{bmatrix} \mathbf{j}.$$

In addition to a discretized computational domain, the PIC method uses a set of N_c computational particles to represent a species α, where the state of each computational particle is defined by its spatial position $\mathbf{x}_p \in D$ and velocity coordinate $\mathbf{v}_p \in \mathbb{R}^3$ for $p = 1, ..., N_c$, with $\mathbf{x}_p$ and $\mathbf{v}_p$ allowed to evolve in time.

2.5.1 Full-f PIC Method

The starting point for the full-f PIC approximation to Eq.(2.14) is to assume an approximate form for f_α as

$$f_\alpha(\mathbf{X}_j, \mathbf{v}) \approx \hat{f}_\alpha(\mathbf{X_j}, \mathbf{v}) \equiv \frac{N_\alpha}{\Delta V N_c} \sum_{p=1}^{N_c} S_{\mathbf{x}} \left(\mathbf{X_j} - \mathbf{x}_p\right) \delta^3_{\mathbf{v}} \left(\mathbf{v} - \mathbf{v}_p\right), \tag{2.19}$$

where $\Delta V = \Delta x \Delta y \Delta z$. In this expression, $S_{\mathbf{x}}$ is called the shape function and provides an approximation to the spatial Dirac delta function. The shape function is used in the PIC method to transfer information between the particle system and the grid. We note here the similarity of Eq.(2.19) to the Klimontovich-Dupree representation in Eq.(2.7). The Klimontovich-Dupree representation is a solution to Eq.(2.12), in a distributional sense, provided that the particles are taken to evolve according to the Newton-Lorentz equations of motion in Eqs.(2.10)–(2.11). This motivates taking the computational particles' positions and velocities in Eq.(2.19) to evolve in the same way, since Eq.(2.12) shares the same form as Eq.(2.14). We therefore take

$$\frac{d\mathbf{x}_p}{dt} = \mathbf{v}_p \tag{2.20}$$

$$\frac{d\mathbf{v}_p}{dt} = \frac{q_\alpha}{m_\alpha} \left(\mathbf{E}(\mathbf{x}_p) + \mathbf{v}_p \times \mathbf{B}(\mathbf{x}_p)\right) \tag{2.21}$$

for $p = 1, ..., N_c$. In practice, the particles are evolved in time with a numerical integration scheme applied to Eqs.(2.20)–(2.21).

Next, we discuss the choice of the shape function. For the distribution function f_α in Eq.(2.14), the normalization was such that

$$\int_{\mathbb{X}\times\mathbb{V}} f_\alpha d^3x d^3v = N_\alpha.$$

Similarly, for the approximate distribution function in Eq.(2.19), we require

$$\int_{\mathbb{R}^3} \left[\sum_{\mathbf{j}} \hat{f}_\alpha \left(\mathbf{X_j}, \mathbf{v} \right) \Delta V \right] d^3v = N_\alpha.$$

This is satisfied by enforcing the condition

$$\sum_{\mathbf{j}} S_{\mathbf{x}}(\mathbf{X}_j - \mathbf{x}) = 1$$

on the shape function. The shape function is also taken to have positivity, finite support, and to exhibit the symmetry $S_{\mathbf{x}}(\mathbf{x} - \mathbf{y}) = S_{\mathbf{x}}(\mathbf{y} - \mathbf{x})$. Typically, $S_{\mathbf{x}}$ is defined in terms of the B-spline functions, denoted b_l. The first few B-splines are defined for $x \in \mathbb{R}$ as

$$b_0(x) = \begin{cases} 1 & : |x| \leq \frac{1}{2} \\ 0 & : |x| > \frac{1}{2} \end{cases}$$

$$b_1(x) = \begin{cases} 1 - |x| & : |x| \leq 1 \\ 0 & : |x| > 1 \end{cases}$$

$$b_2(x) = \begin{cases} \frac{3}{4} - x^2 & : |x| \leq \frac{1}{2} \\ \frac{1}{8}\left(3 - 2|x|\right)^2 & : \frac{1}{2} < |x| \leq \frac{3}{2} \\ 0 & : |x| > \frac{3}{2} \end{cases}$$

and are illustrated in Figure 2.1. We define a one dimensional shape function simply as $S_{1\mathrm{D}} = b_l(x)$, and take the full shape function to be

$$S_{\mathbf{x}}(\mathbf{x}) = S_{1\mathrm{D}}\left(\frac{x}{\Delta x}\right) S_{1\mathrm{D}}\left(\frac{y}{\Delta y}\right) S_{1\mathrm{D}}\left(\frac{z}{\Delta z}\right).$$

Once a shape function has been selected, the PIC approximation provides a way to compute the velocity moments of $\hat{f}_\alpha$ on the grid points from the particle system. For example, the number

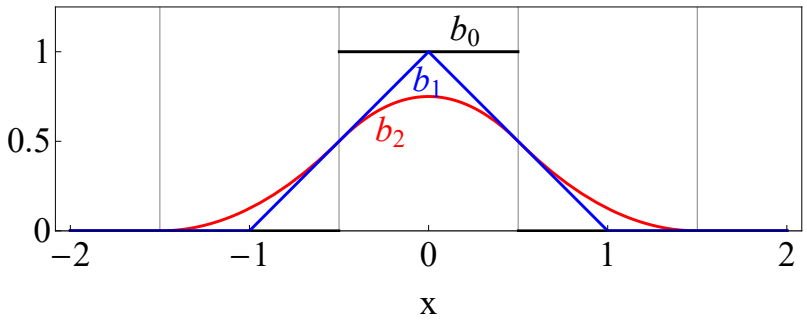

Figure 2.1: Illustration of the B-spline functions b_l for $l = 0, 1, 2$.

density for species α is computed at the grid point $\mathbf{X_j}$ by

$$n_\alpha(\mathbf{X}_j) \approx \int_{\mathbb{R}^3} \hat{f}_\alpha\left(\mathbf{X}_j, \mathbf{v}\right) d^3v = \frac{N_\alpha}{\Delta V N_c} \sum_{p=1}^{N_c} S_{\mathbf{x}}(\mathbf{X}_j - \mathbf{x}_p), \tag{2.22}$$

where the finite support of the shape function allows the summation to be carried out for only the particles local to $\mathbf{X_j}$. Similarly, the flux density at grid point $\mathbf{X_j}$ is computed as

$$n_\alpha \mathbf{u}_\alpha\left(\mathbf{X_j}\right) \approx \int_{\mathbb{R}^3} \mathbf{v} \hat{f}_\alpha\left(\mathbf{X}_j, \mathbf{v}\right) d^3v = \frac{N_\alpha}{\Delta V N_c} \sum_{p=1}^{N_c} \mathbf{v}_p S_{\mathbf{x}}(\mathbf{X}_j - \mathbf{x}_p). \tag{2.23}$$

The velocity moments can then be used to obtain charge and current densities at the grid points by

$$\rho\left(\mathbf{X_j}\right) = \sum_\alpha q_\alpha n_\alpha\left(\mathbf{X}_j\right) \tag{2.24}$$

$$\mathbf{J}\left(\mathbf{X_j}\right) = \sum_\alpha q_\alpha n_\alpha \mathbf{u}_\alpha\left(\mathbf{X}_j\right), \tag{2.25}$$

which are used to provide closure to a numerical implementation of Maxwell's equations to solve for $\mathbf{E}$ and $\mathbf{B}$ at the grid points. Remaining is a method for evaluating $\mathbf{E}$ and $\mathbf{B}$ at the particles location, which is required for the numerical implementation for evolving the particles according to Eqs.(2.20)–(2.21). This will require an interpolation scheme, since the field are defined only at the grid points. The electric field experienced by a particle at location $\mathbf{x}_p$ is interpolated from the grid electric field as

$$\mathbf{E}(\mathbf{x}_p) = \sum_{\mathbf{j}} \mathbf{E}(\mathbf{X}_j) S_{\mathbf{x}}\left(\mathbf{X_j} - \mathbf{x}_p\right), \tag{2.26}$$

and similarly for $\mathbf{B}(\mathbf{x}_p)$, where we have taken the same weighting function as in Eq.(2.19). Although taking the same weighting functions in Eq.(2.19) and Eq.(2.26) isn't strictly necessary, there are good reasons for doing so. Choosing different weighting functions has been shown to generate self forces on particles, which can lead to instabilities and violations of momentum conservation [32]. The PIC algorithm can be summarized into four steps:

(1) Interpolation of the forces due to the grid electric and magnetic fields by Eq.(2.26).

(2) Advancing the computational particles in time using a numerical integrator applied to Eqs.(2.20)–(2.21).

(3) Depositing velocity moments to the grid points using Eq.(2.22) and Eq.(2.23) to obtain charge and current density as Eqs.(2.24)–(2.25).

(4) Solving a discretized version of the field equations Eq.(2.3) for the grid electric and magnetic fields.

The computational cycle is illustrated in Figure 2.2.

2.5.2 δf PIC Method

The δf method is a formulation of PIC that is known to reduce the noise due to discrete particle effects in simulations of plasmas near equilibrium [38–42]. The basic principle is to replace a large portion of the distribution function with an analytically known function and to use the particle system to resolve only a small deviation from the known function. The δf method has similarities to control variates Monte Carlo methods, and many of the same steps from the full-f PIC method carry over. The δf method follows from reformulating Eq.(2.14) by assuming $f_\alpha = f_{\alpha,0} + \delta f_\alpha$, where $f_{\alpha,0}$ is a known "equilibrium" distribution and δf_α is an unknown perturbation from equilibrium to be solved for by the PIC method. It is also assumed that the force due to the fields can be decomposed as $\mathbf{F}_\alpha = \mathbf{F}_{\alpha,0} + \delta\mathbf{F}_\alpha$, where $\mathbf{F}_{\alpha,0}$ is a background force consistent with the equilibrium state and $\delta\mathbf{F}_\alpha$ is a perturbed force due to the self-generated fields from the perturbed part of the

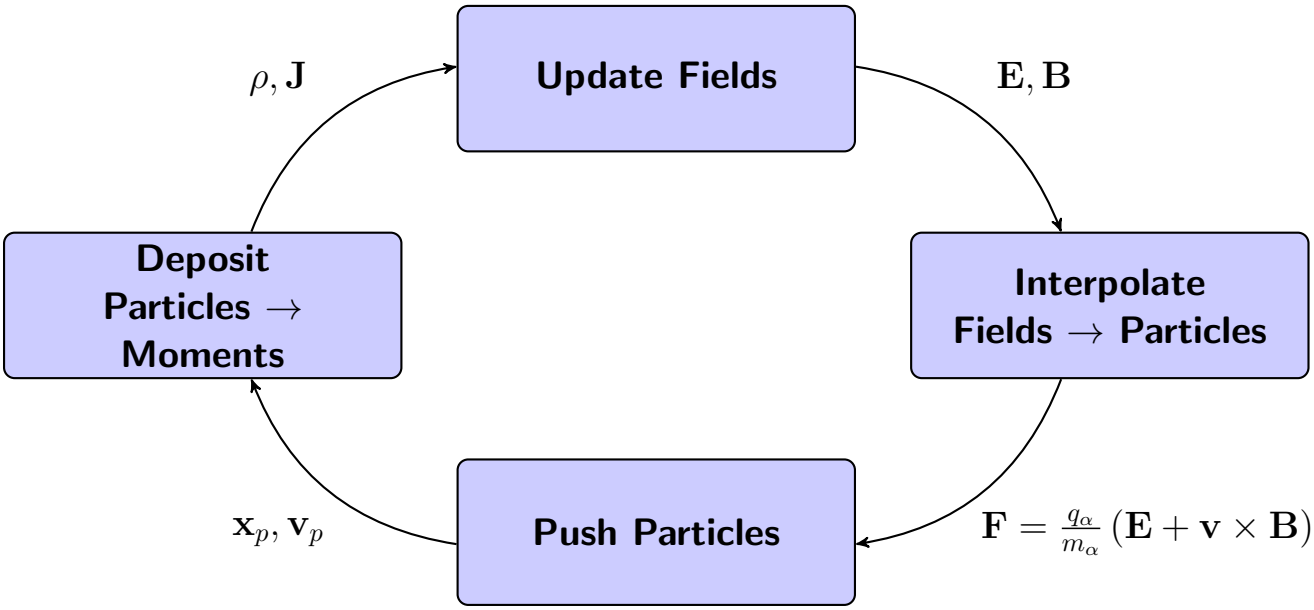

Figure 2.2: Illustration of the PIC computational cycle

distribution. Plugging this form into Eq.(2.14), we have

$$\mathbf{v} \cdot \nabla f_{\alpha,0} + \mathbf{F}_{\alpha,0} \cdot \nabla_{\mathbf{v}} f_{\alpha,0} = 0 \tag{2.27}$$

$$\frac{\partial \delta f_\alpha}{\partial t} + \mathbf{v} \cdot \nabla \delta f_\alpha + (\mathbf{F}_{\alpha,0} + \delta \mathbf{F}_\alpha) \cdot \nabla_{\mathbf{v}} \delta f_\alpha = -\delta \mathbf{F}_\alpha \cdot \nabla_{\mathbf{v}} f_{\alpha,0}, \tag{2.28}$$

where Eq.(2.27) is assumed to hold for $f_{\alpha,0}$, and Eq.(2.28) is used to solve for δf_α. For the δf method, in addition to the position and velocity coordinates, each computational particle is assigned a "weight" defined by

$$w_p = \frac{\delta f_\alpha(\mathbf{x}_p, \mathbf{v}_p)}{f_\alpha(\mathbf{x}_p, \mathbf{v}_p)}. \tag{2.29}$$

The perturbed part of the distribution function at a grid point $\mathbf{X_j}$ is then approximated by

$$\delta f_\alpha(\mathbf{X_j}, \mathbf{v}) \approx \delta \hat{f}_\alpha(\mathbf{X_j}, \mathbf{v}) = \frac{N_\alpha}{\Delta V N_c} \sum_{p=1}^{N_c} w_p S_{\mathbf{x}} \left(\mathbf{X}_j - \mathbf{x}_p\right) \delta_{\mathbf{v}}^3 \left(\mathbf{v} - \mathbf{v}_p\right), \tag{2.30}$$

where this form is motivated by a formal multiplication of a Klimontovich-Dupree representation of the full distribution function by $\delta f_\alpha(\mathbf{x}, \mathbf{v}) / f_\alpha(\mathbf{x}, \mathbf{v})$ and using properties of the Dirac delta function. The selection for the shape function involves the same considerations as in the full-f method, and

the particle trajectories are again taken to follow Eqs.(2.20)–(2.21). Returning to Eq.(2.28), it follows from the method of characteristics that along the trajectory of a particle, δf_α evolves as

$$\frac{d}{dt}\delta f_\alpha = -\delta \mathbf{F}_\alpha \left(\mathbf{x}_p, \mathbf{v}_p\right) \cdot \nabla_{\mathbf{v}_p} f_{\alpha,0} \left(\mathbf{x}_p, \mathbf{v}_p\right). \tag{2.31}$$

Taking a time derivative of Eq.(2.29) and using Eq.(2.31), after some algebra, we arrive at an equation for the evolution of w_p as

$$\frac{dw_p}{dt} = -(1 - w_p)\delta \mathbf{F}_\alpha \cdot \nabla_{\mathbf{v}_p} \ln f_{\alpha,0}(\mathbf{x}_p, \mathbf{v}_p).$$

The number density can be computed from Eq.(2.30) as

$$\begin{aligned} n_\alpha(\mathbf{X}_j) &= n_{\alpha,0}(\mathbf{X}_j) + \delta n_\alpha(\mathbf{X}_j) \\ &\approx \int_{\mathbb{R}^3} f_{\alpha,0} \left(\mathbf{X}_j, \mathbf{v}\right) d^3v + \frac{N_\alpha}{\Delta V N_c} \sum_{p=1}^{N_c} w_p S_{\mathbf{x}}(\mathbf{X}_j - \mathbf{x}_p), \end{aligned}$$

and the flux density as

$$\begin{aligned} n_\alpha \mathbf{u}_\alpha(\mathbf{X}_j) &= n_{\alpha,0}\mathbf{u}_{\alpha,0}(\mathbf{X}_j) + \delta \mathbf{u}_\alpha n_\alpha(\mathbf{X}_j) \\ &\approx \int_{\mathbb{R}^3} \mathbf{v} f_{\alpha,0} \left(\mathbf{X}_j, \mathbf{v}\right) d^3v + \frac{N_\alpha}{\Delta V N_c} \sum_{p=1}^{N_c} w_p \mathbf{v}_p S_{\mathbf{x}}(\mathbf{X}_j - \mathbf{x}_p), \end{aligned}$$

which can again be used in Eqs.(2.24)–(2.25) to provide closure to a numerical implementation of Maxwell's equations. Finally, the interpolation of forces is the same in the δf method as in the full-f method, i.e. Eq.(2.26).

Chapter 3

Fully Kinetic and Gyrokinetic Ion Models for the Ion Temperature Gradient Instability

In this chapter, we present fully kinetic (FK) and gyrokinetic (GK) ion models for the ion temperature gradient (ITG) driven instability. On time scales which are short compared to collisional times, magnetized plasmas can exist in a wide variety of stationary states which may include density and temperature gradients [2, 3]. In a plasma with an equilibrium temperature gradient, pressure perturbations generate electric fields, causing particles to convect along the gradient direction due to the $\mathbf{v}_E$ drift. Phase differences between the electrostatic potential and the pressure perturbation can result in "hot" particles convecting into regions of positive pressure perturbation and "cold" particles convecting into regions of negative pressure perturbation. The perturbation is therefore reinforced, driving an instability known as the ITG mode. Turbulent plasma states driven by the unstable ITG mode can lead to enhanced particle and energy losses in confined plasmas. Useful discussions on the physical mechanisms underlying this instability can be found in a number of references including [3–5, 43].

The FK ion model presented in this chapter is similar to the one that was used in [17] to make comparisons with an extended magnetohydrodynamic model for the ITG mode. New results presented in this chapter include a detailed linear dispersion comparison between the FK and GK ion slab ITG models in Section 3.2.3 and the extension of the FK ion ITG model for a weakly inhomogeneous magnetic field in Section 3.4.2. This chapter is organized as follows. In Section 3.1 we present FK and GK ion models including equilibrium density and temperature gradients in a

uniform background magnetic field. The equilibrium distributions in both models are constructed from constants of motion representing the kinetic energy of an ion and the guiding center coordinate perpendicular to the magnetic field. In Section 3.2, we derive and compare the linear dispersion relations resulting from each model. It is shown that under the GK ordering assumptions, the FK ion dispersion relation reduces to the GK ion dispersion relation, assuring the inclusion of the GK normal modes in the FK ion model. The low frequency modes included in the models are shown to be deformations of the ion acoustic wave due to the equilibrium gradients. The ion acoustic wave in the limit of a homogeneous equilibrium is the test bed model considered in Chapter 4 for the development of orbit averaging and sub-cycling time stepping schemes. Finally in this section, we examine the ion Bernstein modes [44] which have frequencies near harmonics of the ion gyro-frequency. The ion Bernstein modes are an example of high frequency physics which is present in the FK ion model but is analytically eliminated in the GK ion model. Section 3.3 presents linear simulation results of the ITG instability using the FK ion model. Excellent agreement is shown when compared to the analytical dispersion theory. In addition, the GK dispersion theory produces excellent agreement to both the FK ion dispersion theory and the FK ion simulation results. In Section 3.4, we discuss the extension of the FK and GK ion models when weak inhomogeneities are included in the background magnetic field. This work will be of importance in Chapter 5, where the ITG instability is simulated in a toroidal magnetic field.

3.1 Kinetic Ion Models for the ITG Instability in a Uniform Magnetic Field

Here we present the governing equations for modelling the ITG instability in a uniform $\mathbf{B}$ field, first with FK ions and then with GK ions. The magnetic field is given as $\mathbf{B} = B\hat{\mathbf{b}}$, where B is the magnitude of $\mathbf{B}$ and $\hat{\mathbf{b}}$ is the unit vector in the direction of $\mathbf{B}$. In this section, $\mathbf{B}$ is assumed to have no spatial or time dependence. We work in a Cartesian coordinate system in which the vectors $\mathbf{e}_1$, $\mathbf{e}_2$, and $\hat{\mathbf{b}}$ form an orthonormal basis such that $\mathbf{e}_1 \times \mathbf{e}_2 = \hat{\mathbf{b}}$. The position vector $\mathbf{x}$ can

be expressed as $\mathbf{x} = x\mathbf{e}_1 + y\mathbf{e}_2 + z\hat{\mathbf{b}}$. Both the FK and GK ion models are electrostatic, assuming

$$\mathbf{E} = -\nabla\phi, \tag{3.1}$$

where ϕ is the electrostatic potential. In addition, both models take an adiabatic response for the electron density n_e as

$$n_e = \mathcal{N}_e \left(1 + \frac{e\phi}{T_e}\right), \tag{3.2}$$

where $\mathcal{N}_e$ is the equilibrium electron density, $-e$ is the electron charge, and T_e is the electron temperature. This is a simple approximation following from an assumption that the mobility of the electrons allows them to respond adiabatically to a low frequency electrostatic potential and they will therefore follow a Boltzmann distribution. Equation (3.2) is then a first order expansion of the Boltzmann distribution in $e\phi/T_e$. Finally, each model uses its respective form of the quasineutrality condition.

3.1.1 Fully Kinetic Ion Model

The starting point for the FK ion model is the Vlasov equation for the ion distribution function

$$\frac{\partial f_i}{\partial t} + \mathbf{v}\cdot\nabla f_i + \frac{q_i}{m_i}\left(\mathbf{E} + \mathbf{v}\times\mathbf{B}\right)\cdot\nabla_{\mathbf{v}} f_i = 0. \tag{3.3}$$

We assume f_i can be separated into equilibrium and perturbed parts as $f_i = f_0 + \delta f$ and seek an equilibrium state with temperature and density gradients. The ion equilibrium distribution function must satisfy

$$\mathbf{v}\cdot\nabla f_0 + \frac{q_i}{m_i}\left(\mathbf{v}\times\mathbf{B}\right)\cdot\nabla_{\mathbf{v}} f_0 = 0. \tag{3.4}$$

A common method for solving Eq.(3.4) involves finding constants of motion for an ion subject to the Lorentz force due to $\mathbf{B}$ [2,3]. For the uniform magnetic field, constants of motion can be readily obtained. In particular, we consider the kinetic energy of an ion K given by

$$K = \frac{m_i}{2}v^2, \tag{3.5}$$

where $v^2 = \mathbf{v} \cdot \mathbf{v}$, and the guiding center coordinate perpendicular to the magnetic field $\mathbf{R}_\perp$ given by

$$\mathbf{R}_\perp = \mathbf{x}_\perp + \frac{m_i}{q_i} \frac{\mathbf{v} \times \hat{\mathbf{b}}}{B},$$

with $\mathbf{x}_\perp = \mathbf{x} - (\mathbf{x} \cdot \hat{\mathbf{b}})\hat{\mathbf{b}}$. It can then be verified that Eq.(3.4) is satisfied by any distribution function of the form $f_0 = f_0(\mathbf{R}_\perp, K)$. Plugging this form into Eq.(3.3), the perturbed part of the distribution function then evolves according to

$$\frac{\partial}{\partial t}\delta f + \mathbf{v} \cdot \nabla \delta f + \frac{q_i}{m_i} (\mathbf{E} + \mathbf{v} \times \mathbf{B}) \cdot \nabla_{\mathbf{v}} \delta f = -\frac{\mathbf{E} \times \hat{\mathbf{b}}}{B} \cdot \frac{\partial f_0}{\partial \mathbf{R}_\perp} - q_i \mathbf{v} \cdot \mathbf{E} \frac{\partial f_0}{\partial K}. \tag{3.6}$$

Quasineutrality for the FK model is simply $n_e = n_i$, where the ion density is computed from the ion distribution function by

$$n_i(\mathbf{x}) = \int_{\mathbb{R}^3} f_i(\mathbf{x}, \mathbf{v}) d^3 v. \tag{3.7}$$

It is noted that the integral on the right hand side contains contributions from the equilibrium and perturbed parts. The equilibrium ion density comes from

$$n_0(\mathbf{x}_\perp) = \int_{\mathbb{R}^3} f_0 \left(\mathbf{x}_\perp + \frac{m_i}{q_i} \frac{\mathbf{v} \times \hat{\mathbf{b}}}{B}, \frac{m_i v^2}{2} \right) d^3 v.$$

Assuming the equilibrium distribution function varies on a length scale that is long compared to an average ion gyro-radius allows the expansion

$$f_0 \left(\mathbf{x}_\perp + \frac{m_i}{q_i} \frac{\mathbf{v} \times \hat{\mathbf{b}}}{B}, \frac{m_i v^2}{2} \right) \approx f_0 \left(\mathbf{x}_\perp, \frac{m_i v^2}{2} \right) + \frac{m_i}{q_i} \frac{\mathbf{v} \times \hat{\mathbf{b}}}{B} \cdot \nabla f_0 \left(\mathbf{x}_\perp, \frac{m_i v^2}{2} \right). \tag{3.8}$$

Integrating this expansion over velocity then gives

$$n_0(\mathbf{x}_\perp) \approx \int_{\mathbb{R}^3} f_0 \left(\mathbf{x}_\perp, \frac{m_i v^2}{2} \right) d^3 v, \tag{3.9}$$

noting that the integral of the second term on the right hand side of Eq.(3.8) vanishes. The contribution from the perturbed ion distribution function in Eq.(3.7) is given by

$$\delta n_i(\mathbf{x}) = \int_{\mathbb{R}^3} \delta f_i(\mathbf{x}, \mathbf{v}) d^3 v. \tag{3.10}$$

Quasineutrality along with the adiabatic electron model Eq.(3.2) then gives an equation for computing the electrostatic potential by

$$\frac{e\phi}{T_e} = \frac{\delta n_i}{n_0}, \tag{3.11}$$

where it is assumed that $\mathcal{N}_e = n_0$. Once a choice for $f_0(\mathbf{R}_\perp, K)$ is made, a closed system of equations is given by Eq.(3.1), Eq.(3.6), and Eqs.(3.9)–(3.11). Here, we choose for f_0 a local Maxwellian distribution function in which the equilibrium density $\mathcal{N}_i$ and temperature T_i vary with $R_x = \mathbf{R}_\perp \cdot \mathbf{e}_1$,

$$f_0(R_x, K) = \frac{\mathcal{N}_i(R_x)}{(2\pi T_i(R_x)/m_i)^{3/2}} \exp\left(-\frac{K}{T_i(R_x)}\right). \tag{3.12}$$

In this case, the right hand side of Eq.(3.6) can be written as

$$\frac{q_i}{T_i}\mathbf{v}\cdot\mathbf{E}f_0 - \frac{E_y}{B}\left[\frac{\partial \ln \mathcal{N}_i}{\partial R_x} + \frac{\partial \ln T_i}{\partial R_x}\left(\frac{K}{T_i} - \frac{3}{2}\right)\right] f_0, \tag{3.13}$$

with $E_y = \mathbf{E}\cdot\mathbf{e}_2$, and Eq.(3.9) yields simply $n_0 \approx \mathcal{N}_i$.

3.1.2 Gyrokinetic Ion Model

The GK Vlasov equation for the ion guiding center distribution function $\bar{f}_i$ is expressed in terms of the guiding center position vector $\mathbf{R}$, the magnetic moment μ, and the component of velocity parallel to the magnetic field $v_\parallel$ [9]. The guiding center position vector is related to the particle coordinates through

$$\mathbf{R} = \mathbf{x} - \boldsymbol{\rho},$$

where

$$\boldsymbol{\rho} = \frac{m_i}{q_i}\frac{\hat{\mathbf{b}}\times\mathbf{v}}{B}.$$

The parallel velocity is given by $v_\parallel = \mathbf{v}\cdot\hat{\mathbf{b}}$ and the magnetic moment by $\mu = v_\perp/2B$, with $v_\perp = |\mathbf{v}\times\hat{\mathbf{b}}|$. In the limit of a uniform magnetic field, the GK Vlasov equation is

$$\frac{\partial \bar{f}_i}{\partial t} + \left(v_\parallel\hat{\mathbf{b}} + \frac{\langle\mathbf{E}\rangle\times\hat{\mathbf{b}}}{B}\right)\cdot\frac{\partial \bar{f}_i}{\partial \mathbf{R}} + \frac{q_i}{m_i}\langle\mathbf{E}\rangle\cdot\hat{\mathbf{b}}\frac{\partial \bar{f}_i}{\partial v_\parallel} = 0. \tag{3.14}$$

The gyro-averaging operator $\langle\cdot\rangle$ acting on a function $\boldsymbol{\psi}(\mathbf{x})$ is defined by

$$\langle\boldsymbol{\psi}\rangle = \frac{\oint_C \boldsymbol{\psi}\left(\mathbf{x}=\mathbf{R}+\boldsymbol{\rho}\right) d\rho}{\oint_C d\rho},$$

where C is the path along one closed ion gyro-orbit, which can be parametrized by the gyro-phase φ as

$$\boldsymbol{\rho}(\varphi) = \frac{m_i}{q_i}\sqrt{\frac{2\mu}{B}}\left(\sin\varphi\mathbf{e}_1 + \cos\varphi\mathbf{e}_2\right), \qquad 0 \le \varphi \le 2\pi. \tag{3.15}$$

From Eq.(3.15), we can express Eq.(3.16) as

$$\langle\boldsymbol{\psi}\rangle = \frac{1}{2\pi}\int_0^{2\pi} \boldsymbol{\psi}\left(\mathbf{x}=\mathbf{R}+\boldsymbol{\rho}(\varphi)\right) d\varphi. \tag{3.16}$$

We again assume that $\bar{f}_i$ can be separated into equilibrium and perturbed parts as $\bar{f}_i = \bar{f}_0 + \delta\bar{f}$. The equilibrium guiding center distribution function satisfies simply

$$v_\parallel \hat{\mathbf{b}} \cdot \frac{\partial \bar{f}_0}{\partial \mathbf{R}} = 0.$$

Hence, we can again choose an equilibrium distribution of the form $\bar{f}_0 = \bar{f}_0(\mathbf{R}_\perp, K)$, where in terms of the GK variables

$$\mathbf{R}_\perp = \mathbf{R} - \left(\mathbf{R}\cdot\hat{\mathbf{b}}\right)\hat{\mathbf{b}}$$

and

$$K = m_i\left(\frac{v_\parallel^2}{2} + \mu B\right). \tag{3.17}$$

Plugging this form into Eq.(3.14), we have that the perturbed part of the guiding center distribution function evolves as

$$\frac{\partial}{\partial t}\delta\bar{f} + \left(v_\parallel\hat{\mathbf{b}} + \frac{\langle\mathbf{E}\rangle\times\hat{\mathbf{b}}}{B}\right)\cdot\frac{\partial}{\partial\mathbf{R}}\delta\bar{f} + \frac{q_i}{m_i}\langle\mathbf{E}\rangle\cdot\hat{\mathbf{b}}\frac{\partial}{\partial v_\parallel}\delta\bar{f} = -\frac{\langle\mathbf{E}\rangle\times\hat{\mathbf{b}}}{B}\cdot\frac{\partial\bar{f}_0}{\partial\mathbf{R}_\perp} - q_i v_\parallel\hat{\mathbf{b}}\cdot\langle\mathbf{E}\rangle\frac{\partial\bar{f}_0}{\partial K}. \tag{3.18}$$

In the GK ion model, $\bar{f}_i$ gives only the part of the ion distribution function that is independent of the gyro-phase φ. There is an additional contribution related to the polarization response of the ions, dependent on φ, which is included in the GK approximation of the full ion distribution function f_i. The full ion distribution function is approximated by

$$f_i \approx \bar{f}_i - \frac{q_i}{T_i}\left(\phi - \langle\phi\rangle\right)\bar{f}_0. \tag{3.19}$$

The number density contribution from the first term on the right hand side of Eq.(3.19) in the particle coordinates is obtained through

$$\bar{n}_i(\mathbf{x}) = \int_0^\infty \int_{-\infty}^\infty \left[\frac{1}{2\pi} \int_0^{2\pi} \bar{f}_i(\mathbf{R} = \mathbf{x} - \boldsymbol{\rho}(\mu, \varphi), v_\parallel, \mu) d\varphi \right] B dv_\parallel d\mu,$$

where the integral in brackets is to account for all guiding centers which can contribute to the density at $\mathbf{x}$. The contribution from the second term on the right hand side of Eq.(3.19) is the ion polarization density given by

$$n^{pol}(\mathbf{x}) = -\frac{q_i}{T_i} \left(\phi(\mathbf{x}) - \tilde{\phi}(\mathbf{x}) \right) \bar{n}_0,$$

where

$$\tilde{\phi}(\mathbf{x}) = \frac{1}{\bar{n}_0} \int_0^\infty \int_{-\infty}^\infty \left[\frac{1}{2\pi} \int_0^{2\pi} \langle \phi \rangle \left(\mathbf{R} = \mathbf{x} - \boldsymbol{\rho}(\mu, \varphi) \right) d\varphi \right] \bar{f}_0(\mathbf{x}_\perp, v_\parallel, \mu) B dv_\parallel d\mu.$$

Quasineutrality in the GK model can then be expressed as $n_e = \bar{n}_i + n^{pol}$, or by separating the equilibrium and perturbed parts of the guiding center distribution function, $n_e = \bar{n}_0 + \delta\bar{n} + n^{pol}$. Together with Eq.(3.2), we obtain the following equation for computing the electrostatic potential

$$\frac{e\phi}{T_e} + \frac{q_i}{T_i} \left(\phi - \tilde{\phi} \right) = \frac{\delta\bar{n}}{\bar{n}_0}, \tag{3.20}$$

with

$$\delta\bar{n}(\mathbf{x}) = \int_0^\infty \int_{-\infty}^\infty \left[\frac{1}{2\pi} \int_0^{2\pi} \delta\bar{f}(\mathbf{R} = \mathbf{x} - \boldsymbol{\rho}(\mu, \varphi), v_\parallel, \mu) d\varphi \right] B dv_\parallel d\mu \tag{3.21}$$

$$\bar{n}_0(\mathbf{x}_\perp) \approx \int_0^\infty \int_{-\infty}^\infty \bar{f}_0(\mathbf{x}_\perp, v_\parallel, \mu) B dv_\parallel d\mu, \tag{3.22}$$

and assuming $\mathcal{N}_e = \bar{n}_0$. In Eq.(3.22), we have again assumed that the equilibrium distribution function varies on a length scale much longer than an average ion gyro-radius. The closed system of equations for the GK model is then Eq.(3.1), Eq.(3.18), and Eqs.(3.20)–(3.22) once a form for $\bar{f}_0$ has been selected. Again, we choose the local Maxwellian distribution with gradients along $\mathbf{e}_1$ for $\bar{f}_0$ given by Eq.(3.12). Then, the right hand side of Eq.(3.18) is given by

$$\frac{q_i}{T_i} v_\parallel \hat{\mathbf{b}} \cdot \langle \mathbf{E} \rangle \bar{f}_0 - \frac{\langle E_y \rangle}{B} \left[\frac{\partial \ln \mathcal{N}_i}{\partial R_x} + \frac{\partial \ln T_i}{\partial R_x} \left(\frac{K}{T_i} - \frac{3}{2} \right) \right] \bar{f}_0, \tag{3.23}$$

and Eq.(3.22) yields simply $\bar{n}_0 \approx \mathcal{N}_i$.

3.2 Slab ITG Dispersion Relations

Next, we take on the task of deriving dispersion relations for the FK and GK ion models presented in the previous section. We consider a perturbation propagating perpendicular to the equilibrium gradients as illustrated in Figure 3.1, taking a plane wave ansatz for the perturbed quantities as

$$\psi(\mathbf{x},t) = \psi(\mathbf{k},\omega)e^{i(\mathbf{k}\cdot\mathbf{x}-\omega t)}, \tag{3.24}$$

where $\mathbf{k}$ has components in the $\mathbf{e}_2$ and $\hat{\mathbf{b}}$ directions as

$$\mathbf{k} = k_\perp \mathbf{e}_2 + k_\parallel \hat{\mathbf{b}}. \tag{3.25}$$

The dispersion relations provide the linear theory which we use to verify our simulations. In addition, we show that for low frequency waves, the GK dispersion relation can be recovered from the FK dispersion relation to first order in the GK ordering.

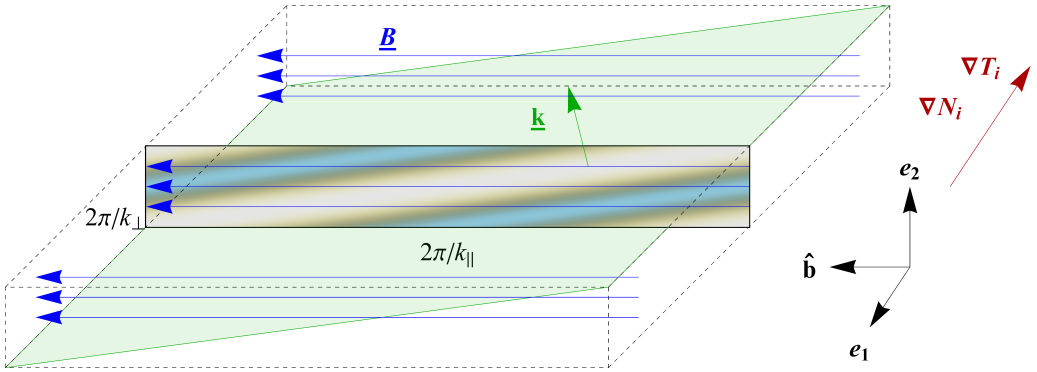

Figure 3.1: 2D Slab Domain

3.2.1 Fully Kinetic Ion Dispersion Relation

Assuming a small amplitude perturbation, Eq.(3.6) with the drive terms from the local Maxwellian given in Eq.(3.13) is linearized as

$$\frac{\partial}{\partial t}\delta f + \mathbf{v}\cdot\nabla\delta f + \frac{q_i}{m_i}(\mathbf{v}\times\mathbf{B})\cdot\nabla_{\mathbf{v}}\delta f = \frac{q_i}{T_i}\mathbf{v}\cdot\mathbf{E}f_0 - \frac{E_y}{B}\left[\frac{\partial \ln \mathcal{N}_i}{\partial R_x} + \frac{\partial \ln T_i}{\partial R_x}\left(\frac{K}{T_i}-\frac{3}{2}\right)\right]f_0. \tag{3.26}$$

Furthermore, we take $\frac{\partial \ln \mathcal{N}_i}{\partial R_x}$, $\frac{\partial \ln T_i}{\partial R_x}$, T_i, and $\mathcal{N}_i$ to be constant, considering the propagation local to a 2D slice at a fixed $x = x_0$ coordinate. From the assumption that the equilibrium varies on length scales which are long compared to the ion gyro-radius, we may also take R_x to be fixed as $R_x \approx x_0$. We denote the constant gradient values by

$$\begin{aligned} \kappa_{\mathcal{N}} &= -\frac{\partial \ln \mathcal{N}_i}{\partial R_x}\bigg|_{R_x=x_0} \\ \kappa_T &= -\frac{\partial \ln T_i}{\partial R_x}\bigg|_{R_x=x_0} \end{aligned} \tag{3.27}$$

and now use T_i and $\mathcal{N}_i$ to represent the constant values of temperature and density, respectively, at $R_x = x_0$. With this notation, we now write Eq.(3.26) as

$$\frac{\partial}{\partial t}\delta f + \mathbf{v}\cdot\nabla\delta f + \frac{q_i}{m_i}(\mathbf{v}\times\mathbf{B})\cdot\nabla_{\mathbf{v}}\delta f = \frac{q_i}{T_i}\mathbf{E}\cdot\mathbf{v}f_0 + \frac{E_y}{B}\left[\kappa_{\mathcal{N}} + \kappa_T\left(\frac{m_i v^2}{2T_i} - \frac{3}{2}\right)\right] f_0. \tag{3.28}$$

It is convenient to express the Cartesian velocity components in cylindrical coordinates as

$$\mathbf{v} = v_\perp \cos\varphi \mathbf{e}_1 + v_\perp \sin\varphi \mathbf{e}_2 + v_\parallel \hat{\mathbf{b}}.$$

Using this expression and assuming the ansatz of Eq.(3.24) in Eq.(3.28), we have

$$i\left(\omega - g(\varphi)\right)\delta f + \Omega_i \frac{\partial}{\partial\varphi}\delta f = iS(\varphi) f_0, \tag{3.29}$$

where

$$\begin{aligned} g(\varphi) &= k_\perp v_\perp \sin\varphi + k_\parallel v_\parallel \\ S(\varphi) &= \frac{q_i\phi(\mathbf{k},\omega)}{T_i}\left[k_\perp v_\perp \sin\varphi + k_\parallel v_\parallel + \frac{T_i k_\perp}{q_i B}\left(\kappa_{\mathcal{N}} + \kappa_T\left(\frac{m_i v^2}{2T_i} - \frac{3}{2}\right)\right)\right], \end{aligned}$$

and the ion gyro-frequency is $\Omega_i = q_i B/m_i$. Equation (3.29) can be solve using an integrating factor, yielding

$$\delta f(\varphi) = i\frac{f_0}{\Omega_i}\int^{\varphi} S(\varphi') e^{i\frac{\omega}{\Omega_i}(\varphi'-\varphi)} e^{i\int_{\varphi'}^{\varphi}\frac{g(\varphi'')}{\Omega_i}d\varphi''} d\varphi'.$$

Explicitly computing the integrals in this expression yields, after much algebra,

$$\begin{aligned} \delta f = \frac{q_i\phi}{T_i} f_0 \sum_{n=-\infty}^{\infty}\sum_{m=-\infty}^{\infty} i^{n-m} e^{i(m+n)\varphi} J_m\left(\frac{k_\perp v_\perp}{\Omega_i}\right) J_n\left(\frac{k_\perp v_\perp}{\Omega_i}\right)\left[\frac{k_\parallel v_\parallel}{\omega - k_\parallel v_\parallel + n\Omega_i} + \right. \\ \left. i\frac{k_\perp v_\perp}{2}\left(\frac{e^{-i\varphi}}{\omega - k_\parallel v_\parallel + (n-1)\Omega_i} - \frac{e^{i\varphi}}{\omega - k_\parallel v_\parallel + (n+1)\Omega_i}\right) + \frac{T_i k_\perp}{q_i B}\frac{\kappa_{\mathcal{N}} + \kappa_T\left(\frac{m_i v^2}{2T_i} - \frac{3}{2}\right)}{\omega - k_\parallel v_\parallel + n\Omega_i}\right]. \end{aligned} \tag{3.30}$$

In obtaining Eq.(3.30), we have made use of the Jacobi-Anger expansion [45] given by

$$e^{iz\cos\theta} = \sum_{n=-\infty}^{\infty} i^n J_n(z) e^{in\theta},$$

where $J_n(z)$ is the n^{th} Bessel function of the first kind. Next, the perturbed number density is obtained by Eq.(3.10), which in the cylindrical velocity coordinates is

$$\delta n = \int_{-\infty}^{\infty}\int_{0}^{\infty}\int_{0}^{2\pi} \delta f v_\perp d\varphi dv_\perp dv_\parallel.$$

Performing the integration and simplifying yields

$$\begin{aligned}\delta n =& \frac{q_i\phi}{T_i} n_0 \Bigg[k_\perp \rho_i \frac{\kappa_T}{\sqrt{2}k_\parallel} \left(\sum_{n=-\infty}^{\infty} b\left(\Gamma_n(b) - \Gamma_{n+1}(b)\right) Z(\zeta_n) - \frac{1}{4}\Gamma_n(b) Z''(\zeta_n) - n\Gamma_n(b) Z(\zeta_n) \right) \\ & - k_\perp \rho_i \frac{\kappa_{\mathcal{N}}}{\sqrt{2}k_\parallel} \sum_{n=-\infty}^{\infty} \Gamma_n(b) Z(\zeta_n) + \frac{1}{2}\sum_{n=-\infty}^{\infty} \Gamma_n(b) Z'(\zeta_n) + \frac{1}{\sqrt{2}k_\parallel \rho_i} \sum_{n=-\infty}^{\infty} n\Gamma_n(b) Z(\zeta_n) \Bigg].\end{aligned} \tag{3.31}$$

In expressing Eq.(3.31) we have adopted the following notation

$$b \equiv \left(k_\perp \rho_i\right)^2, \qquad \zeta_n \equiv \frac{\omega + n\Omega_i}{\sqrt{2}k_\parallel v_{th}}$$

and have defined the ion thermal velocity by $v_{th} = \sqrt{T_i/m_i}$ and the thermal ion gyro-radius by $\rho_i = v_{th}/\Omega_i$. Furthermore, Z is the plasma dispersion function of Fried and Conte [46] and $\Gamma_n(b) \equiv I_n(b)e^{-b}$, where I_n is the n^{th} modified Bessel function of the first kind [45]. Finally, closure is provided with Eq.(3.11) yielding the dispersion relation for the FK ion model:

$$\begin{aligned}\varepsilon_{FK}(\mathbf{k},\omega) = 1 &- \underbrace{\theta k_\perp \rho_i \frac{\kappa_T}{\sqrt{2}k_\parallel} \left[\sum_{n=-\infty}^{\infty} b\left(\Gamma_n(b) - \Gamma_{n+1}(b)\right) Z(\zeta_n) - \frac{1}{4}\Gamma_n(b) Z''(\zeta_n) - n\Gamma_n(b) Z(\zeta_n) \right]}_{\text{Temperature Gradient}} \\ &+ \underbrace{\theta k_\perp \rho_i \frac{\kappa_{\mathcal{N}}}{\sqrt{2}k_\parallel} \sum_{n=-\infty}^{\infty} \Gamma_n(b) Z(\zeta_n)}_{\text{Density Gradient}} - \underbrace{\frac{\theta}{2}\sum_{n=-\infty}^{\infty} \Gamma_n(b) Z'(\zeta_n)}_{\text{Ion Acoustic}} - \underbrace{\frac{\theta}{\sqrt{2}k_\parallel \rho_i} \sum_{n=-\infty}^{\infty} n\Gamma_n(b) Z(\zeta_n)}_{\text{Polarization}} = 0,\end{aligned} \tag{3.32}$$

where $\theta = q_i T_e / e T_i$, and each term is labelled according to its underlying physics.

3.2.2 Gyrokinetic Ion Dispersion Relation

Linearizing Eq.(3.18) and assuming the drive terms from the local Maxwellian given in Eq.(3.23), we have

$$\frac{\partial}{\partial t}\delta\bar{f} + v_\parallel \hat{\mathbf{b}}\cdot\frac{\partial}{\partial \mathbf{R}}\delta\bar{f} = \frac{q_i}{T_i}v_\parallel \hat{\mathbf{b}}\cdot\langle\mathbf{E}\rangle\bar{f}_0 - \frac{\langle E_y\rangle}{B}\left[\frac{\partial \ln \mathcal{N}_i}{\partial R_x} + \frac{\partial \ln T_i}{\partial R_x}\left(\frac{K}{T_i}-\frac{3}{2}\right)\right]\bar{f}_0.$$

Taking again the local approximation for the equilibrium quantities, we have

$$\frac{\partial}{\partial t}\delta\bar{f} + v_\parallel \hat{\mathbf{b}}\cdot\frac{\partial}{\partial \mathbf{R}}\delta\bar{f} = \frac{q_i}{T_i}v_\parallel \hat{\mathbf{b}}\cdot\langle\mathbf{E}\rangle\bar{f}_0 + \frac{\langle E_y\rangle}{B}\left[\kappa_{\mathcal{N}} + \kappa_T\left(\frac{m_i v^2}{2T_i}-\frac{3}{2}\right)\right]\bar{f}_0, \tag{3.33}$$

with $\kappa_{\mathcal{N}}$ and κ_T defined in Eq.(3.27) and with gradients decreasing along $\mathbf{e}_1$. A plane wave ansatz in the guiding center coordinates is taken for perturbed quantities as

$$\psi(\mathbf{R},t) = \psi(\mathbf{k},\omega)e^{i(\mathbf{k}\cdot\mathbf{R}-\omega t)}, \tag{3.34}$$

with $\mathbf{k}$ as in Eq.(3.25). Plugging this form into Eq.(3.33) gives without difficulty

$$\delta\bar{f}_i = \frac{q_i\langle\phi\rangle}{T_i}\bar{f}_0\left[\frac{k_\parallel v_\parallel}{\omega - k_\parallel v_\parallel} + \frac{T_i k_\perp}{q_i B}\frac{\kappa_{\mathcal{N}} + \kappa_T\left(\frac{m_i(v_\parallel^2+2\mu B)}{2T_i}-\frac{3}{2}\right)}{\omega - k_\parallel v_\parallel}\right].$$

Next, we consider the integral contained in the brackets of Eq.(3.21). For $\delta\bar{f}$ taking the plane wave form of Eq.(3.34), we have

$$\frac{1}{2\pi}\int_0^{2\pi}\delta\bar{f}_i(\mathbf{k})e^{i\mathbf{k}\cdot(\mathbf{x}-\boldsymbol{\rho}(\varphi))}d\varphi = \delta\bar{f}_i(\mathbf{k})e^{i\mathbf{k}\cdot\mathbf{x}}\left(\frac{1}{2\pi}\int_0^{2\pi}e^{-i\mathbf{k}\cdot\boldsymbol{\rho}(\varphi)}d\varphi\right).$$

Using Eq.(3.15) and Eq.(3.25), the integral on the right hand side can be written as

$$\frac{1}{2\pi}\int_0^{2\pi}e^{-i\frac{k_\perp\sqrt{2\mu B}}{\Omega_i}\cos\varphi}d\varphi = J_0\left(\frac{k_\perp\sqrt{2\mu B}}{\Omega_i}\right),$$

where the second expression follows from an integral identity of J_0 [45]. Returning to Eq.(3.21), we have

$$\delta\bar{n} = \int_0^\infty\int_{-\infty}^\infty \frac{q_i\langle\phi\rangle}{T_i}\bar{f}_0\left[\frac{k_\parallel v_\parallel}{\omega - k_\parallel v_\parallel} + \frac{T_i k_\perp}{q_i B}\frac{\kappa_{\mathcal{N}} + \kappa_T\left(\frac{m_i(v_\parallel^2+2\mu B)}{2T_i}-\frac{3}{2}\right)}{\omega - k_\parallel v_\parallel}\right]J_0\left(\frac{k_\perp\sqrt{2\mu B}}{\Omega_i}\right)B dv_\parallel d\mu. \tag{3.35}$$

Assuming ϕ varies as Eq.(3.24) and using Eq.(3.16), we have for the gyro-averaged electrostatic potential

$$\langle \phi(\mathbf{k}) e^{i\mathbf{k}\cdot\mathbf{x}} \rangle = \frac{1}{2\pi} \int_0^{2\pi} \phi(\mathbf{k}) e^{i\mathbf{k}\cdot(\mathbf{R}+\boldsymbol{\rho}(\varphi))} d\varphi = \phi(\mathbf{k}) e^{i\mathbf{k}\cdot\mathbf{x}} \left(\frac{1}{2\pi} \int_0^{2\pi} e^{i\mathbf{k}\cdot\boldsymbol{\rho}(\varphi)} d\varphi \right).$$

Again, we use Eq.(3.15) and Eq.(3.25) to express the integral on the right hand side as

$$\frac{1}{2\pi} \int_0^{2\pi} e^{i\frac{k_\perp \sqrt{2\mu B}}{\Omega_i} \cos\varphi} d\varphi = J_0 \left(\frac{k_\perp \sqrt{2\mu B}}{\Omega_i} \right).$$

Now, we write Eq.(3.35) as

$$\delta\bar{n} = \frac{q_i \phi}{T_i} \int_0^\infty \int_{-\infty}^\infty \bar{f}_0 \left[\frac{k_\parallel v_\parallel}{\omega - k_\parallel v_\parallel} + \frac{T_i k_\perp}{q_i B} \frac{\kappa_\mathcal{N} + \kappa_T \left(\frac{m_i (v_\parallel^2 + 2\mu B)}{2T_i} - \frac{3}{2} \right)}{\omega - k_\parallel v_\parallel} \right] J_0^2 \left(\frac{k_\perp \sqrt{2\mu B}}{\Omega_i} \right) B dv_\parallel d\mu,$$

which after integration, yields

$$\delta\bar{n} = \frac{q_i \phi}{T_i} \bar{n}_0 \Bigg[k_\perp \rho_i \frac{\kappa_T}{\sqrt{2} k_\parallel} \left(b \left(\Gamma_0(b) - \Gamma_1(b) \right) Z(\zeta) - \frac{1}{4} \Gamma_0(b) Z''(\zeta) \right) - k_\perp \rho_i \frac{\kappa_\mathcal{N}}{\sqrt{2} k_\parallel} \Gamma_0(b) Z(\zeta) + \frac{1}{2} \Gamma_0(b) Z'(\zeta) \Bigg],$$

where $\zeta = \frac{\omega/\Omega_i}{\sqrt{2} k_\parallel \rho_i}$. Closure is provided by Eq.(3.20), which can be expressed as

$$\frac{e\phi}{T_e} + \frac{q_i \phi}{T_i} \left(1 - \Gamma_0(b) \right) = \frac{\delta\bar{n}_i}{\bar{n}_0},$$

from Eq.(3.24) and integration over the gyro-phase. Finally, we obtain the GK ion dispersion relation as

$$\varepsilon_{GK}(\mathbf{k}, \omega) = 1 - \underbrace{\theta k_\perp \rho_i \frac{\kappa_T}{\sqrt{2} k_\parallel} \left[b \left(\Gamma_0(b) - \Gamma_1(b) \right) Z(\zeta) - \frac{1}{4} \Gamma_0(b) Z''(\zeta) \right]}_{\text{Temperature Gradient}} + \underbrace{\theta k_\perp \rho_i \frac{\kappa_n}{\sqrt{2} k_\parallel} \Gamma_0(b) Z(\zeta)}_{\text{Density Gradient}} - \underbrace{\frac{\theta}{2} \Gamma_0(b) Z'(\zeta)}_{\text{Ion Acoustic}} + \underbrace{\theta \left(1 - \Gamma_0(b) \right)}_{\text{Polarization}} = 0. \tag{3.36}$$

3.2.3 Comparison of Dispersion Relations

Here, we show that the FK dispersion relation reduces to the GK dispersion relation under the GK ordering assumptions. The GK ordering assumptions relevant to the electrostatic slab ITG

model are [6, 9]

$$\frac{\omega}{\Omega_i} \sim k_\parallel \rho_i \sim \frac{\rho_i}{L_{eq}} \sim O(\epsilon) \tag{3.37}$$

$$k_\perp \rho_i \sim O(1),$$

where L_{eq} is a characteristic length scale on which equilibrium quantities are assumed to vary. For our purposes, the ordering assumption on the equilibrium length scale corresponds to $\kappa_{\mathcal{N}} \rho_i \sim \kappa_T \rho_i \sim O(\epsilon)$. Notice that the terms in Eq.(3.32) involve the plasma dispersion function, along with its first two derivatives, evaluated at ζ_n. Using the definition of ρ_i, we can write ζ_n in terms of the ordering parameters given above as

$$\zeta_n = \frac{\omega/\Omega_i}{\sqrt{2} k_\parallel \rho_i} + \frac{n}{\sqrt{2} k_\parallel \rho_i},$$

from which it clear that the first term is $O(1)$ and for $n \neq 0$ the second term is $O(\epsilon^{-1})$ in the GK ordering. Hence, the large argument expansion of the plasma dispersion function, given by

$$Z(w) \sim i\sigma\sqrt{\pi} e^{-w^2} - \frac{1}{w} - \frac{1}{2w^2} + ... \qquad |w| \gg 1, \tag{3.38}$$

where

$$\sigma \equiv \begin{cases} 0 : \mathrm{Im}(w) > 0 \\ 1 : \mathrm{Im}(w) = 0 \\ 2 : \mathrm{Im}(w) < 0 \end{cases}$$

is appropriate for $n \neq 0$. Furthermore, since $|\mathrm{Re}(\zeta_n)| \gg 1$, we may neglect the exponential term in Eq.(3.38) yielding from the second term

$$Z(\zeta_n) \sim -\frac{\sqrt{2} k_\parallel \rho_i}{n} \frac{1}{1 + \frac{\omega}{n\Omega_i}} + O(\epsilon^2), \qquad n \neq 0.$$

An additional expansion is made in $\omega/n\Omega_i$ yielding simply

$$Z(\zeta_n) \sim -\frac{\sqrt{2} k_\parallel \rho_i}{n} + O(\epsilon^2) \qquad n \neq 0. \tag{3.39}$$

Taking similar expansions for Z' and Z'' shows

$$Z'(\zeta_n) \sim O(\epsilon^2) \tag{3.40}$$

$$Z''(\zeta_n) \sim O(\epsilon^3) \qquad n \neq 0. \tag{3.41}$$

We first consider the term in Eq.(3.32), resulting from the temperature gradient

$$-\theta k_\perp \rho_i \frac{\kappa_T}{\sqrt{2}k_\parallel}\left[\sum_{n=-\infty}^{\infty} b\left(\Gamma_n(b)-\Gamma_{n+1}(b)\right)Z(\zeta_n)-\frac{1}{4}\Gamma_n(b)Z''(\zeta_n)-n\Gamma_n(b)Z(\zeta_n)\right].$$

Our expansions in Eqs.(3.39)–(3.41) show this to reduce to

$$-\theta k_\perp \rho_i \frac{\kappa_T}{\sqrt{2}k_\parallel}\left[b\left(\Gamma_0(b)-\Gamma_1(b)\right)Z(\zeta)-\frac{1}{4}\Gamma_0(b)Z''(\zeta)\right]- \theta(k_\perp\rho_i)(\kappa_T\rho_i)\sum_{n\neq 0}\left[-b\frac{\Gamma_n(b)}{n}+b\frac{\Gamma_{n+1}(b)}{n}+\Gamma_n(b)\right]+O(\epsilon^2). \tag{3.42}$$

The following identities of the modified Bessel function [45] are useful for evaluating the summation in Eq.(3.42):

$$I_n(w)=I_{-n}(w) \tag{3.43}$$

$$I_{n-1}(w)-I_{n+1}(w)=\frac{2n}{w}I_n(w) \tag{3.44}$$

$$I_0(w)+2\sum_{n=1}^{\infty}I_n(w)=e^w. \tag{3.45}$$

Considering the first term of the sum in Eq.(3.42), we have

$$\sum_{n\neq 0}\frac{\Gamma_n(b)}{n}=\sum_{n=1}^{\infty}e^{-b}\frac{I_n(b)}{n}-\sum_{n=1}^{\infty}e^{-b}\frac{I_{-n}(b)}{n}=0, \tag{3.46}$$

where the last equality follows from Eq.(3.43). For the second term, we have

$$\sum_{n\neq 0}\frac{\Gamma_{n+1}(b)}{n}=\sum_{n=1}^{\infty}e^{-b}\frac{\left(I_{n+1}(b)-I_{n-1}(b)\right)}{n}= -\frac{2e^{-b}}{b}\sum_{n=1}^{\infty}I_n(b)=-\frac{e^{-b}}{b}\left(e^b-I_0(b)\right)=\frac{\Gamma_0(b)-1}{b}$$

making use of Eqs.(3.43)–(3.45). For the third term, we have

$$\sum_{n\neq 0}\Gamma_n(b)=2e^{-b}\sum_{n=1}^{\infty}I_n(b)=e^{-b}\left(e^b-I_0(b)\right)=1-\Gamma_0(b), \tag{3.47}$$

using Eq.(3.43) and Eq.(3.45). With these expressions for the sums in Eq.(3.42), there is a cancellation of terms, and we are left with

$$-\theta k_\perp \rho_i \frac{\kappa_T}{\sqrt{2}k_\parallel}\left[b\left(\Gamma_0(b)-\Gamma_1(b)\right)Z(\zeta)-\frac{1}{4}\Gamma_0(b)Z''(\zeta)\right]+O(\epsilon^2),$$

which is identical to the temperature gradient term of Eq.(3.36). Next, the term in Eq.(3.32) resulting from the density gradient is

$$\theta k_\perp \rho_i \frac{\kappa_\mathcal{N}}{\sqrt{2}k_\parallel} \sum_{n=-\infty}^{\infty} \Gamma_n(b) Z(\zeta_n),$$

which from Eq.(3.39) and Eq.(3.46) reduces to

$$\theta k_\perp \rho_i \frac{\kappa_\mathcal{N}}{\sqrt{2}k_\parallel} \Gamma_0(b) Z(\zeta) + O(\epsilon^2),$$

the density gradient term of Eq.(3.36). The ion acoustic term in Eq.(3.32) is

$$-\frac{\theta}{2} \sum_{n=-\infty}^{\infty} \Gamma_n(b) Z'(\zeta_n),$$

giving the correct reduction of

$$-\frac{\theta}{2} \Gamma_0(b) Z'(\zeta) + O(\epsilon^2),$$

using Eq.(3.40). Finally, the polarization term in Eq.(3.32) is

$$-\frac{\theta}{\sqrt{2}k_\parallel \rho_i} \sum_{n=-\infty}^{\infty} n\Gamma_n(b) Z(\zeta_n),$$

reducing to

$$\theta \left(1 - \Gamma_0(b)\right) + O(\epsilon^2)$$

from Eq.(3.39) and Eq.(3.47). Again, this matches with the polarization term in Eq.(3.32), and we conclude that

$$\varepsilon_{FK}(\mathbf{k}, \omega) - \varepsilon_{GK}(\mathbf{k}, \omega) \sim O(\epsilon^2).$$

This shows that the low frequency normal modes in the GK ion model are present in the FK ion model as well.

3.2.4 Low Frequency Normal Modes

Here, we examine the low frequency normal modes present in the GK and FK ion models by examining Eq.(3.36). Specifically, we consider the effects of $\kappa_\mathcal{N}$, κ_T, and $k_\perp \rho_i$ on the ion acoustic

wave. Setting these parameters to be zero, we are left with the dispersion relation for ion acoustic waves propagating parallel to the magnetic field

$$1 - \frac{\theta}{2} Z'(\zeta) = 0. \tag{3.48}$$

The simplest study of ion acoustic waves comes from considering Eq.(3.48) in the limit $\mathrm{Im}(\omega) \to 0$ and $\mathrm{Re}(\omega) \gg k_\parallel v_{th}$. In this case, the lowest order term in the large argument expansion of Z' gives simply

$$Z'(\zeta) \sim \frac{1}{\zeta^2},$$

yielding dispersionless waves travelling in opposite directions along the magnetic field as

$$\omega = \pm \sqrt{\frac{q_i T_e}{e m_i}} k_\parallel,$$

where we have used the definitions of ζ, θ, and T_i to simplify this expression. A more careful treatment of Eq.(3.48) reveals solutions to have finite negative values of $\mathrm{Im}\{\omega\}$, corresponding to waves which are exponentially decaying in time [2, 24, 25]. This decay is a result of a collisionless process known as ion Landau damping, in which ions with velocities $\sim \omega/k_\parallel$ resonate with the wave, drawing energy from it.

The next level of detail we look at is the inclusion of wavenumber components which are perpendicular to the magnetic field. A wave with finite $k_\perp$ generates a time varying component of the electric field perpendicular to the magnetic field. Polarization of the plasma then occurs due mainly to the displacement of ions in the direction of the perpendicular electric field. In addition, there are effects due to the ions experiencing variations in the electric field as they gyrate about their guiding center. These are known as finite Larmor radius (FLR) effects and can lead to important corrections to the dispersive properties of drift instabilities. Still considering for now $\kappa_T = \kappa_\mathcal{N} = 0$, we have the dispersion relation for the ion acoustic wave including polarization and FLR effects as

$$1 - \frac{\theta}{2} \Gamma_0(b) Z'(\zeta) + \theta \left(1 - \Gamma_0(b)\right) = 0. \tag{3.49}$$

A numerical solution to Eq.(3.49) is shown in Figure 3.2 for $\theta = 4.0$ and $k_\parallel \rho_i = 2 \times 10^{-3}$. It is seen that increasing $k_\perp \rho_i$ results in lowering the magnitude of the real frequency $\omega_R \equiv \mathrm{Re}(\omega)$ and

decreasing the imaginary part of the frequency $\gamma \equiv \mathrm{Im}(\omega)$ (damping/growth rate). Both branches of the ion acoustic wave have the same damping rate when no equilibrium gradients are present.

The inclusion of equilibrium gradients in the model results in significant deformation of the branches of the ion acoustic wave. Figure 3.2 shows that the inclusion of an equilibrium temperature gradient causes the sound wave travelling in the direction of $-\mathbf{e}_2$ to become unstable as $k_\perp \rho_i$ is increased. Further deformation occurs with the inclusion of an equilibrium density gradient, as illustrated in Figure 3.3. Here, the density gradient acts to reduce the growth rate of the unstable branch, while bringing the stable branch near marginal stability.

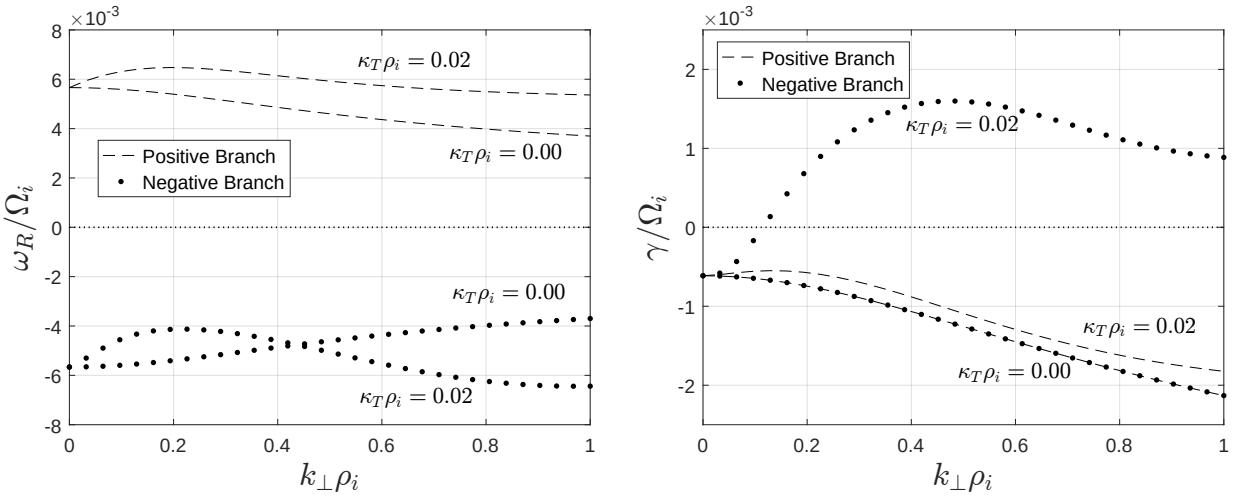

Figure 3.2: Deformation of the ion acoustic wave from the inclusion of a temperature gradient.

3.2.5 Ion Bernstein Modes

Now, we examine the ion Bernstein modes [44], which are unique to the FK ion model. The ion Bernstein modes have frequencies near the harmonics of the ion gyro-frequency. Since gyrokinetics analytically eliminates the gyro-frequency time scale, the ion Bernstein modes do not appear in the GK ion model. We consider the simplest setting in which the ion Bernstein modes appear by taking $\kappa_T = \kappa_{\mathcal{N}} = 0$ and taking the propagation to be exactly perpendicular to the

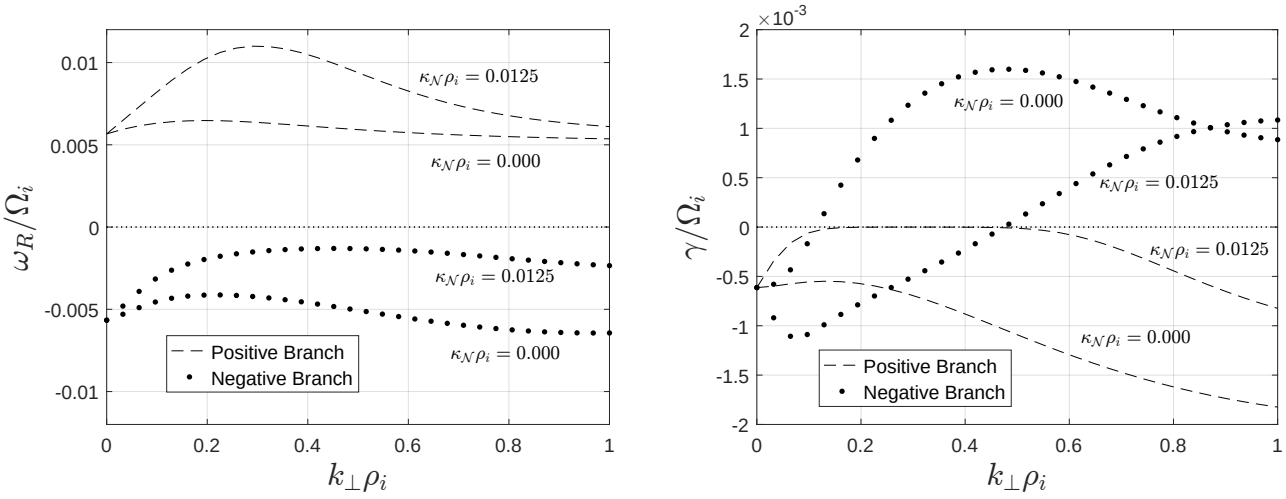

Figure 3.3: Effects of the density gradient on the ITG mode.

magnetic field, i.e. $k_\parallel \to 0$, in the dispersion relation Eq.(3.32). In this limit, we are left with

$$1 + \theta \sum_{n=-\infty}^{\infty} \frac{n\Omega_i \Gamma_n(b)}{\omega + n\Omega_i} = 0,$$

where the second term is due to the ion polarization response. The summation can be simplified to give

$$1 - 2\theta \sum_{n=1}^{\infty} \frac{n^2\Omega_i^2 \Gamma_n(b)}{\omega^2 - n^2\Omega_i^2} = 0. \tag{3.50}$$

Next, we write out the first few terms of the sum explicitly as

$$\frac{1}{2\theta\Omega_i^2} = \frac{\Gamma_1(b)}{\omega^2 - \Omega_i^2} + \frac{2^2\Gamma_2(b)}{\omega^2 - 2^2\Omega_i^2} + \frac{3^2\Gamma_3(b)}{\omega^2 - 3^2\Omega_i^2} + ...$$

and consider the limit $k_\perp\rho_i \ll 1$, which allows the small argument expansion of Γ_n, given by

$$\Gamma_n(b) \approx \left(\frac{b}{2}\right)^n \left(\frac{1-b}{n!} + ...\right).$$

Expanding to $O(b^2)$ will allow us to obtain the first two Bernstein modes. We have

$$\frac{1}{2\theta\Omega_i^2} = \frac{b}{2}\frac{1}{\omega^2 - \Omega_i^2} + \frac{b^2}{2}\left(\frac{1}{\omega^2 - 4\Omega_i^2} - \frac{1}{\omega^2 - \Omega_i^2}\right) + O(b^3)$$

For the first Bernstein mode, we need only $O(b)$ terms to give

$$\left(\omega^2 - \Omega_i^2\right) \frac{1}{2\theta\Omega_i^2} = \frac{b}{2} + O(b^2).$$

Assuming $\omega = \omega_0 + b\omega_1 + ...$, we have

$$\left(\omega_0^2 + 2b\omega_0\omega_1 - \Omega_i^2\right) \frac{1}{2\theta\Omega_i^2} = \frac{b}{2} + O(b^2).$$

Collecting powers of b, at zeroth order,

$$\omega_0^2 - \Omega_i^2 = 0,$$

yielding $\omega_0 = \pm\Omega_i$. At first order,

$$\frac{2\omega_0\omega_1}{\theta\Omega_i^2} = 1,$$

which gives the correction

$$\omega_1 = \pm\frac{\theta}{2}\Omega_i.$$

Hence the frequency of the first ion Bernstein mode is

$$\omega_{B1} = \pm\Omega_i \pm \frac{\theta}{2}\Omega_i \left(k_\perp\rho_i\right)^2 + O\left(k_\perp\rho_i\right)^4. \tag{3.51}$$

A similar analysis is used to obtain the second ion Bernstein mode, beginning with

$$\left(\omega^2 - 4\Omega_i^2\right) \frac{1}{2\theta\Omega_i^2} = \frac{b}{2}\frac{\omega^2 - 4\Omega_i^2}{\omega^2 - \Omega_i^2} + \frac{b^2}{2}\left(1 - \frac{\omega^2 - 4\Omega_i^2}{\omega^2 - \Omega_i^2}\right) + O(b^3). \tag{3.52}$$

We again assume $\omega = \omega_0 + b\omega_1 + b^2\omega_2 + ...$ Plugging this form into Eq.(3.52), expanding, and collecting powers of b, we have at zeroth order

$$\omega_0^2 - 4\Omega_i^2 = 0,$$

yielding $\omega_0 = \pm 2\Omega_i$. At first order, we find $\omega_1 = 0$. Finally, the second order equation is

$$\frac{2\omega_0\omega_2}{\theta\Omega_i^2} = 1,$$

giving the correction

$$\omega_2 = \pm\frac{\theta\Omega_i}{4}.$$

Hence the frequency of the second ion Bernstein mode is

$$\omega_{B2} = \pm 2\Omega_i \pm \frac{\theta \Omega_i}{4} \left(k_\perp \rho_i\right)^4 + O\left(k_\perp \rho_i\right)^6 . \tag{3.53}$$

The higher frequency ion Bernstein modes may be found similarly by expanding Eq.(3.50) to higher orders in b. It is noted that the Bernstein modes have purely real frequencies, that is, they are neither growing nor decaying in time. Figure 3.4 shows the dispersion of the first four ion Bernstein modes from numerically solving Eq.(3.50), along with the frequencies from the analytical expressions Eq.(3.51) and Eq.(3.53). The effects of the ion Bernstein modes on FK ion simulations

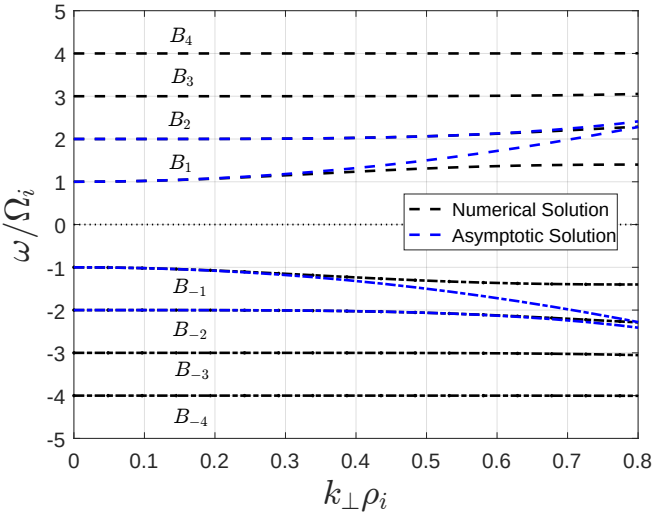

Figure 3.4: Dispersion of the Ion Bernstein Modes

is examined in more detail in Chapter 4.

3.3 Simulation Results for the FK Slab ITG Model

Here, we use the baseline δf method presented in Chapter 4.3.3 to simulate the linear ITG instability in slab geometry with the FK ion model equations from Eq.(3.1), Eq.(3.28), and Eqs.(3.10)–(3.11). We use the test case from [17] with parameters $\theta = 4.0$, $k_\parallel \rho_i = 2.0 \times 10^{-3}$, $k_\perp \rho_i = 0.2$, $\kappa_\mathcal{N} = 0.0$, and scan over values of $\kappa_T \rho_i$. Figure 3.5 shows the results from simulation

compared with the solutions to both the FK and GK ion dispersion relations given by Eq.(3.32) and Eq.(3.36) respectively. The simulations were performed using $\Delta y = .65\rho_i$, $\Delta z = 65.5\rho_i$, $\Omega_i \Delta t = 0.125$ and 4194304 particles. Excellent agreement is observed between the FK ion simula-

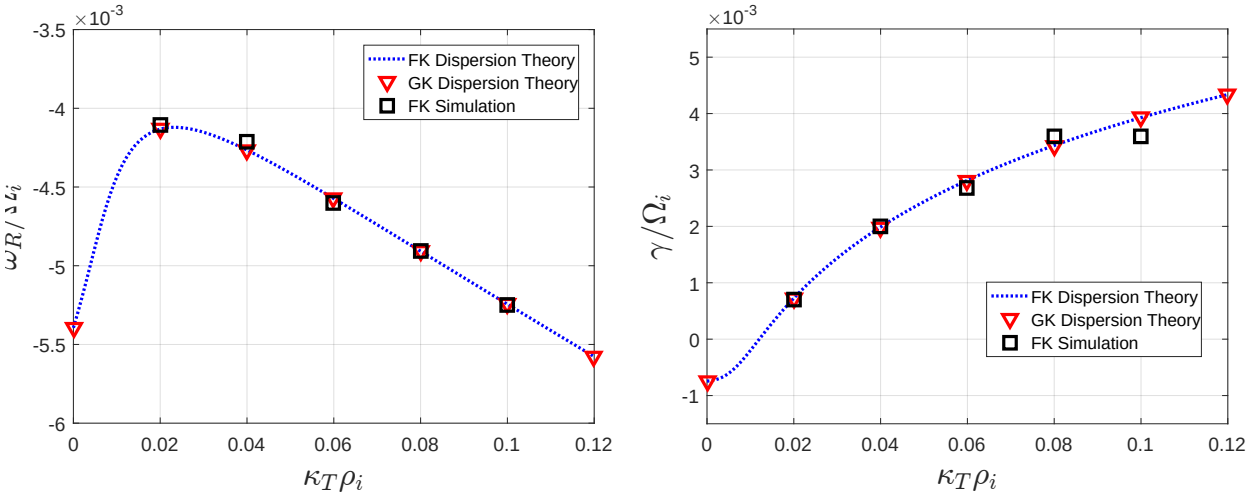

Figure 3.5: Simulation results for the slab ITG FK ion model compared to the dispersion theories from the FK ion model and the GK ion model.

tions, the FK ion dispersion solutions, and the GK ion dispersion relations. Figure 3.6, shows the Fourier mode time history for $\kappa_T \rho_i = 0.02$ from the FK ion simulation. Both the low frequency ITG mode and high frequency ion Bernstein modes are observed.

3.4 Extension to a Weakly Inhomogeneous Magnetic Field

In the previous sections, we considered a model assuming a uniform magnetic field. This allowed us to obtain the constant of motion R_x, which was used to construct an inhomogeneous equilibrium distribution in the FK ion model. Furthermore, the simplicity of the uniform magnetic field assumption allowed us to analyze the linear dispersive properties of both the FK and GK ion models in detail. Guiding center drift motions due to inhomogeneities in the magnetic field, however, can produce important effects which are not present in the uniform magnetic field model.

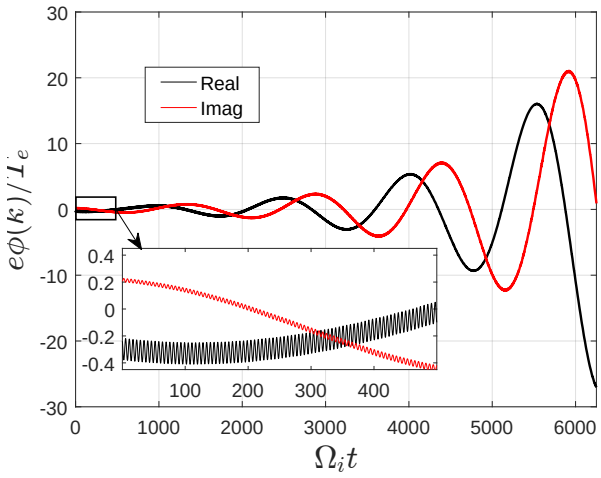

Figure 3.6: Fourier mode time history from the FK ion model simulation with $\kappa_T = 0.02$. Both the low frequency ITG mode and the high frequency ion Bernstein modes are present.

Here, we first present how gyrokinetics includes these drifts in the guiding center dynamics and how equilibrium temperature and density gradients are included in the inhomogeneous magnetic field GK ion model. Fully kinetic ion models require no modification to the particle equations of motion due to magnetic field inhomogeneities. The challenge instead is the inclusion of equilibrium temperature and density gradients. A method for doing this is presented through the construction of an approximate constant of motion, assuming the equilibrium distribution varies on length scales which are large compared to an average gyro-radius.

3.4.1 Gyrokinetic Ion Model

Gyrokinetic models account for magnetic field inhomogeneities through the inclusion of the magnetic drift terms $\mathbf{v}_d$ in the guiding center equations of motion [9]. Including these terms, the

guiding center of an ion evolves according to

$$\frac{d\mathbf{R}}{dt} = v_\parallel \hat{\mathbf{b}} + \frac{\langle \mathbf{E} \rangle \times \mathbf{B}}{B} + \mathbf{v}_d$$
$$\mathbf{v}_d = \frac{m_i}{q_i}\hat{\mathbf{b}} \times \left[\frac{v_\parallel^2}{B} \left(\hat{\mathbf{b}} \cdot \frac{\partial}{\partial \mathbf{R}} \right) \hat{\mathbf{b}} + \mu \frac{\partial \ln B}{\partial \mathbf{R}} \right],$$

where the first term in $\mathbf{v}_d$ accounts for drifts due to the curvature of the magnetic field and the second term accounts for drift due to gradients in the magnetic field strength. In addition, magnetic field inhomogeneities can be the source of accelerations parallel to the magnetic field. To account for this, the parallel velocity evolves as

$$\frac{dv_\parallel}{dt} = \frac{q_i}{m_i}\langle \mathbf{E} \rangle \cdot \hat{\mathbf{b}} + \langle \mathbf{E} \rangle \cdot \frac{v_\parallel}{B}\hat{\mathbf{b}} \times \left(\hat{\mathbf{b}} \cdot \frac{\partial}{\partial \mathbf{R}} \right) \hat{\mathbf{b}} - \mu B \hat{\mathbf{b}} \cdot \frac{\partial \ln B}{\partial \mathbf{R}}.$$

The GK Vlasov equation for ion guiding centers, including the effects of magnetic field inhomogeneities can be written as

$$\frac{\partial \bar{f}_i}{\partial t} + \frac{d\mathbf{R}}{dt} \cdot \frac{\partial \bar{f}_i}{\partial \mathbf{R}} + \frac{dv_\parallel}{dt}\frac{\partial \bar{f}_i}{\partial v_\parallel},$$

and an equilibrium distribution then satisfies

$$\left(v_\parallel \hat{\mathbf{b}} + \mathbf{v}_d \right) \cdot \frac{\partial \bar{f}_0}{\partial \mathbf{R}} - \mu B \hat{\mathbf{b}} \cdot \frac{\partial \ln B}{\partial \mathbf{R}} \frac{\partial \bar{f}_0}{\partial v_\parallel} = 0.$$

Gyrokinetic ordering for the more general case of inhomogeneous magnetic fields requires in addition to Eq.(3.37),

$$\frac{\rho_i}{L_B} \sim O(\epsilon),$$

where L_B is a characteristic length scale on which the magnetic field varies. With this requirement and $\rho_i / L_{eq} \sim O(\epsilon)$, we have

$$\mathbf{v}_d \cdot \frac{\partial \bar{f}_0}{\partial \mathbf{R}} \sim O(\epsilon^2),$$

and may therefore be neglected in the equilibrium equation. We are left with the simpler equation

$$v_\parallel \hat{\mathbf{b}} \cdot \frac{\partial \bar{f}_0}{\partial \mathbf{R}} - \mu B \hat{\mathbf{b}} \cdot \frac{\partial \ln B}{\partial \mathbf{R}} \frac{\partial \bar{f}_0}{\partial v_\parallel} = 0. \tag{3.54}$$

Now suppose that the guiding center position is described by curvilinear coordinates. Suppose also that one such coordinate, denoted R_χ, has the property

$$\hat{\mathbf{b}} \cdot \frac{\partial R_\chi}{\partial \mathbf{R}} = 0.$$

Then we can use R_χ to construct a solution to Eq.(3.54). In addition, we can use the kinetic energy defined by Eq.(3.17) allowing us to construct solutions to Eq.(3.54) as $\bar{f}_0 = \bar{f}_0(R_\chi, K)$. The perturbed part of the ion guiding center distribution function then evolves according to

$$\frac{\partial}{\partial t}\delta\bar{f} + \frac{d\mathbf{R}}{dt}\cdot\frac{\partial}{\partial \mathbf{R}}\delta\bar{f} + \frac{dv_\parallel}{dt}\frac{\partial}{\partial v_\parallel}\delta\bar{f} = -\frac{\langle\mathbf{E}\rangle\times\hat{\mathbf{b}}}{B}\cdot\frac{\partial R_\chi}{\partial \mathbf{R}}\frac{\partial \bar{f}_0}{\partial R_\chi} - q_i v_\parallel \langle\mathbf{E}\rangle\cdot\tilde{\mathbf{b}}\frac{\partial \bar{f}_0}{\partial K}$$

$$\tilde{\mathbf{b}} \equiv \hat{\mathbf{b}} + \frac{m_i}{q_i}\frac{v_\parallel}{B}\hat{\mathbf{b}}\times\left(\hat{\mathbf{b}}\cdot\frac{\partial}{\partial \mathbf{R}}\hat{\mathbf{b}}\right).$$

3.4.2 Fully Kinetic Ion Model

For the FK ion model, we seek an approximate solution under the assumption that $\epsilon \equiv \rho_i/L_{eq} \ll 1$. Our approach is to construct f_0 from a scalar $R_\chi(\mathbf{x}, \mathbf{v}; \epsilon)$ such that

$$\lim_{\epsilon\to 0^+}\left[\mathbf{v}\cdot\nabla f_0(R_\chi(\mathbf{x},\mathbf{v};\epsilon)) + \frac{q_i}{m_i}(\mathbf{v}\times\mathbf{B})\cdot\nabla_{\mathbf{v}} f_0(R_\chi(\mathbf{x},\mathbf{v};\epsilon))\right] = 0.$$

To be explicit with our ordering assumptions, we use the following nondimensional variables

$$\tilde{\mathbf{x}} \to \frac{\mathbf{x}}{L_{eq}}, \qquad \tilde{\mathbf{v}} \to \frac{\mathbf{v}}{v_{th}}, \qquad \tilde{\mathbf{B}} \to \frac{\mathbf{B}}{B_0},$$

where B_0 is such that

$$\frac{|\mathbf{B}|}{B_0} \sim O(1).$$

Here, we also define ρ_i in terms of B_0 as $\rho_i = m_i v_{th}/q_i B_0$. In the nondimensional variables, and omitting the tildes for simplicity, Eq.(3.4) becomes

$$\epsilon\mathbf{v}\cdot\nabla f_0 + (\mathbf{v}\times\mathbf{B})\cdot\nabla_{\mathbf{v}} f_0 = 0.$$

Plugging in the form $f_0 = f_0(R_\chi(\mathbf{x},\mathbf{v};\epsilon))$ yields

$$\frac{\partial f_0}{\partial R_\chi}\left[\epsilon\mathbf{v}\cdot\nabla R_\chi + (\mathbf{v}\times\mathbf{B})\cdot\nabla_{\mathbf{v}} R_\chi\right] = 0.$$

Hence for f_0 to have nontrivial dependence on R_χ as $\epsilon\to 0$, R_χ must satisfy

$$\lim_{\epsilon\to 0^+}\left[\epsilon\mathbf{v}\cdot\nabla R_\chi(\mathbf{x},\mathbf{v};\epsilon) + (\mathbf{v}\times\mathbf{B})\cdot\nabla_{\mathbf{v}} R_\chi(\mathbf{x},\mathbf{v};\epsilon)\right] = 0. \tag{3.55}$$

We assume a regular perturbation series for R_χ in ϵ as

$$R_\chi = R_\chi^{(0)} + \epsilon R_\chi^{(1)} + \epsilon^2 R_\chi^{(2)} + ...$$

Plugging this form into Eq.(3.55) and collecting powers of ϵ yields a sequence of equations which can be solved successively to increase the rate at which the limit in Eq.(3.55) goes to zero. The sequence of equations is as follows

$$(\mathbf{v} \times \mathbf{B}) \cdot \nabla_\mathbf{v} R_\chi^{(0)} = 0$$
$$(\mathbf{v} \times \mathbf{B}) \cdot \nabla_\mathbf{v} R_\chi^{(i)} = -\mathbf{v} \cdot \nabla R_\chi^{(i-1)},$$

for $i = 1, 2, ...$ At zeroth order, we choose $R_\chi^{(0)} = \chi$, where χ is a curvilinear spatial coordinate such that

$$\nabla\chi \cdot \mathbf{B} = 0.$$

With this choice, the next order equation is

$$(\mathbf{v} \times \mathbf{B}) \cdot \nabla_\mathbf{v} R_\chi^{(1)} = -\mathbf{v} \cdot \nabla\chi,$$

which has the solution

$$R_x^{(1)} = \frac{\mathbf{v} \times \mathbf{B}}{\mathbf{B} \cdot \mathbf{B}} \cdot \nabla\chi.$$

In terms of the dimensional variables, we have

$$R_\chi \approx \chi + \frac{m_i}{q_i} \frac{\mathbf{v} \times \hat{\mathbf{b}}}{B} \cdot \nabla\chi,$$

which is the projection of the χ coordinate of a particles position onto its guiding center. We can now use R_χ to construct an equilibrium distribution that will satisfy Eq.(3.4) to $O(\epsilon)$. Furthermore, the kinetic energy of an ion, given by Eq.(3.5), is an exact constant of motion for an arbitrary magnetic field. We therefore construct our equilibrium distribution as $f_0 = f_0(R_\chi, K)$. With this form, the perturbed part of the distribution evolves as

$$\frac{\partial}{\partial t}\delta f + \mathbf{v} \cdot \nabla\delta f + \frac{q_i}{m_i}(\mathbf{E} + \mathbf{v} \times \mathbf{B}) \cdot \nabla_\mathbf{v}\delta f = -\frac{\mathbf{E} \times \hat{\mathbf{b}}}{B} \cdot \nabla\chi \frac{\partial f_0}{\partial R_\chi} - q_i \mathbf{v} \cdot \mathbf{E} \frac{\partial f_0}{\partial K}.$$

We use this formulation as the starting point to model the ITG instability in a toroidal magnetic field in Chapter 5.

3.5 Summary and Conclusions

In this chapter, we have presented fully kinetic and gyrokinetic ion models for the ITG driven instability. First assuming a uniform magnetic field, we were able to derive dispersion relations for both models. By applying the gyrokinetic ordering assumptions to the FK ion dispersion relation, it was shown to reduce to the GK ion dispersion relation. The low frequency normal modes in the GK ion model are therefore contained in the FK ion model. These models may be useful for comparison studies to understand the limits of gyrokinetics. In addition to the low frequency modes, the FK ion model allows for the propagation of ion Bernstein modes at frequencies near the harmonics of the ion gyro-frequency. These are modes which have been analytically eliminated from the GK model, and can be a potential source of difficulty in numerical simulations of the FK model. Simulation results were obtained for the FK slab ITG mode, showing excellent agreement with the analytical dispersion theory. Finally, we present a method for extending the FK ion model for a weakly inhomogeneous magnetic field. This model will be of importance in Chapter 5, where the ITG instability is considered in a toroidal magnetic field.

Chapter 4

An Implicit δf Particle-in-Cell Method with Sub-Cycling and Orbit Averaging

A key advantage to gyrokinetic (GK) ion models is that the analytical elimination of the ion gyration time-scale can relax time step size constraints in numerical implementations. For many topical problems using GK ion models, however, resolution of the physical phenomena requires time step sizes which are close to that needed to fully resolve the ion gyro-motion. For example, in [47,48] a time step size of $\Omega_i \Delta t = 1.0$ is used for a well-resolved simulation of the DIII-D H-mode pedestal, where Ω_i is the ion cyclotron frequency. In [49] a time step size of $\Omega_i \Delta t = 0.2$ is used for the simulation of NSTX core plasmas, and in [50] $\Omega_i \Delta t = 0.25$ is used for microtearing simulations.

Given this progression in GK ion simulations, the use of models which fully resolve the ion gyro-motion, known as fully kinetic (FK) ion models, may provide a useful alternative to GK ion models without a large increase in computational effort. The advantage of the FK ion model is that the model accuracy does not depend on the ordering assumptions of gyrokinetics. Furthermore, recent efforts in optimizing particle-in-cell (PIC) algorithms for modern computing architectures, such as graphics processing units (GPUs), holds promise for handling the more expensive particle integration of the FK ion model [18–21].

In this chapter, we explore an implicit orbit averaging/sub-cycling (OASC) time stepping algorithm, which may be useful for extending the ability of FK ion models to simulate time scales which are long compared to the ion gyration time scale. This algorithm is shown to accurately produce finite-Larmor-radius (FLR) effects at perpendicular wave numbers $k_\perp \rho_i \sim O(1)$ while advancing the fields on a macro time step ΔT larger than that required to resolve the ion gyro-

motion. The accuracy of the ion gyro-motion is preserved by sub-cycling the computational particles on a micro time step Δt chosen such that $\Omega_i \Delta t \ll 1$. The algorithm is applied to a model problem for ion Landau damped ion acoustic waves in a magnetized plasma, which is the FK ion model presented in Chapter 3 with $\kappa_T = \kappa_{\mathcal{N}} = 0$. Linear theory for the model is derived to validate simulation results. Comparisons are also made with a linear dispersion relation obtained from the analysis of the equivalent GK ion model from Chapter 3. The dispersion results show very good agreement between the two models for the low frequency ion acoustic wave.

A notable effect in simulations using FK ions is the introduction of ion Bernstein waves near harmonics of the ion gyro-frequency [44, 51]. These are electrostatic normal modes, which are analytically eliminated in GK models, but are present when full ion dynamics are included. Linear theory based on the Laplace transform method is presented to determine the amplitudes of the normal modes relative to the initial perturbation size. The theory predicts ion Bernstein wave amplitudes which are comparable to the ion acoustic wave amplitude. Since the ion Bernstein waves are not damped, their presence in simulations may be undesirable for studies of low-frequency fluctuations. It is demonstrated that formulating the electrostatic field equation in terms of the ion particle flux results in numerical damping for the ion Bernstein waves.

This chapter is organized as follows. In Section 4.1, the model problem for ion Landau damped ion acoustic waves in a magnetized plasma is presented. Section 4.2 gives the linear theory for the model problem, including an analysis to derive information on the amplitudes of the normal modes. Section 4.3 gives the numerical methods used in our simulation model. In Section 4.4, simulation results are presented to demonstrate the numerical properties of the implicit OASC algorithm and the accurate production of FLR effects at large macro time step sizes. Here, a comparison with the GK model is also presented. A hybrid CPU-GPU implementation of our simulation model is discussed in Section 4.5 and is shown to achieve a speedup factor of ~ 48 compared to an equivalent serial CPU implementation. Section 4.6 contains further discussion and a summary.

4.1 Kinetic Model for Magnetized Ion Acoustic Waves

Here we introduce the equations for the ion Landau damped ion acoustic wave model. We consider a uniform equilibrium distribution $\nabla f_0 = 0$ in a straight, uniform magnetic field $\mathbf{B} = B_0\hat{z}$ and a self generated electrostatic field $\mathbf{E} = -\nabla\phi$, where ϕ is the electrostatic potential. The model is 2D-3V, meaning it is defined over two spatial dimensions and three velocity dimensions. The spatial dependence of quantities is over the two dimensional domain $(y, z) \in [0, l_y) \times [0, l_z)$ and periodicity is assumed in both y and z outside the domain with periods l_y and l_z respectively. The velocity dependence of quantities is over $(v_x, v_y, v_z) \in \mathbb{R}^3$. The ion distribution function f_i is taken to follow the Vlasov equation:

$$\frac{\partial f_i}{\partial t} + \mathbf{v} \cdot \nabla f_i + \frac{q_i}{m_i} (\mathbf{E} + \mathbf{v} \times \mathbf{B}) \cdot \nabla_{\mathbf{v}} f_i = 0, \tag{4.1}$$

where q_i and m_i are the ion charge and mass respectively. The electrons are assumed to be adiabatic, with number density n_e following:

$$n_e = n_0 \left(1 + \frac{e\phi}{T_e}\right), \tag{4.2}$$

where n_0 is the equilibrium density, e is the electron charge, and T_e is the electron temperature. Finally, quasi-neutrality is assumed:

$$n \equiv n_e = n_i = \int_{\mathbb{R}^3} f_i d^3v. \tag{4.3}$$

Equations (4.1)–(4.3), along with the periodicity assumptions form a closed model. In particular, Eq.(4.1) can be solved for the ion distribution function f_i, Eq.(4.3) then used to provide an electron number density n_e, and finally Eq.(4.2) provides a way to calculate ϕ. A Maxwellian equilibrium distribution is taken, in which case the normal modes of the model are a low frequency, magnetized ion acoustic waves and high frequency ion Bernstein waves.

4.2 Linear Analysis of the Model Problem

The linearized Vlasov equation is

$$\frac{\partial \delta f}{\partial t} + \mathbf{v} \cdot \nabla \delta f + \frac{q_i}{m_i} (\mathbf{v} \times \mathbf{B}) \cdot \nabla_{\mathbf{v}} \delta f = -\frac{q_i}{m_i} \mathbf{E} \cdot \nabla_{\mathbf{v}} f_0, \tag{4.4}$$

where the full ion distribution function is given as $f_i = f_0 + \delta f$. We consider a Maxwellian equilibrium distribution function

$$f_0(\mathbf{v}) = \frac{n_0}{(2\pi T_i/m_i)^{3/2}} \exp\left(-\frac{m_i \mathbf{v}\cdot\mathbf{v}}{2T_i}\right),$$

where T_i is the ion temperature. The field model couples to Eq.(4.4) through the perturbed number density δn. We have

$$\frac{e\phi}{T_e} = \frac{\delta n}{n_0} = \frac{1}{n_0}\int_{\mathbb{R}^3} \delta f d^3v. \tag{4.5}$$

4.2.1 Model Parameters

An analysis of the model equations shows that there are three dimensionless parameters which determine the behavior of the system. These are the parallel and perpendicular system lengths normalized by the thermal ion gyro-radius

$$\frac{l_z}{\rho_i}, \qquad \frac{l_y}{\rho_i},$$

and a ratio involving charges and temperatures

$$\theta \equiv \frac{q_i T_e}{e T_i}.$$

We define the thermal ion gyro-radius by $\rho_i = v_{th}/\Omega_i$, where v_{th} is the ion thermal velocity defined by $v_{th}^2 = T_i/m_i$. For the linear analysis, we are interested in the propagation of plane waves through the plasma, assuming spatial and time dependent quantities vary as:

$$\psi(\mathbf{x}, t) = \tilde{\psi}(\mathbf{k}, \omega) e^{i(\mathbf{k}\cdot\mathbf{x} - \omega t)}$$

where $\mathbf{k} = k_\parallel \hat{z} + k_\perp \hat{y}$ is the wave number and ω is the frequency, which may be complex valued. In this case, it is convenient to use the parameters $k_\parallel \rho_i$ and $k_\perp \rho_i$ in place of the first two. We consider cases where $k_\parallel \rho_i \ll 1$ and $k_\perp \rho_i \sim O(1)$ in order to work in a regime where the validity of GK ion models should overlap with the FK ion model. A rough estimate for the time scale separation is also

determined by these parameters. Defining the ion sound speed by $c_s^2 \equiv q_i T_e/em_i$, the time scale for an ion acoustic wave propagating nearly parallel to $\mathbf{B}$ is then roughly $c_s k_\parallel$. The ion gyro-motion and ion Bernstein waves evolve on the time scale of Ω_i. In terms of our parameters, we have

$$\sqrt{\theta} k_\parallel \rho_i = \frac{c_s k_\parallel}{\Omega_i} \ll 1.$$

4.2.2 Linear Theory

The normal modes for the system are studied for the linearized model. The resulting dispersion relation is given by

$$\epsilon(\mathbf{k},\omega) = 1 - \frac{\theta}{2} \sum_{n=-\infty}^{\infty} Z' \left(\frac{\omega/\Omega_i + n}{\sqrt{2} k_\parallel \rho_i} \right) I_n(k_\perp^2 \rho_i^2) e^{-k_\perp^2 \rho_i^2} - \frac{\theta}{\sqrt{2} k_\parallel \rho_i} \sum_{n=-\infty}^{\infty} n Z \left(\frac{\omega/\Omega_i + n}{\sqrt{2} k_\parallel \rho_i} \right) I_n(k_\perp^2 \rho_i^2) e^{-k_\perp^2 \rho_i^2} = 0, \tag{4.6}$$

where Z is the plasma dispersion function of Fried and Conte [46] and I_n is the n^{th} modified Bessel function of the first kind. The solutions of Eq.(4.6) give the normal modes of the model, which include a low-frequency, ion Landau damped ion acoustic wave and undamped ion Bernstein waves near harmonics of the ion gyro-frequency. The ion Bernstein waves are a unique feature of the FK ion model and are not present in GK ion models. In our numerical simulations with finite $k_\perp \rho_i$, it was found that the Bernstein waves had amplitudes comparable to the ion acoustic wave. Since the Bernstein waves are undamped, they were found to quickly become dominant in the time histories of ϕ. To validate that this feature of our simulations was consistent with the continuous model, we have further developed the linear theory using the Laplace transform in time.

The linear system is studied as an initial value problem using the Laplace transform to determine the amplitudes of each normal mode. The Laplace transform method applied to the one dimensional Landau problem as an initial value problem is presented in a number of plasma physics texts. See for example, Chapter 8 of [2]. The initial condition for the perturbed distribution function is taken to be

$$\delta f(\mathbf{x}, \mathbf{v}, t = 0) = A_0 f_0(\mathbf{v}) e^{i\mathbf{k}\cdot\mathbf{x}}. \tag{4.7}$$

The Laplace transform pair for a time dependent quantity $\varphi(t)$ is

$$\varphi(p) = \int_0^\infty \varphi(t) e^{-pt} dt, \qquad \varphi(t) = \frac{1}{2\pi i} \int_{\sigma - i\infty}^{\sigma + i\infty} \varphi(p) e^{pt} dp \tag{4.8}$$

where p is complex valued and σ can be chosen as any real number which is to the right of all singularities of $\varphi(p)$ in the complex p-plane. The complex variable p is related to the complex frequency of a plane wave ω simply by $p = -i\omega$. Equations (4.4)–(4.5) with an initial condition given by Eq.(4.7) can be solved for the transformed electrostatic potential. The solution of the Laplace (in time) and Fourier (in space) transformed electrostatic potential in terms of the complex frequency is

$$\frac{e\phi_{\mathbf{k}}}{T_e}(p) = \frac{A_0}{i\sqrt{2}k_\parallel \rho_i} \frac{\sum_{n=-\infty}^{\infty} Z\left(\frac{ip/\Omega_i + n}{\sqrt{2}k_\parallel \rho_i}\right) I_n(k_\perp^2 \rho_i^2) e^{-k_\perp^2 \rho_i^2}}{\epsilon(\mathbf{k}, ip)}. \tag{4.9}$$

The time dependent solution of the electrostatic potential can be obtained from the inverse Laplace transform of Eq.(4.9), which is given by the contour integral in Eq.(4.8). The evaluation of this contour integral is simplified by deforming the contour of integration to the path shown in Figure 4.1 with a possible set of poles of $\phi_{\mathbf{k}}(p)$, corresponding to the zeros of $\epsilon(\mathbf{k}, ip)$. Justification for the contour deformation is given in Appendix A. By examining the deformed contour in Figure 4.1 b), the time dependent solution of the electrostatic potential can be written as

$$\begin{aligned} \frac{e\phi_{\mathbf{k}}}{T_e}(t) = \sum_j A_j e^{p_j t} + \frac{1}{2\pi i} \Bigg(& \int_{\sigma - i\infty}^{-\alpha - i\infty} \frac{e\phi_{\mathbf{k}}}{T_e}(p) e^{pt} dp + \\ & \int_{-\alpha - i\infty}^{-\alpha + i\infty} \frac{e\phi_{\mathbf{k}}}{T_e}(p) e^{pt} dp + \int_{-\alpha + i\infty}^{\sigma + i\infty} \frac{e\phi_{\mathbf{k}}}{T_e}(p) e^{pt} dp \Bigg), \end{aligned} \tag{4.10}$$

where $\{p_j\}$ in the first term are the simple roots of $\epsilon(\mathbf{k}, ip)$, and

$$A_j = \mathrm{Res}\left[\frac{e\phi_{\mathbf{k}}}{T_e}(p), p_j\right]. \tag{4.11}$$

The main contribution in Eq.(4.10) comes from the first term. Provided that $\phi_{\mathbf{k}}(p)$ decays rapidly as $\mathrm{Im}(p) \to \pm\infty$, the second and fourth terms in Eq.(4.10) will vanish. Furthermore, the third term becomes exponentially small compared to the contributions from the poles as $t \to \infty$, leaving the normal modes given by the first term as the time asymptotic solution. In Section 4.4, we

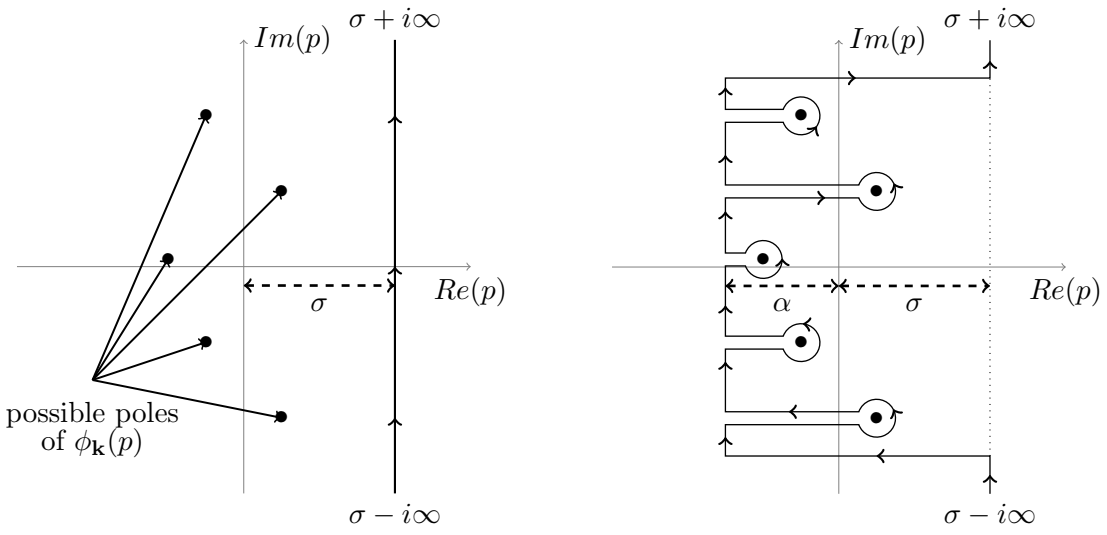

Figure 4.1: Contour deformation for obtaining Eq.(4.10). The figure on the left (a) illustrates the original contour used in the inverse Laplace transform. The figure on the right (b) illustrates the deformed contour.

numerically solve for the amplitudes of the normal modes relative to the initial perturbation size A_0 and compare with the amplitudes found in our simulations. This is accomplished by first solving the dispersion relation Eq.(4.6) numerically for the complex frequencies and then evaluating the corresponding residues in Eq.(4.11) to obtain the amplitudes A_j.

4.3 Numerical Methods

A number of numerical methods are used to obtain stable, accurate, and low noise simulations of the low frequency ion acoustic wave at large time step sizes. Key features of our 2D-3V simulation model include the δf method which reduces discrete particle noise levels by solving for small perturbations from a Maxwellian equilibrium, a perturbed flux density formulation of the field model which introduces numerical damping of high frequency modes, orbit averaging and sub-cycling (OASC) using separate time step sizes for the particles and fields, a second order implicit integrating scheme to advance the particle orbits and weight equations, and a Picard iterative process to solve the implicit equations.

4.3.1 δf method

The δf method is utilized, which is effective in reducing discrete particle noise by solving for departures from an known equilibrium distribution [38–42]. The assumption is made that f_i can be separated into a known, time independent equilibrium part and an unknown perturbed part as $f_i = f_0 + \delta f$. Particle weights are defined for each computational particle as $w_p = \delta f_p / f_p \approx \delta f_p / f_{0p}$, where the subscript p indicates an evaluation at the phase space location of particle p. The particle weights evolve according to the weight equation, which for linear simulations is

$$\frac{dw_p}{dt} = -\frac{q_i}{m_i}\mathbf{E}(\mathbf{x}_p) \cdot \nabla_{\mathbf{v}_p} \ln f_0(\mathbf{v}_p).$$

For the linear δf scheme, the particles' phase space locations evolve according to their equilibrium trajectories:

$$\begin{aligned}\frac{d\mathbf{x}_p}{dt} &= \mathbf{v}_p \\ \frac{d\mathbf{v}_p}{dt} &= \frac{q_i}{m_i}\left(\mathbf{v}_p \times \mathbf{B}\right).\end{aligned}$$

Once the particle weights and phase space locations are known, the perturbed number and flux densities at grid point $\mathbf{X}_j$ can be calculated as follows:

$$\begin{aligned}\delta n_j &= \frac{N_y N_z n_0}{N_c}\sum_{p=1}^{N_c} w_p S_{\mathbf{x}}(\mathbf{X}_j - \mathbf{x}_p) \\ \delta(n\mathbf{u})_j &= \frac{N_y N_z n_0}{N_c}\sum_{p=1}^{N_c} w_p \mathbf{v}_p S_{\mathbf{x}}(\mathbf{X}_j - \mathbf{x}_p)\end{aligned}$$

where N_y and N_z are the number of grid points in the y and z directions, respectively, N_c is the number of computational particles, and $S_{\mathbf{x}}$ is the "shape" function [32], which we take to be a product of linear b-spline functions.

4.3.2 Field Equation Formulations

Recent numerical analysis of implicit δf models has shown that numerical damping can depend on the velocity moments used in the field model equations [23]. Here, we consider two

formulations of Eq.(4.5) to be used in the simulation model. These formulations are equivalent in the continuous limit $\Delta y \to 0$, $\Delta z \to 0$, and $\Delta t \to 0$ but exhibit different properties in the discrete models. The first formulation uses the perturbed number density directly, and the second formulation uses the continuity equation to give the field model in terms of the perturbed flux density. We will refer to these formulations as the perturbed number density form (PND) and the perturbed flux density form (PFD). Simulation results presented in Section 4.4 show that the PFD form introduces numerical damping of the ion Bernstein waves, where as, the PND form leaves the ion Bernstein waves undamped. For the PND form, we have simply

$$\frac{e\phi_j^\nu}{T_e} = \frac{\delta n_j^\nu}{n_0},$$

where ν is the time step index. To derive the PFD form, the partial derivative with respect to time is taken in Eq.(4.5) and the continuity equation is used to give

$$\frac{\partial}{\partial t}\left(\frac{e\phi_j}{T_e}\right) = -\nabla \cdot \frac{\delta(n\mathbf{u})_j}{n_0} \tag{4.12}$$

Our baseline time stepping method for the PFD form, without OASC, uses the trapezoidal rule to discretize Eq.(4.12) in time as

$$\frac{e\phi_j^\nu}{T_e} = \frac{e\phi_j^{\nu-1}}{T_e} - \frac{\Delta t}{2}\left(\nabla \cdot \frac{\delta(n\mathbf{u})_j^\nu + \delta(n\mathbf{u})_j^{\nu-1}}{n_0}\right)$$

where the divergence is taken spectrally in Fourier space. The electric field for both field models is also computed by taking the gradient of ϕ^ν spectrally from the discrete Fourier transform. Simulation results using these two field equation formulations are presented in Section 4.4.

4.3.3 Baseline Time Stepping Algorithm

Our baseline time stepping algorithm to which we apply OASC uses a second order implicit scheme to advance the particle positions, velocities, and weight equations. Our motivation for using implicit schemes is for the greater stability that is generally offered. In the process of designing our numerical schemes, we keep in mind future applications using more complex models that may involve higher frequency modes posing severe constraints on the time step size for explicit schemes.

For example, in [16], it is known that the compressional Alfven wave can be the source of a numerical instability when it is not well resolved. This can be restrictive since $\omega/\Omega_i \gg 1$ in low-β plasmas. The following implicit time discretization scheme is applied to the ion equations of motion and weight equation to address these difficulties

$$\mathbf{x}^{\nu} = \mathbf{x}^{\nu-1} + \frac{\Delta t}{2}\left(\mathbf{v}^{\nu} + \mathbf{v}^{\nu-1}\right) \tag{4.13}$$

$$\mathbf{v}^{\nu} = \mathbf{R}\cdot\mathbf{v}^{\nu-1} \tag{4.14}$$

$$w^{\nu} = w^{\nu-1} - \frac{\Delta t}{2}\left[G^{\nu}(\mathbf{x}^{\nu},\mathbf{v}^{\nu}) + G^{\nu-1}(\mathbf{x}^{\nu-1},\mathbf{v}^{\nu-1})\right], \tag{4.15}$$

where ν is the discrete time index, and we have dropped the subscript p for simplicity of notation. In Eq.(4.14), the rotation matrix $\mathbf{R}$ is defined as

$$\mathbf{R} = \begin{bmatrix} \cos(\Omega_i\Delta t) & \sin(\Omega_i\Delta t) & 0 \\ -\sin(\Omega_i\Delta t) & \cos(\Omega_i\Delta t) & 0 \\ 0 & 0 & 1 \end{bmatrix},$$

which produces the correct gyro-phase at each time step, and in Eq.(4.15) we have

$$G^{\nu}(\mathbf{x}^{\nu},\mathbf{v}^{\nu}) = \frac{q}{m}\mathbf{E}^{\nu}(\mathbf{x}^{\nu})\cdot\nabla_{\mathbf{v}^{\nu}}\ln f_0(\mathbf{v}^{\nu}), \tag{4.16}$$

where the evaluation of the electric field at a particle's position is performed through interpolation as

$$\mathbf{E}^{\nu}(\mathbf{x}^{\nu}) = \sum_j \mathbf{E}^{\nu}_j S_{\mathbf{x}}(\mathbf{X}_j - \mathbf{x}^{\nu}).$$

The velocity advance may be extended for nonlinear simulations by including half accelerations due to $\mathbf{E}^{\nu-1}(\mathbf{x}^{\nu-1})$ and $\mathbf{E}^{\nu}(\mathbf{x}^{\nu})$ before and after the rotation, respectively, similar to the Boris push [32, 52]. Modification to the weight equation is also needed for nonlinear simulations as in [38].

4.3.4 Orbit Averaging and Sub-Cycling

For the OASC scheme, the electric field and the computational particles are advanced on separate time steps [53]. The long term goal of this research is to model low frequency ($\omega \ll$

Ω_i) well magnetized plasma physics where gyrokinetics is applicable using a direct Lorentz force method. The main issue at hand is to accurately model the ion FLR effects without including the ion Bernstein waves which are a source of high frequency noise. Because we are interested in low frequency phenomena, we will sub-cycle to resolve the ion cyclotron motion, then orbit-average numerically to accurately resolve ion FLR effects. Orbit averaging and sub-cycling have been explored previously in the context of multi-scale implicit PIC. Besides the seminal orbit-averaging work of B. Cohen and co-workers [53–55], a multi-scale method was developed to advance particles depending on their local accuracy in phase space [56, 57]. More recently an exact charge and energy-conserving scheme incorporates a sub-stepping in time algorithm to avoid particles tunnelling through an electrostatic potential barrier and improves momentum conservation [20, 58, 59]. In our algorithm, the micro time step Δt is used to resolve the fast gyro-motion of the ions and the macro time step ΔT is used to resolve the low-frequency fields. These are chosen such that $\Omega_i \Delta t \ll 1$, $\Omega_i \Delta T \gg 1$, and $\Delta T/\Delta t = M$ for $M \in \mathbb{N}$. The particle trajectories and weights are sub-cycled on the micro time step according to Eqs.(4.13)–(4.16) where $\mathbf{E}^\nu$ is replaced with $\mathbf{E}^{(N,\nu)}$ for $1 \leq \nu \leq M-1$. We define $\mathbf{E}^{(N,\nu)}$ as the electric field interpolated in time to the micro time step $t^{(N,\nu)}$ from the fields defined at the macro time steps t^{N-1} and t^N. A simple linear interpolation is used

$$\mathbf{E}^{(N,\nu)} = (1 - \frac{\nu}{M})\mathbf{E}^{N-1} + \frac{\nu}{M}\mathbf{E}^N.$$

The orbit averaging scheme is derived for the flux form of the field equation Eq.(4.12). Integrating Eq.(4.12) between macro time steps t^{N-1} and t^N, we have

$$\frac{e\phi^N}{T_e} = \frac{e\phi^{N-1}}{T_e} - \nabla \cdot \int_{t^{N-1}}^{t^N} \frac{\delta(n\mathbf{u})}{n_0} dt.$$

The integral on the right hand side is then approximated using the composite trapezoidal rule

$$\int_{t^{N-1}}^{t^N} \delta(n\mathbf{u}) dt \approx \frac{\Delta T}{2M} \left(\delta(n\mathbf{u})^{N-1} + 2\delta(n\mathbf{u})^{(N,1)} + 2\delta(n\mathbf{u})^{(N,2)} + ... + 2\delta(n\mathbf{u})^{(N,M-1)} + \delta(n\mathbf{u})^N \right), \tag{4.17}$$

where the perturbed flux densities $\delta(n\mathbf{u})^{(N,\nu)}$ are deposited using particle trajectories and weights on the micro time step $t^{(N,\nu)}$. We will refer to the right hand side of Eq.(4.17) as the orbit averaged

flux density and denote it as $\langle \delta(n\mathbf{u}) \rangle^{N-1/2}$. In this notation, our discretized field model is

$$\frac{e\phi^N}{T_e} = \frac{e\phi^{N-1}}{T_e} - \nabla \cdot \langle \delta(n\mathbf{u}) \rangle^{N-1/2}. \tag{4.18}$$

The OASC algorithm is illustrated in Figure 4.2. Note that the OASC algorithm reduces to the baseline time stepping algorithm with the PFD form of the field equation when $M = 1$.

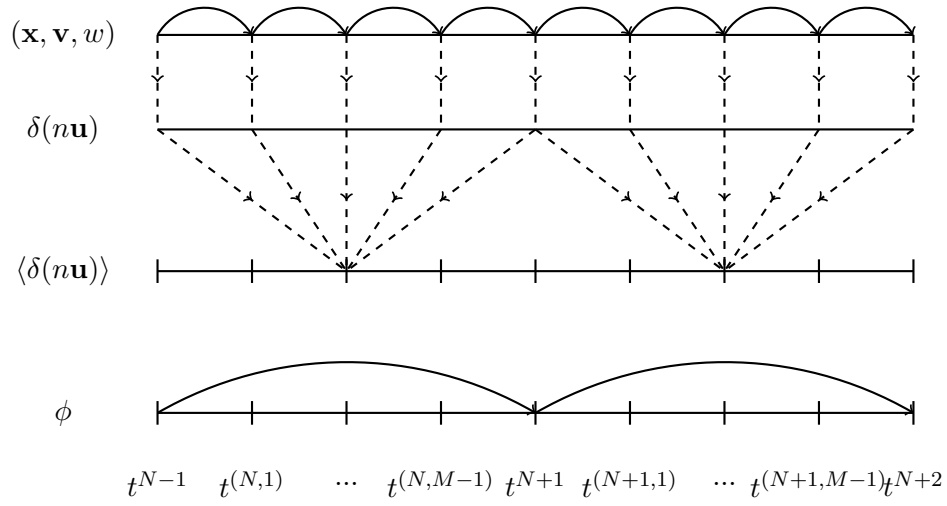

Figure 4.2: Illustration of the OASC algorithm. Particle quantities $(\mathbf{x}, \mathbf{v}, w)$ are advanced on the micro time steps using a time interpolated electric field. The flux density $\delta(n\mathbf{u})$ is deposited from the particles at each micro time step to obtain the orbit averaged flux density $\langle \delta(n\mathbf{u}) \rangle$, which is used to advance ϕ over the macro time step.

4.3.5 Solution Method for the Implicit Equations

The OASC scheme is implicit and therefore requires the self consistent solution of the particles and electric field at the macro time step t^N. There has been recent progress made in efficient solution methods for fully implicit PIC. These efforts have focused on the use of Jacobian-free Newton-Krylov (JFNK) solvers [58,60,61] and preconditioning to accelerate the convergence of the GMRES iterations [62]. The use of a JFNK solver has not been explored in this work but may hold future promise for increased computational efficiency of the algorithm. For our simulation model, we adopt a Picard iteration scheme to solve the implicit equations. An initial guess is made for ϕ^N and successive corrections to ϕ^N are made by repeatedly advancing the sub-cycled particle

system. This process is carried out until the L^2 norm of the residual in Eq.(4.18) is reduced to a specified tolerance. For our simulations, we have taken both the absolute and relative tolerances to be 5.0×10^{-7}. For the initial guess, we take the value of ϕ at the previous time step. In the tests performed in Section 4.4, the Picard scheme typically converged in 4-8 iterations, with the number of iterations increasing as expected with larger values of ΔT and $k_\perp \rho_i$.

4.4 Simulation Results

To demonstrate the numerical properties of the algorithms discussed in Section 4.3 applied to the FK ion model, linear simulations are performed and compared to the theory presented in Section 4.2. Of interest are the use of the PFD form to damp the high frequency ion Bernstein waves, the accurate production of FLR effects in the OASC algorithm, and the effects of the sub-cycling parameter M in producing accurate simulations over long time scales.

4.4.1 Effects of the Field Equation Formulation on Ion Bernstein Waves

A notable feature of the FK ion simulation model is the presence of ion Bernstein waves near harmonics of the ion gyro-frequency, which are superimposed on the ion acoustic wave. Although consistent with the physical model, these are undamped high frequency modes and their presence may be undesirable for studies of low frequency phenomena. In addition, ion Berstein waves are eliminated in GK ion models, which may cause difficulty for comparisons with FK ion models. In simulations using the PND form of the field model, ion Bernstein waves with large amplitudes were found to be present for finite $k_\perp \rho_i$ and to quickly obscure the low frequency ion acoustic wave as this parameter was increased.

In Figure 4.3, simulations are performed using the PND form of the field model. The amplitudes for the ion acoustic wave and the first three Bernstein waves are measured relative to the initial perturbation size A_0 for increasing values of $k_\perp \rho_i$ and compared to the theoretical amplitudes from Eq.(4.11). We use the model parameters $\theta = 5$ and $k_\parallel \rho_i = 6.28 \times 10^{-3}$. The simulations are performed using the baseline time stepping algorithm from Section 4.3.3 with 131072 computa-

tional particles, a mesh size of $n_y \times n_z = 16 \times 32$, and a time step size $\Omega_i \Delta t = 0.125$. Both theory and simulations, using the PND form of the field model, show Bernstein waves with amplitudes comparable to or exceeding that of the ion acoustic wave for finite $k_\perp \rho_i$. In Figure 4.4, we compare

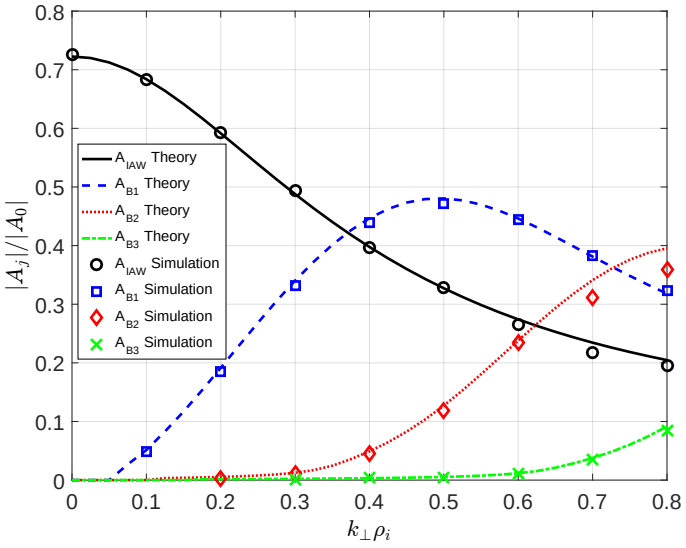

Figure 4.3: Amplitudes from simulations using the PND form of the field model are compared to theory for the ion acoustic wave, A_{IAW}, and the first three Bernstein waves, (A_{B1}, A_{B2}, A_{B3}). The amplitudes are given relative to the initial perturbation size, A_0.

simulations at $k_\perp \rho_i = 0.3$ between the PND and PFD forms of the field model. The physical and numerical parameters are taken the same as in Figure 4.3. The time history of the first Fourier mode is plotted, demonstrating the numerical damping of the ion Bernstein waves which is achieved only for the PFD form. The difference in the numerical behaviors of the two field model formulations is consistent with the numerical analysis in [23]. In this chapter, it is shown that numerical dissipation which is normally present when using implicit schemes can be absent in the δf method when the field model used contains only the perturbed number density as a source term.

4.4.2 FLR Effects for the Orbit Averaging/Sub-Cycling Algorithm

An important measure of success for the OASC algorithm is the ability to accurately model FLR effects at large time step sizes. This is demonstrated for the ion acoustic wave using the

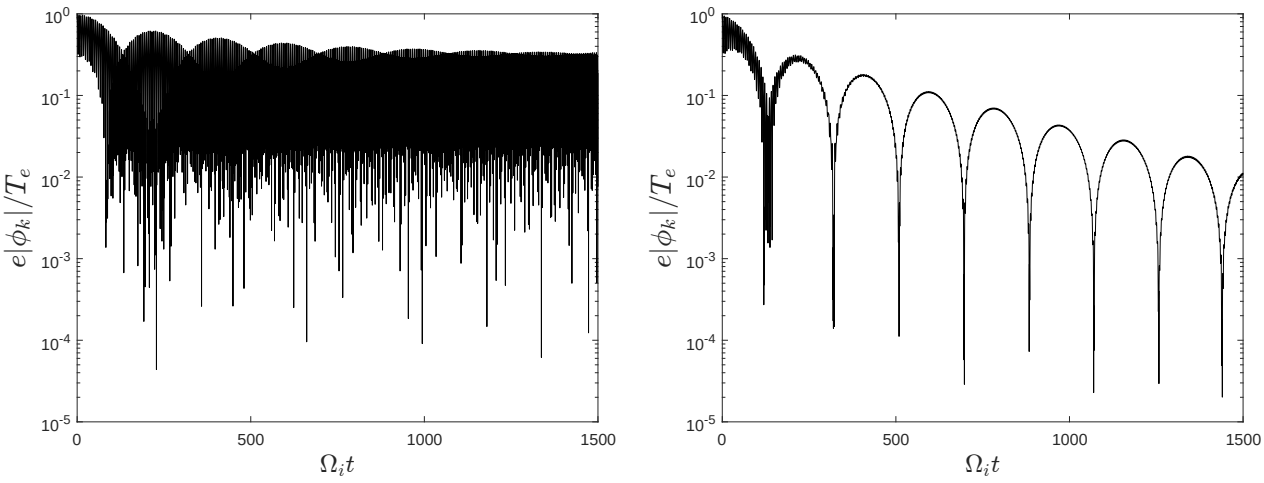

Figure 4.4: Time histories of the first Fourier mode amplitude of $\phi_{\mathbf{k}}$. The PND form is used on the left and the PFD form is used on the right. Numerical damping of the ion Bernstein waves occurs only for the PFD form of the field model, leaving a clean simulation of the low frequency ion acoustic wave.

model parameters $\theta = 5$, $k_{\|}\rho_i = 1.61 \times 10^{-3}$ and scanning over values of $k_{\perp}\rho_i \sim O(1)$. For these simulations, we use 262144 computational particles, a mesh size of $n_y \times n_z = 64 \times 64$, a macro time step size of $\Omega_i \Delta T = 0.75$, and sub-cycling parameter $M = 18$, which corresponds to a micro time step size of $\Omega_i \Delta t = 4.17 \times 10^{-2}$. In Figure 4.5, the dispersion results of the simulations are compared to the exact linear dispersion theory for the FK ion model given by Eq.(4.6). Comparisons are also made with the linear dispersion theory for the GK model, which was presented in Chapter 3. The simulations show excellent agreement with the FK ion dispersion theory using a macro time step size larger than that required to resolve the gyro-motion of the ions. Furthermore, the dispersion relation for the GK ion model yields nearly identical results to that of the FK ion model for the ion acoustic wave.

4.4.3 Effects of the Sub-Cycling Parameter

In order to produce accurate simulations over long time scales, sufficient resolution of the ion gyr-omotion on the micro time step is necessary. Convergence tests are performed, varying the

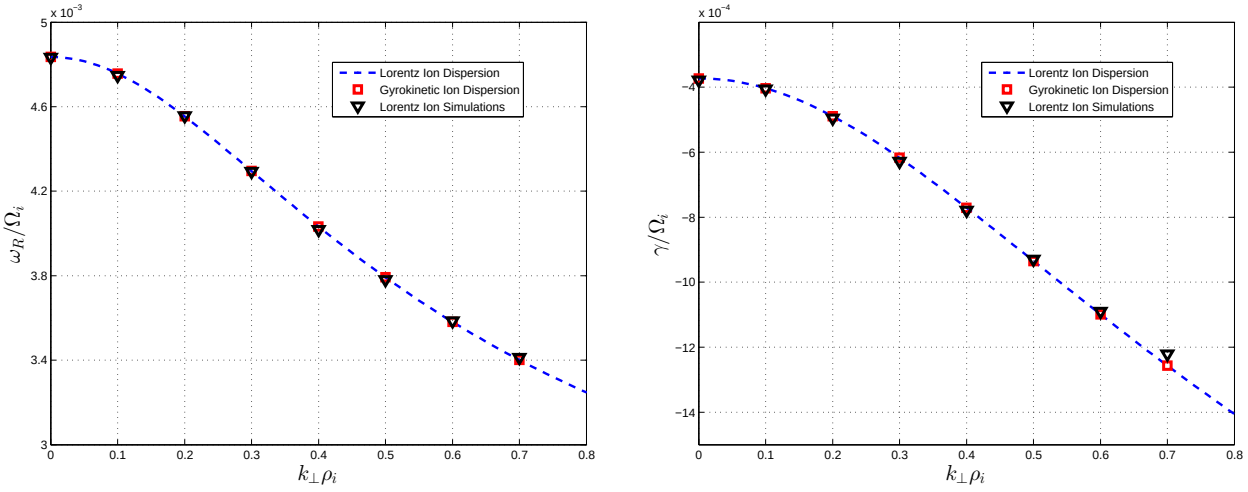

Figure 4.5: Dispersion results showing FLR effects on the ion acoustic wave using the parameters $\theta = 5.0$, $k_\parallel \rho_i = 1.61 \times 10^{-3}, \Omega_i \Delta T = 0.75$, and $M = 18$ in the OASC algorithm. Data points obtained by solving the GK dispersion relation given in Chapter 3 are also shown.

sub-cycling parameter, M. In the first test, the macro time step is kept fixed at $\Omega_i \Delta T = 1.0$ and the sub-cycling parameter, M, is increased from $M = 1$, which corresponds to the baseline time stepping algorithm (without OASC) over the macro time step, up to $M = 16$ which well resolves the ion gyro-motion. The time histories of the first Fourier mode amplitude of ϕ for increasing values of M in the first test are given in Figure 4.6 a). As expected, the quality of the simulations improves as the sub-cycling parameter is increased. When M is taken too small, large inaccuracies in the simulations develop quickly in time. In the second test, the micro time step size is kept fixed at $\Omega_i \Delta t = 6.25 \times 10^{-2}$ and M is increased to give larger values for the macro time step. The time histories of the first Fourier mode amplitude of ϕ for increasing values of M in the second test are given in Figure 4.6 b). It is observed that the time histories are nearly identical in each case, demonstrating the robustness of the algorithm for large macro time steps, provided there is sufficient resolution at the micro time step. For both tests, the same model parameters, particle number, and mesh size are used as in Figure 4.5 and $k_\perp \rho_i = 0.4$.

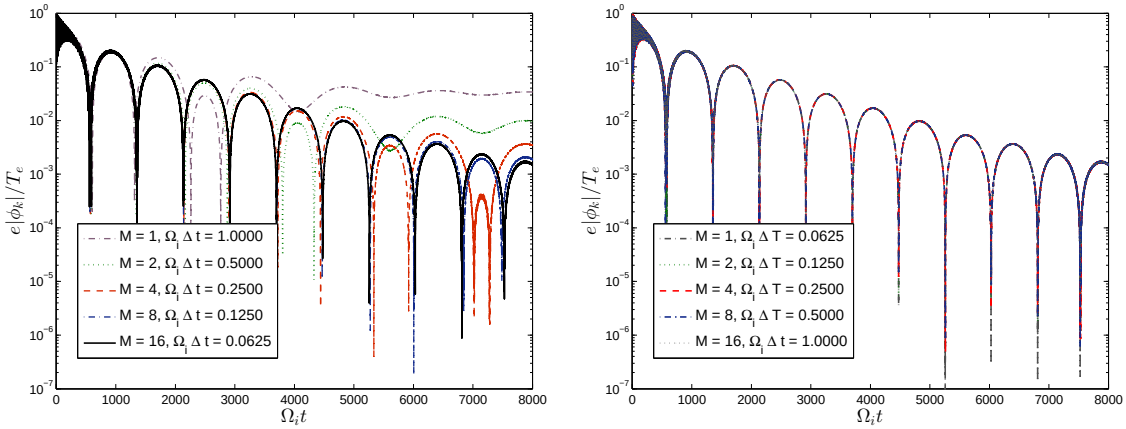

Figure 4.6: Time histories of the first Fourier mode amplitude of $\phi_{\mathbf{k}}$. On the left (a), the macro time step size is fixed at $\Omega_i \Delta T = 1.0$ and the sub-cycling parameter M is increased to improve accuracy for long time periods. On the right (b), the micro time step size is fixed at $\Omega_i \Delta t = 6.25 \times 10^{-2}$ and M is increased to give a larger macro time step size.

4.5 CPU-GPU Implementation

One promising aspect of the OASC algorithm presented here is that it is amenable to implementation on hybrid architecture utilizing graphics processing units (GPUs) or many integrated core co-processors. The reason for this is that the particle pushing over the micro time steps and the orbit averaging can be done locally on the GPU. The resulting velocity moments can be copied to the CPU memory where a global field solve is done. This eliminates the need for communication of particle data between the CPU and GPU. Many applications of GK simulation are for situation where $\Omega_i \Delta t \sim 1$. Additionally, the FK ion method presented here can take advantage of hybrid architectures, as we show below. Similarly [20] implemented their energy and charge conserving scheme with sub-stepping and saw speedups over a factor of 100 compared to an equivalent serial CPU implementation. To demonstrate the feasibility of utilizing hybrid architectures with sub-cycling and orbit averaging, we have implemented our test bed code on one node of the Titan supercomputer at Oak Ridge National Laboratory. We note this is simply a first step to show the promise of the algorithm. Many node parallelization using MPI is not implemented. Future implementations of the algorithm for solving more realistic turbulence problems will require many

nodes (> 100). We also note that MPI optimization is well understood and widely used in PIC codes.

Our CPU-GPU version of the OASC algorithm is implemented in single-precision using CUDA Fortran. Interpolation of field values, particle pushes, and deposits are all performed locally on the GPU, and the field solve is performed on the CPU. The particle data is deposited to arrays stored in global memory using the `atomicadd` function to avoid race conditions, which can occur when more than one thread simultaneously tries to access the same memory location [63]. Although the use of atomic functions can delay the parallel executions in the code, the reduced communication cost between the device and host which is gained by keeping the particle data on the GPU outweighs the serialization that results from the atomic additions. Optimizations to the deposits, including the use of particle sorting, storing multiple copies of the domain in shared memory, and partitioning the grid space into "tiles" have been explored in [20, 21]. As a first step in utilizing GPUs, we focus on simplicity of implementation; however, these optimizations are promising for future work to reduce the run-time of the deposit phase in our algorithm.

To benchmark the CPU-GPU implementation, we compare run-times between the single-precision CPU-GPU code and an equivalent single-precision serial CPU code running on the Titan supercomputer. Both codes are compiled with the PGI 15.3.0 compiler using the `-fast` optimization flag. The GPU used is an NVIDIA Tesla K20X, which utilizes the NVIDIA Kepler$^{\text{TM}}$ architecture and has a peak theoretical compute performance of 3.95 TFLOPs in single-precision. The host machine is a 16-core 2.2 GHz AMD Opteron$^{\text{TM}}$ 6274 processor, for which one core is utilized for both the CPU-GPU and CPU serial implementations.

In Figure 4.7, the time per particle per sub-cycle is reported in nano-seconds for the CPU-GPU and CPU serial codes as the number of particles is increased. The test problem uses parameters $\theta = 5.0$, $k_{\|}\rho_i = 1.61 \times 10^{-3}$ and $k_{\perp}\rho_i = 0.4$. The mesh size is $n_y \times n_z = 64 \times 64$, and the time step size is $\Omega_i \Delta t = 6.25 \times 10^{-2}$ for a sub-cycling parameter $M = 1$, which corresponds to the baseline time stepping algorithm. The largest speedup observed is a factor of 46.9 when 2^{22} particles are used. In Figure 4.8, we examine the effects of the sub-cycling parameter, M, on the

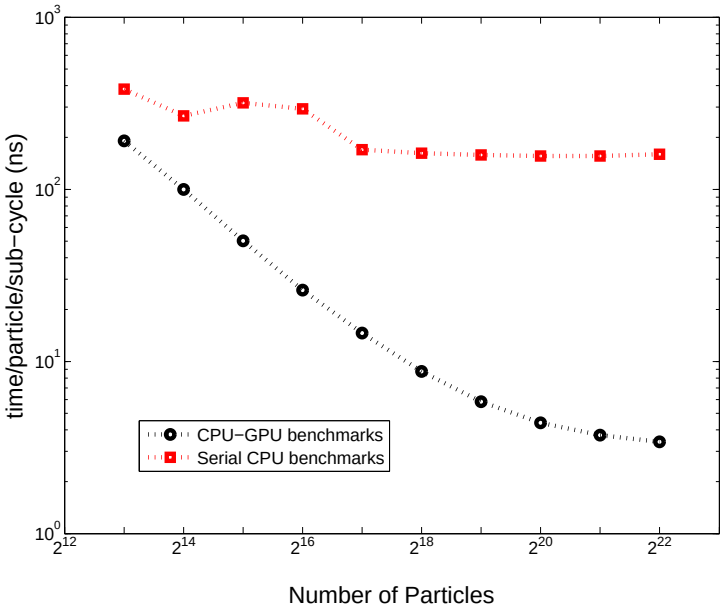

Figure 4.7: Benchmarks of the CPU-GPU and serial CPU implementations. The test problem uses sub-cycling parameter $M = 1$, which corresponds to the baseline time stepping algorithm. A speedup factor of 46.9 is observed for 2^{22} particles.

run-time of the two implementations. We run with a macro time step size of $\Omega_i \Delta T = 0.75$ for $2^{17} - 2^{19}$ particles, keeping all other parameters the same as for Figure 4.7. An additional speedup is observed in the CPU-GPU code as M is increased, due to the increased amount of computation that can be performed on the GPU per communication to the CPU. This speedup is more significant for lower numbers of particles, for example, when using 2^{17} particles, a speedup factor of 3.9 is observed in the CPU-GPU code for $M = 32$ compared to $M = 1$. The serial CPU code; however, is near peak performance for all tests shown in Figure 4.8. The largest speedup factor observed between the CPU-GPU and serial CPU codes when increasing M is 47.9 for 2^{19} particles at $M = 32$.

4.6 Summary and Conclusions

In this study, we have explored an implicit δf particle-in-cell method with orbit averaging and sub-cycling algorithm, which is applied to a magnetized plasma simulation model for ion acoustic

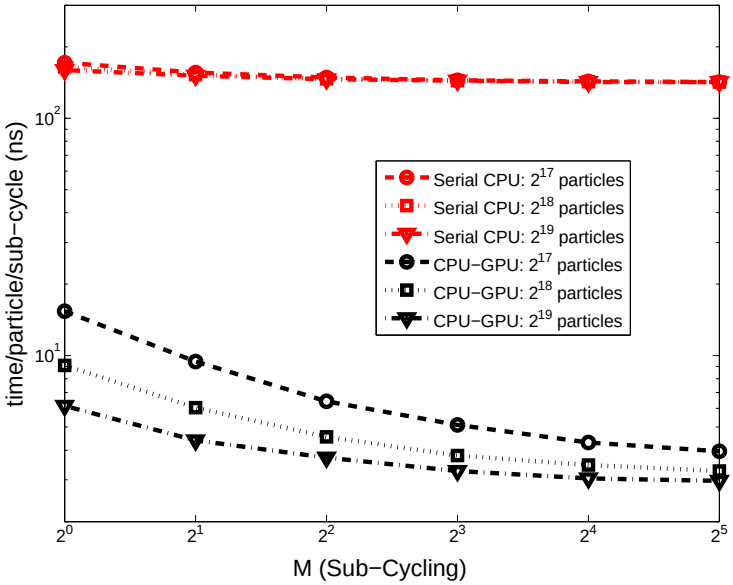

Figure 4.8: The sub-cycling parameter, M, is increased and an additional speedup is observed for the CPU-GPU code. The serial CPU code is near peak performance.

waves using the full Lorentz force equations of motion for the ions. This algorithm shows promise to extend efforts in the development of fully kinetic ion methods to model low frequency phenomena in well magnetized plasmas. In particular, we were able to produce accurate FLR effects over long time scales in our simulations using a fully kinetic ion model. Additionally, theory has been derived to study the significance of ion Bernstein waves in our model. Ion Bernstein waves are of interest, since they are unique to models using the full Lorentz force equations of motion and are analytically eliminated from gyrokinetic ion models. It is found that the ion Bernstein waves can have a significant effect on simulations, however, numerical damping can be introduced to the ion Bernstein waves when the field equation is formulated in terms of the perturbed flux density in the δf method. This can be beneficial for simulations of low-frequency fluctuations, since the ion Bernstein waves have significant amplitudes for finite $k_\perp \rho_i$, and can obscure physics on longer time scales. Finally, a CPU-GPU implementation of the OASC algorithm has been developed and has achieved a speedup by a factor of ~ 48 compared to an equivalent serial CPU only code. Low

communication between the CPU and GPU can be achieved by transferring only grid quantities, making the OASC algorithm well suited to implement on hybrid architectures. Our testbed model of the ion acoustic wave is of interest due to its relation to the ion temperature gradient models of Chapters 3 and 5.

Chapter 5

A Fully Kinetic Ion Model for the Toroidal Ion Temperature Gradient Instability

Theoretical investigations of the ion temperature gradient (ITG) mode began using simplified magnetic geometries in slab models [64, 65]. In slab geometry, the ITG mode is a deformation of the ion acoustic wave, driven unstable by $\mathbf{v}_E$ convections of "hot" particles into regions of positive pressure perturbations and "cold" particles into regions of negative pressure perturbations. In magnetically confined fusion experiments, however, tokamaks confine plasma in a toroidal magnetic field configuration with twisted, sheared field lines. Guiding center drifts due to the curvature and gradient of the magnetic field provide additional destabilizing mechanisms in the ITG mode, leading to larger growth rates than predicted in slab models [4, 5, 43].

The toroidal ITG instability is a well studied problem in the context of gyrokinetics [5,66–70], and therefore provides a good starting point in the development of fully kinetic (FK) ion models which can be used to verify gyrokinetic (GK) models. In this chapter, we present a simulation model for the toroidal ITG instability using the full Lorentz force equations of motion for the ions. We use the model presented in Chapter 3.4.2 to include temperature and density gradients in the equilibrium ion distribution function. In order to ensure the long time accuracy of the particle orbits in the FK ion model, an integration scheme based on variational principles has been developed. We focus on the "Cyclone DIII-D base case parameter set" as given in [70] as a benchmark for the FK toroidal ITG simulation model. Comparisons are made with the global GEM code for a frequency scan over the parameter R_0/L_T, where R_0 is the major radius and L_T is the length scale for the

equilibrium temperature gradient.

This chapter is organized as follows. In Section 5.1, we introduce the basic toroidal coordinate system and the field line following coordinate system, which is used to define the computational domain and boundary conditions. Section 5.2 give details of the model equations based on the equilibrium construction presented in Chapter 3.4.2. In Section 5.3, we present our simulation model based on the δf method and give details on how geometric factors due to the toroidal geometry are accounted for. Our particle integration scheme is derived in Section 5.4 and is benchmarked with a guiding center integrator. In addition, the integration scheme is shown to exhibit good conservation properties of kinetic energy and toroidal angular momentum for simulations on long time scales. Section 5.5 shows comparisons with the global GEM code for the DIII-D test case. Finally, a summary and conclusion are given in Section 5.6.

5.1 Magnetic Field Geometry and Computational Domain

In this section, we first introduce a basic toroidal coordinate system used to express the magnetic field model for this study. A field-line-following coordinate system is then defined in terms of the basic toroidal coordinates, which is used to express the so called flux tube domain over which our model equations are solved [5, 66, 71]. Since the toroidal ITG mode is characterized by long wavelengths parallel to the magnetic field and short perpendicular wavelengths, a coordinate system which is aligned with the magnetic field allows for coarser resolution in the direction of the magnetic field. In addition, it allows us to define a minimal simulation volume necessary to capture the relevant physics. With the boundary conditions imposed on the flux tube domain, slicing and rearranging shows it to be equivalent to an annular toroidal wedge domain.

5.1.1 Toroidal Coordinate System

A basic toroidal coordinate system is most easily defined in terms of a cylindrical coordinate system (R, Z, ζ) [72, 73]. Here R is the cylindrical radius and Z is the cylindrical axis. The angle ζ is taken to be the negative azimuthal angle, i.e. increasing ζ corresponds to a clockwise rotation

about the Z axis, so that (R, Z, ζ) is right handed. The Cartesian coordinates (x^1, x^2, x^3) are expressed in terms of (R, Z, ζ) by

$$x^1 = R\cos\zeta$$

$$x^2 = -R\sin\zeta$$

$$x^3 = Z.$$

In the basic toroidal coordinate system, we refer to the Z axis of the cylindrical system as the *major axis* and ζ as the *toroidal angle*. The *minor axis* is a circle in the $Z = 0$ plane with radius $R = R_0$. The toroidal coordinates consist of the toroidal angle ζ, the minor radius r measuring the distance from the minor axis in a constant ζ plane, and an angle about the minor axis θ called the *poloidal angle*. The cylindrical coordinates R and Z are expressed in terms of r and θ by

$$R = R_0 + r\cos\theta$$

$$Z = r\sin\theta.$$

The right handed coordinate system (r, θ, ζ) is illustrated in Figure 5.1. Written in a mixed cylindrical and toroidal coordinates, the assumed form of the magnetic field in our model is given by

$$\mathbf{B} = B_0\left(\frac{R_0}{R}\hat{\zeta} + \frac{r}{q(r)R}\hat{\theta}\right). \tag{5.1}$$

The function $q(r)$ is known as the safety factor and measures the average twist of the field lines on a constant r surface. A purely toroidal field corresponds to $q \to \infty$, and a purely poloidal field corresponds to $q \to 0$. The derivative of q measures the magnetic shear, i.e. the change in field line pitch from one constant r surface to the next. We take the form for $q(r)$ to be a local expansion about reference minor radius r_0 as

$$q(r) = q_0 + (r - r_0)q_0'(r_0).$$

It is noted that the model $\mathbf{B}$ field is divergence free, as can be verified from

$$\nabla\cdot\mathbf{F} = \frac{1}{rR}\left(\frac{\partial}{\partial r}(rRF_r) + \frac{\partial}{\partial\theta}(RF_\theta) + \frac{\partial}{\partial\zeta}(rF_\zeta)\right).$$

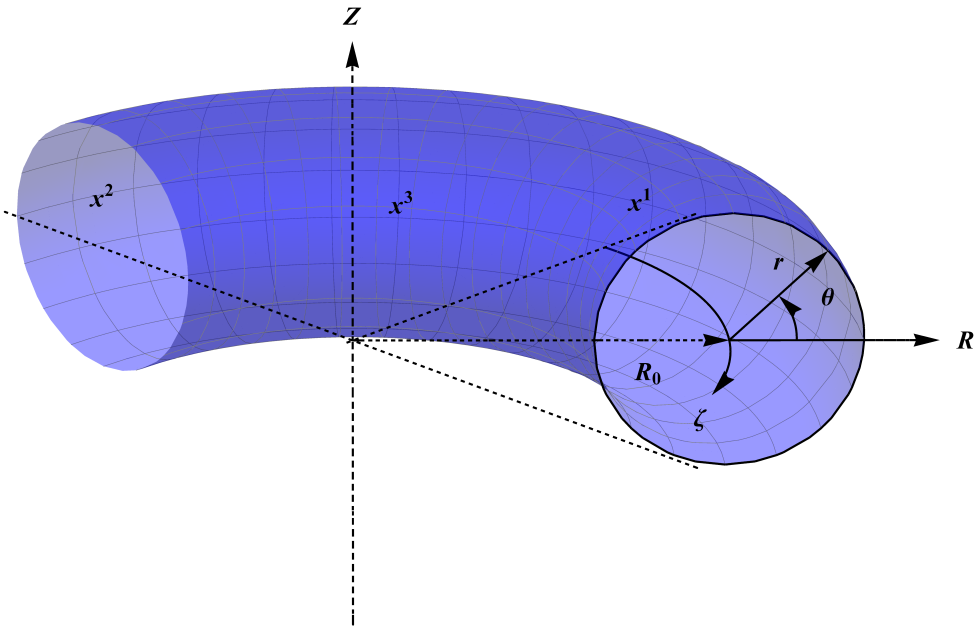

Figure 5.1: Illustration of the Cylindrical and Toroidal Coordinates

5.1.2 Field-Line-Following Coordinates

The simulation domain is defined in terms of a field-line-following coordinate system. Since low-frequency microinstabilities in magnetically confined plasmas are characterized by long wavelengths parallel to the magnetic field and short perpendicular wavelengths, a coordinates system that is aligned with the magnetic field can provide a large computational advantage by reducing the resolution required for these modes and allowing for smaller simulation volumes [5, 71]. In terms of the toroidal coordinates and a reference minor radius r_0, the field-line-following coordinates are defined as

$$x = r - r_0 \tag{5.2}$$

$$y = \frac{r_0}{q_0}\left(\int_0^\theta \hat{q}(r,\theta')d\theta' - \zeta\right) \tag{5.3}$$

$$z = q_0 R_0 \theta, \tag{5.4}$$

where

$$\hat{q}(r,\theta) = \frac{\nabla\zeta \cdot \mathbf{B}}{\nabla\theta \cdot \mathbf{B}}.$$

These coordinates are non-orthogonal and are chosen to have the properties $\mathbf{B} \cdot \nabla x = \mathbf{B} \cdot \nabla y = 0$, from which it follows that

$$\frac{\partial \mathbf{x}}{\partial z} \propto \mathbf{B},$$

where $\mathbf{x}$ is the position vector. For the magnetic field model given in Eq.(5.1), the integral in the definition of the y coordinate can be evaluated explicitly, yielding

$$y = \frac{r_0}{q_0}\left(\frac{2q(r)}{\sqrt{1-(r/R_0)^2}}\arctan\left(\frac{1-r/R_0}{\sqrt{1-(r/R_0)^2}}\tan\frac{\theta}{2}\right) - \zeta\right).$$

The simulation domain is taken to be a rectangular region in the field-line-following coordinates given as

$$D = \left\{(x,y,z)\middle| -\frac{l_x}{2} \le x \le \frac{l_x}{2}, -\frac{l_y}{2} \le y \le \frac{l_y}{2}, -q_0R_0\pi \le z \le q_0R_0\pi\right\}, \tag{5.5}$$

which corresponds to a long, thin tube in physical space following the twisted magnetic field. The mapping of such a region to physical space is illustrated in Figure 5.2.

5.1.3 Boundary Conditions

The boundary conditions for a perturbed quantity A over the flux tube domain are as follows. Periodicity is enforced in y for fixed x and z as

$$A(x, y + l_y, z) = A(x, y, z). \tag{5.6}$$

Fixed boundary conditions are taken in x as

$$A\left(-\frac{l_x}{2}, y, z\right) = A\left(\frac{l_x}{2}, y, z\right) = 0. \tag{5.7}$$

The boundary condition at the end points in z requires some discussion. In selecting the boundary condition, we wish to enforce the periodicity in θ for a fixed toroidal angle. In particular, we require

$$A\left(x(r), y(r, \theta + 2\pi, \zeta), z(\theta + 2\pi)\right) = A\left(x(r), y(r, \theta, \zeta), z(\theta)\right).$$

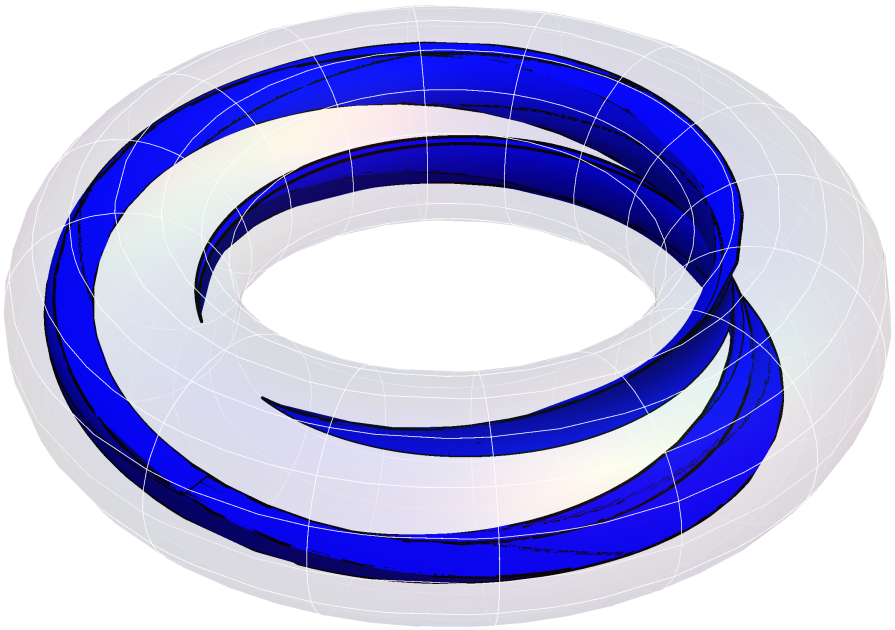

Figure 5.2: Mapping of the rectangular region D in field-line-following coordinates to physical space for $l_x = 48$ and $l_y = 48$.

From the coordinate transformation in Eqs.(5.2)–(5.4), we have

$$y(r, \theta + 2\pi, \zeta) = y(r, \theta, \zeta) + \delta y(r)$$

$$z(\theta + 2\pi) = z(\theta) + 2\pi q_0 R_0,$$

where

$$\delta y(r) = \frac{r_0}{q_0} \int_{-\pi}^{\pi} \hat{q}(r, \theta') d\theta'.$$

The boundary condition in z can therefore be written as the periodicity constraint

$$A\left(x, y + \delta y(x), z + l_z\right) = A(x, y, z), \tag{5.8}$$

where $l_z = 2\pi q_0 R_0$. An example of a function satisfying Eqs.(5.6)–(5.7) and Eq.(5.8) can be given by

$$A(x, y, z) = C(x) e^{i \frac{2\pi n}{l_y} \left(y - \delta y(x) \frac{z}{l_z}\right)} e^{i \frac{2\pi m}{l_z} z},$$

where $C\left(-\frac{l_x}{2}\right) = C\left(\frac{l_x}{2}\right) = 0$. Figure 5.3 illustrates the boundary conditions in y and z in a plane in the field-line-following coordinate system defined by a fixed value of x. Periodic copies of the domain are illustrated in the y direction, corresponding to the condition in Eq.(5.6). At the z boundaries, the domain is extended into a copy that is shifted by $\delta y(x)$ in the y direction, corresponding to Eq.(5.8). The shift in y is chosen to make the end points in z match up along a contour of constant ζ. In Figure 5.3, we also illustrate how a yz-plane in the field-line-following coordinates can be sliced and rearranged to a domain that maps to a toroidal wedge. This provides an alternative view of the boundary condition as enforcing periodicity in θ for the toroidal wedge.

5.2 Equations for Modelling the ITG Instability with Fully Kinetic Ions

In this section, we present the equations for a FK ion model for the toroidal ITG instability. In Chapter 3.4.2, we showed how an approximate equilibrium distribution function, including temperature and density gradients, could be constructed for a FK ion model assuming equilibrium quantities to vary on length scales much larger than the ion gyro-radius. Our starting point was the Vlasov equation for the evolution of the ion distribution function f_i give as

$$\frac{\partial f_i}{\partial t} + \mathbf{v} \cdot \nabla f_i + \frac{q_i}{m_i} \left(\mathbf{E} + \mathbf{v} \times \mathbf{B}\right) \cdot \nabla_{\mathbf{v}} f_i = 0, \tag{5.9}$$

where q_i and m_i are the ion charge and mass respectively and $\mathbf{E}$ is the electric field. Next, it was assumed that f_i could be separated into equilibrium and perturbed parts as $f_i = f_0 + \delta f$. For consistency with Eq.(5.9), f_0 is required to satisfy

$$\mathbf{v} \cdot \nabla f_0 + \frac{q_i}{m_i} \left(\mathbf{v} \times \mathbf{B}\right) \cdot \nabla_{\mathbf{v}} f_0 = 0. \tag{5.10}$$

In Chapter 3.4.2, we assumed a curvilinear coordinate could be found whose gradient is perpendicular to the magnetic field. Here, we choose this coordinate to be the radial field-line-following coordinate x. Our equilibrium distribution function is then taken to depend on R_x given by

$$R_x = x + \frac{m_i}{q_i} \frac{\mathbf{v} \times \hat{\mathbf{b}}}{B} \cdot \nabla x, \tag{5.11}$$

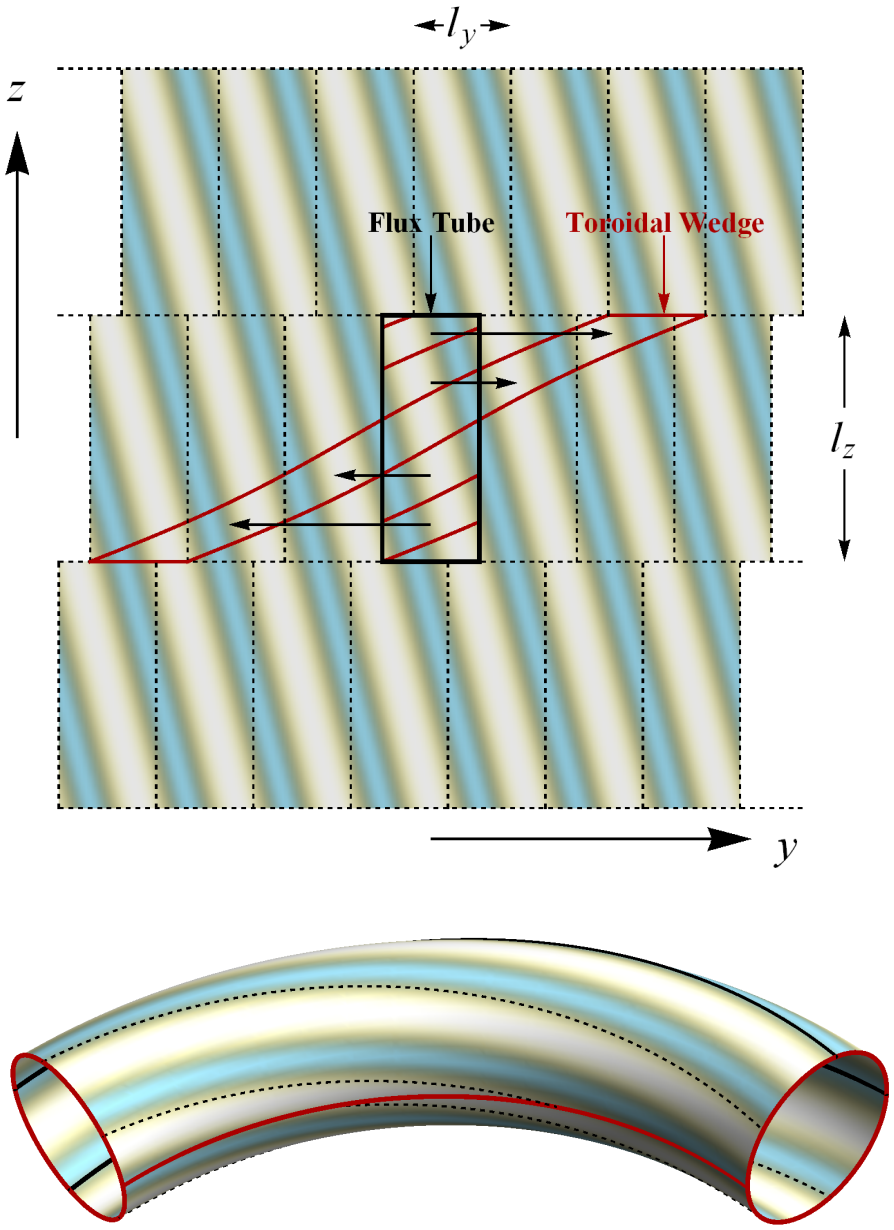

Figure 5.3: Illustration of boundary conditions in y and z in a fixed x plane.

using the decomposition $\mathbf{B} = B\hat{\mathbf{b}}$, where B is the magnitude of $\mathbf{B}$ and $\mathbf{b}$ is the unit vector pointing in the direction of $\mathbf{B}$. In addition, we consider the ion kinetic energy, given by

$$K = \frac{m_i}{2} v^2, \tag{5.12}$$

where $v^2 = \mathbf{v}\cdot\mathbf{v}$. From these two quantities, an equilibrium distribution function can be constructed as $f_0 = f_0(R_x, K)$ to satisfy Eq.(5.10) to first order in the parameter $\epsilon = \rho_i/L_{eq}$, where L_{eq} is such that

$$L_{eq}\frac{\|\nabla f_0\|}{f_0} \sim 1,$$

and we take

$$\rho_i = \frac{m_i v_{th}}{q_i B_0}, \tag{5.13}$$

where v_{th} is the thermal ion velocity and B_0 is the magnetic field strength at the minor axis. With this form for f_0, the perturbed part of the distribution function evolves as

$$\frac{\partial \delta f}{\partial t} + \mathbf{v}\cdot\nabla\delta f + \frac{q_i}{m_i}\left(\mathbf{E} + \mathbf{v}\times\mathbf{B}\right)\cdot\nabla_{\mathbf{v}}\delta f = -q_i\mathbf{E}\cdot\mathbf{v}\frac{\partial f_0}{\partial K} - \nabla x\cdot\left(\frac{\mathbf{E}\times\hat{\mathbf{b}}}{B}\right)\frac{\partial f_0}{\partial R_x}. \tag{5.14}$$

A local Maxwellian is selected for f_0, where temperature and density are allowed to vary with R_x. That is

$$f_0(K, R_x) = \frac{\mathcal{N}_i(R_x)}{\left(2\pi T_i(R_x)/m_i\right)^{3/2}} e^{-K/T_i(R_x)}, \tag{5.15}$$

where T_i and $\mathcal{N}_i$ are the ion equilibrium temperature and density, respectively. With this form, the partial derivatives on the right hand side of Eq.(5.14) are given by

$$\frac{\partial f_0}{\partial K} = -\frac{1}{T_i} f_0 \tag{5.16}$$

$$\frac{\partial f_0}{\partial R_x} = \left(\frac{\frac{\partial \mathcal{N}_i}{\partial R_x}}{\mathcal{N}_i} + \left(\frac{K}{T_i} - \frac{3}{2}\right)\frac{\frac{\partial T_i}{\partial R_x}}{T_i}\right) f_0. \tag{5.17}$$

In the present work, we consider only the linearized version of Eq.(5.14), that is, we neglect the term containing the electric field on the left hand side to study stability in the presence of a small perturbation. In addition, we do not consider effects due to profile variations of T_i and $\mathcal{N}_i$, assuming constant values for the terms depending on R_x in Eqs.(5.16)–(5.17). We use the notation

$$\kappa_T = -\left.\frac{\frac{\partial T_i}{\partial R_x}}{T_i}\right|_{R_x=0}$$

$$\kappa_{\mathcal{N}} = -\left.\frac{\frac{\partial \mathcal{N}_i}{\partial R_x}}{\mathcal{N}_i}\right|_{R_x=0},$$

so that $\kappa_T, \kappa_{\mathcal{N}} > 0$ corresponds to equilibrium quantities that are decreasing with R_x. In addition, we now take T_i and $\mathcal{N}_i$ to represent the constant values $T_i(R_x = 0)$ and $\mathcal{N}_i(R_x = 0)$, respectively. With this notation, the linearized version of Eq.(5.14), assuming Eq.(5.15) and neglecting equilibrium profile variations is written

$$\frac{\partial \delta f}{\partial t} + \mathbf{v}\cdot\nabla\delta f + \frac{q_i}{m_i}(\mathbf{v}\times\mathbf{B})\cdot\nabla_{\mathbf{v}}\delta f = \frac{q_i}{T_i}\mathbf{E}\cdot\mathbf{v}f_0 + \frac{\left(\mathbf{E}\times\hat{\mathbf{b}}\right)\cdot\nabla x}{B}\left[\kappa_{\mathcal{N}} + \left(\frac{m_i v^2}{2T_i} - \frac{3}{2}\right)\kappa_T\right] f_0. \quad (5.18)$$

To close Eq.(5.18) an electrostatic field is assumed as

$$\mathbf{E} = -\nabla\phi, \quad (5.19)$$

where ϕ is the electrostatic potential. An equation for ϕ is given in Chapter 3.1, assuming adiabatic electrons and quasineutrality, as

$$\frac{e\phi}{T_e} = \frac{\delta n}{\mathcal{N}_i}, \quad (5.20)$$

where $-e$ and T_e are the electron charge and temperature, respectively, and δn is obtained by

$$\delta n = \int_{\mathbb{R}^3} \delta f d^3 v. \quad (5.21)$$

An analysis of the model equations Eqs.(5.18)–(5.21) with magnetic field Eq.(5.1) over the domain Eq.(5.5) shows that there are nine dimensionless parameters which determine the behavior of the system. The major radius is normalized by ρ_i defined by Eq.(5.13), where v_{th} is defined from the ion temperature as $v_{th} = \sqrt{T_i/m_i}$. The magnetic field model requires the parameters R_0/ρ_i, r_0/R_0, q_0, and $\hat{s}$ defined as

$$\hat{s} \equiv \frac{r_0}{q_0} q_0'.$$

The equations for the evolution of δf and ϕ require the parameters $\kappa_{\mathcal{N}} R_0$, $\kappa_T R_0$, and τ defined as

$$\tau \equiv \frac{q_i T_e}{e T_i}.$$

Finally, the domain requires l_y/ρ_i and l_x/ρ_i. In this work, we use a base set of parameters, known as the "Cyclone DIII-D base case parameter set" from [70]. These parameters are representative of a typical H-mode plasma and have been used extensively in benchmarking studies for GK codes. The parameter set, in terms of the quantities defined above is given in Table 5.1.

R_0/ρ_i	r_0/R_0	q_0	$\hat{s}$	$\kappa_T R_0$	$\kappa_{\mathcal{N}} R_0$	τ
445.0	0.18	1.4	0.78	6.9	2.2	1.0

Table 5.1: Cyclone DIII-D base case parameter set

5.3 Simulation Model

In this section, we present the details of the numerical implementation of our model. We employ a δf particle-in-cell (PIC) method to solve Eq.(5.18) for the perturbed ion distribution function [38–42]. Although it is trivial to obtain ϕ from Eq.(5.20), some care is required to account for the toroidal geometry when compute the gradient in Eq.(5.19). In addition, the toroidal geometry requires modification in the particle loading step and in depositing the particles to the grid. Details on the integration scheme applied to the particle equations of motion are given in Section 5.4.

5.3.1 δf PIC Model

In our simulations, we employ the δf PIC method to evolve the perturbed part of the ion distribution function in Eq.(5.18). We assume that N_p computational particles have been loaded according to a distribution function, f_L satisfying Eq.(5.10). The computational particles are taken to evolve according to the characteristics of Eq.(5.18), as

$$\frac{d}{dt}\mathbf{x}_p = \mathbf{v}_p \tag{5.22}$$

$$\frac{d}{dt}\mathbf{v}_p = \frac{q_i}{m_i}\left(\mathbf{v}_p \times \mathbf{B}(\mathbf{x}_p)\right). \tag{5.23}$$

for $p = 1, ..., N_p$. By choosing f_L to satisfy Eq.(5.10) with each particle following Eqs.(5.22)–(5.23) the computational particles will be distributed according to f_L for all times throughout the simulation. Next, weights are defined for each computational particle as

$$w_p = \frac{\delta f(\mathbf{x}_p, \mathbf{v}_p)}{f_L(\mathbf{x}_p, \mathbf{v}_p)}. \tag{5.24}$$

By taking the time derivative of Eq.(5.24), we obtain an equation for the evolution of w_p from Eqs.(5.22)–(5.23) and Eq.(5.18) as

$$\frac{dw_p}{dt} = \left(\frac{q_i}{T_i} \mathbf{E} \cdot \mathbf{v} + \frac{\left(\mathbf{E} \times \hat{\mathbf{b}} \right) \cdot \nabla x}{B} \left[\kappa_{\mathcal{N}} + \left(\frac{m_i v^2}{2T_i} - \frac{3}{2} \right) \kappa_T \right] \right) \left. \frac{f_0}{f_L} \right|_{\mathbf{x}_p, \mathbf{v}_p} . \tag{5.25}$$

In our implementation, cylindrical coordinates are used to evolve the particles in phase space according to Eqs.(5.22)–(5.23). Particle positions are transformed back to the field-line-following coordinates to be deposited to the grid.

5.3.2 Loading and Deposit of Computational Particles

Computational particles are loaded according to a spatially uniform Maxwellian distribution function. When equilibrium profile variations are neglected, we can simply take $f_L = f_0$. Loading in velocity space requires a means of generating normally distributed random numbers for the cylindrical velocity components (v_R, v_Z, v_ζ) for which standard techniques can be applied, e.g. the Box-Muller transform [74]. Loading particle positions in the flux tube domain, however, requires some care since uniformly distributed particles in physical space can be strongly nonuniform in the (x, y, z) field-line-following coordinates. In particular, uniformly distributed particles over the flux tube domain follow the probability distribution function f_u given by

$$f_u d^3x = \frac{\chi_D}{V} d^3x, \tag{5.26}$$

where χ_D is the characteristic function for the flux tube domain defined as

$$\chi_D = \begin{cases} 1 & : \mathbf{x} \in D \\ 0 & : \text{else}, \end{cases} \tag{5.27}$$

where D given by Eq.(5.5), V is the volume of D, and d^3x is a differential volume element. Our implementation stores particle positions in both the (x, y, z) coordinates and (R, Z, ζ) coordinates, transforming from one to another when needed. Particle loading is most easily performed in the (x, y, z) coordinates, since the domain is rectangular in this system. In this case, Eq.(5.26) is

written

$$f_u d^3x = \frac{\chi_D}{V} J^{xyz} dxdydz, \tag{5.28}$$

where J^{xyz} is the Jacobian of the field-line-following coordinates, which is given by

$$J^{xyz} = \frac{(x + r_0)\left[R_0 + (x + r_0)\cos\left(\frac{z}{q_0 R_0}\right)\right]}{r_0 R_0}$$

for the geometry of our magnetic field model. Notice that J^{xyz} does not depend on y, hence this coordinate can be loaded uniformly. Rejection sampling [75] is used to load the x and z coordinates according to Eq.(5.28).

The computational domain is divided into $N_x \times N_y \times N_z$ equally sized cells in the (x, y, z) coordinates, with grid point spacings of Δx, Δy and Δz in the x, y and z directions respectively. To approximate δn on the computational grid, we must account for the fact that the volume of the cells is nonuniform due to J^{xyz} being different from unity. At a grid point $\mathbf{X}_j$, we approximate δn by

$$\delta n_j \approx \frac{\mathcal{N}_i}{N_p} \frac{V}{\Delta V_j} \sum_{p=1}^{N_p} w_p S(\mathbf{X}_j - \mathbf{x}_p),$$

where $\Delta V_j = J_j^{xyz} \Delta x \Delta y \Delta z$ and S is the particle shape function defined as

$$S(\mathbf{x}) = S_{1\mathrm{D}}\left(\frac{x}{\Delta x}\right) S_{1\mathrm{D}}\left(\frac{y}{\Delta y}\right) S_{1\mathrm{D}}\left(\frac{z}{\Delta z}\right)$$

with $S_{1\mathrm{D}}$ given by

$$S_{1\mathrm{D}}(x) = \begin{cases} 1 - |x| & : |x| \leq 1 \\ 0 & : |x| > 1. \end{cases}$$

5.3.3 Computation of Gradient

A finite difference scheme is used to compute the gradient in Eq.(5.19). Since our particle push is carried out in the cylindrical coordinates, it is convenient in the weight equation Eq.(5.25) to have $\mathbf{E}$ expressed in terms of its cylindrical components. The electrostatic potential, however, is defined on a grid in the field-line-following coordinates, meaning partial derivatives are most easily

computed in (x, y, z) with finite difference. The cylindrical components of $\mathbf{E}$ can be computed on the field aligned grid by first expressing $\mathbf{E}$ as

$$\mathbf{E} = -\frac{\partial \phi}{\partial x}\nabla x - \frac{\partial \phi}{\partial y}\nabla y - \frac{\partial \phi}{\partial z}\nabla z. \tag{5.29}$$

Taking dot products of Eq.(5.29) with $\hat{R}$, $\hat{Z}$, and $\hat{\zeta}$ then yields

$$\begin{aligned} E_R &= -\frac{\partial \phi}{\partial x}h^{xR} - \frac{\partial \phi}{\partial y}h^{yR} - \frac{\partial \phi}{\partial z}h^{zR} \\ E_Z &= -\frac{\partial \phi}{\partial x}h^{xZ} - \frac{\partial \phi}{\partial y}h^{yZ} - \frac{\partial \phi}{\partial z}h^{zZ} \\ E_\zeta &= -\frac{\partial \phi}{\partial x}h^{x\zeta} - \frac{\partial \phi}{\partial y}h^{y\zeta} - \frac{\partial \phi}{\partial z}h^{z\zeta}, \end{aligned}$$

where $h^{xR} = \nabla x \cdot \hat{R}$, $\quad h^{yR} = \nabla y \cdot \hat{R}$, etc. Explicit expressions for these factors can be derived from the transformation equations Eqs.(5.2)–(5.4) and are given as follows

$$\begin{array}{lll} h^{xR} = \cos\theta & h^{yR} = \dfrac{r_0}{q_0}\left(-\dfrac{\sin\theta}{r}\hat{q}(r,\theta) + \cos\theta\dfrac{\partial}{\partial r}\displaystyle\int_0^\theta \hat{q}(r,\theta')d\theta'\right) & h^{zR} = -\dfrac{R_0 q_0}{r}\sin\theta \\ h^{xZ} = \sin\theta & h^{yZ} = \dfrac{r_0}{q_0}\left(\dfrac{\cos\theta}{r}\hat{q}(r,\theta) + \sin\theta\dfrac{\partial}{\partial r}\displaystyle\int_0^\theta \hat{q}(r,\theta')d\theta'\right) & h^{zZ} = \dfrac{R_0 q_0}{r}\cos\theta \\ h^{x\zeta} = 0 & h^{y\zeta} = -\dfrac{r_0}{q_0 R} & h^{z\zeta} = 0 \end{array}$$

In the simulation model, these quantities are computed at each grid point and stored in an array.

5.4 Integration Scheme for Equilibrium Orbits

The computational particles evolve along the equilibrium trajectories according to Eqs.(5.22)–(5.23). The choice of coordinates used to describe a particle's position will determine how simply Eqs.(5.22)–(5.23) can be expressed. Since our computational domain uses a uniform grid in the field-line-following coordinates, the deposit stage requires particle positions to be in the field-line-following coordinates as well. Expressing Eqs.(5.22)–(5.23) in terms of (x, y, z), however, results in a cumbersome form involving complicated geometric terms. In this work, we have made the choice to use the cylindrical (R, Z, ζ) coordinates in the particle push stage and to use the analytical coordinate transformations of Eqs.(5.2)–(5.4) to convert to (x, y, z) in the deposit stage. In terms

of the cylindrical coordinates, Eqs.(5.22)–(5.23) can be written as

$$\ddot{R} = R\dot{\zeta}^2 + \frac{q_i}{m_i}\left(\dot{Z}B_\zeta - R\dot{\zeta}B_Z\right) \tag{5.30}$$

$$\ddot{Z} = \frac{q_i}{m_i}\left(R\dot{\zeta}B_R - \dot{R}B_\zeta\right) \tag{5.31}$$

$$R\ddot{\zeta} = -2\dot{R}\dot{\zeta} + \frac{q_i}{m_i}\left(\dot{R}B_Z - \dot{Z}B_R\right), \tag{5.32}$$

where dots are used to denote a derivative with respect to time, and we have assumed $\mathbf{B}$ to be expressed as

$$\mathbf{B} = B_R\hat{R} + B_Z\hat{Z} + B_\zeta\hat{\zeta}.$$

Using cylindrical coordinates in the particle push has an additional advantage if more complicated magnetic geometries are to be used. For example, if the more general Miller equilibrium model [71, 76] is used, the integration scheme would not need to be changed. The only changes needed would be in the transformation to (x, y, z) and the expression of $\mathbf{B}$ in the cylindrical coordinates.

5.4.1 Derivation of Integration Scheme

Rather than a direct discretization of Eqs.(5.30)–(5.32), e.g. via Runge-Kutta, we derive a scheme based on discrete variational methods [77–80]. Integration schemes derived from variational methods automatically have a number of desirable properties. In particular, when a strict variational formalism is followed, the resulting algorithm will be symplectic, it will exactly preserve momentum associated with symmetries of the system, and will exhibit excellent energy stability over long simulation times. The study of integration schemes based on variational principles is a broad area of research, which we do not attempt to summarize here. For an overview and historical account, we refer to [77]. The starting point for our integrator is the position-momentum form of the discrete Euler-Lagrange equations, for which a derivation is included in Appendix B. The Lagrangian for the single particle motion described in Eqs.(5.30)–(5.32) is written in the cylindrical coordinates as

$$\mathcal{L} = \frac{m_i}{2}\left(\dot{R}^2 + \dot{Z}^2 + R^2\dot{\zeta}^2\right) + q_i\left(\dot{R}A_R + \dot{Z}A_Z + R\dot{\zeta}A_\zeta\right), \tag{5.33}$$

where $\mathbf{A}$ is the vector potential, defined by

$$\mathbf{B} = \nabla \times \mathbf{A}.$$

It is noted that an integration scheme for the full nonlinear form of Eq.(5.14) could be derived along the same lines presented here by including the contribution of $-q_i\phi$ to the Lagrangian. To form the discrete Lagrangian, we use the trapezoidal rule along with the approximations

$$\begin{aligned}
\dot{R} &\approx \underline{\dot{R}} = \frac{R^{\nu+1} - R^{\nu}}{\Delta t} \\
\dot{Z} &\approx \underline{\dot{Z}} = \frac{Z^{\nu+1} - Z^{\nu}}{\Delta t} \\
\dot{\zeta} &\approx \underline{\dot{\zeta}} = \frac{\zeta^{\nu+1} - \zeta^{\nu}}{\Delta t}
\end{aligned}$$

for $t \in [\nu\Delta t, (\nu+1)\Delta t]$. This choice of quadrature will result in a scheme similar to the velocity Verlet method [81]. The discrete Lagrangian over this interval is then

$$\begin{aligned}
\mathcal{L}_d = {} & \frac{\Delta t m_i}{2}\left[\underline{\dot{R}}^2 + \underline{\dot{Z}}^2 + \frac{(R^{\nu})^2 + (R^{\nu+1})^2}{2}\underline{\dot{\zeta}}^2\right] \\
& + \frac{\Delta t q_i}{2}\left[\underline{\dot{R}}\left(A_R^{\nu} + A_R^{\nu+1}\right) + \underline{\dot{Z}}\left(A_Z^{\nu} + A_Z^{\nu+1}\right) + \underline{\dot{\zeta}}\left(R^{\nu}A_{\zeta}^{\nu} + R^{\nu+1}A_{\zeta}^{\nu+1}\right)\right],
\end{aligned} \tag{5.34}$$

where $\mathbf{A}^{\nu}$ is understood to be the evaluation of $\mathbf{A}$ at the particle's location at time $t = \nu\Delta t$. From the position-momentum form of the discrete Euler-Lagrange equations given in Appendix B, an integration scheme in terms of discrete conjugate momenta can be given by

$$p_R^{\nu} = -\frac{\partial \mathcal{L}_d}{\partial R^{\nu}}, \qquad p_R^{\nu+1} = \frac{\partial \mathcal{L}_d}{\partial R^{\nu+1}} \tag{5.35}$$

$$p_Z^{\nu} = -\frac{\partial \mathcal{L}_d}{\partial Z^{\nu}}, \qquad p_Z^{\nu+1} = \frac{\partial \mathcal{L}_d}{\partial Z^{\nu+1}} \tag{5.36}$$

$$p_{\zeta}^{\nu} = -\frac{\partial \mathcal{L}_d}{\partial \zeta^{\nu}}, \qquad p_{\zeta}^{\nu+1} = \frac{\partial \mathcal{L}_d}{\partial \zeta^{\nu+1}}. \tag{5.37}$$

For our purposes, however, it is more convenient to have an integration scheme to be in terms of the cylindrical velocity components v_R, v_Z, and v_{ζ}. A natural definition of the cylindrical velocity

components in terms of p_R, p_Z, and p_ζ comes from the continuous Lagrangian in Eq.(5.33) by

$$p_R = \frac{\partial \mathcal{L}}{\partial \dot{R}} = m_i \dot{R} + q_i A_R = m_i v_R + q_i A_R \tag{5.38}$$

$$p_Z = \frac{\partial \mathcal{L}}{\partial \dot{Z}} = m_i \dot{Z} + q_i A_Z = m_i v_Z + q_i A_Z \tag{5.39}$$

$$p_\zeta = \frac{\partial \mathcal{L}}{\partial \dot{\zeta}} = m_i R^2 \dot{\zeta} + q_i R A_\zeta = m_i R v_\zeta + q_i R A_\zeta. \tag{5.40}$$

The integration scheme in Eqs.(5.35)–(5.37) written in terms of velocity is then

$$v_R^\nu = -\frac{q_i}{m_i} A_R^\nu - \frac{1}{m_i} \frac{\partial \mathcal{L}_d}{\partial R^\nu}, \qquad v_R^{\nu+1} = -\frac{q_i}{m_i} A_R^{\nu+1} + \frac{1}{m_i} \frac{\partial \mathcal{L}_d}{\partial R^{\nu+1}} \tag{5.41}$$

$$v_Z^\nu = -\frac{q_i}{m_i} A_Z^\nu - \frac{1}{m_i} \frac{\partial \mathcal{L}_d}{\partial Z^\nu}, \qquad v_Z^{\nu+1} = -\frac{q_i}{m_i} A_Z^{\nu+1} + \frac{1}{m_i} \frac{\partial \mathcal{L}_d}{\partial Z^{\nu+1}} \tag{5.42}$$

$$v_\zeta^\nu = -\frac{q_i}{m_i} A_\zeta^\nu - \frac{1}{m_i R^\nu} \frac{\partial \mathcal{L}_d}{\partial \zeta^\nu}, \qquad v_\zeta^{\nu+1} = -\frac{q_i}{m_i} A_\zeta^{\nu+1} + \frac{1}{m_i R^{\nu+1}} \frac{\partial \mathcal{L}_d}{\partial \zeta^{\nu+1}}. \tag{5.43}$$

Furthermore, it is convenient to be able to work directly with $\mathbf{B}$, rather than having to first form a vector potential $\mathbf{A}$. By expressing the curl of $\mathbf{A}$ in cylindrical coordinates, we have

$$B_R = \frac{\partial A_\zeta}{\partial Z} - \frac{1}{R} \frac{\partial A_Z}{\partial \zeta} \tag{5.44}$$

$$B_Z = \frac{1}{R} \left(\frac{\partial A_R}{\partial \zeta} - \frac{\partial}{\partial R} \left(R A_\zeta \right) \right) \tag{5.45}$$

$$B_\zeta = \frac{\partial A_Z}{\partial R} - \frac{\partial A_R}{\partial Z}. \tag{5.46}$$

Next, we illustrate how the components of $\mathbf{A}$ can be eliminated in Eq.(5.41) in favor of the components of $\mathbf{B}$ by means of an approximation. Computing the partial derivatives of the discrete Lagrangian in Eq.(5.34) gives

$$\begin{aligned} v_R^\nu = \underline{\dot{R}} &- \frac{\Delta t}{2} R^\nu \left(\underline{\dot{\zeta}} \right)^2 + \frac{q_i}{2 m_i} \left(A_R^{\nu+1} - A_R^\nu \right) \\ &- \frac{q_i \Delta t}{2 m_i} \left[\underline{\dot{R}} \frac{\partial A_R^\nu}{\partial R^\nu} + \underline{\dot{Z}} \frac{\partial A_Z^\nu}{\partial R^\nu} + \underline{\dot{\zeta}} \frac{\partial}{\partial R^\nu} \left(R^\nu A_\zeta^\nu \right) \right] \end{aligned} \tag{5.47}$$

$$\begin{aligned} v_R^{\nu+1} = \underline{\dot{R}} &+ \frac{\Delta t}{2} R^{\nu+1} \left(\underline{\dot{\zeta}} \right)^2 + \frac{q_i}{2 m_i} \left(A_R^\nu - A_R^{\nu+1} \right) \\ &+ \frac{q_i \Delta t}{2 m_i} \left[\underline{\dot{R}} \frac{\partial A_R^{\nu+1}}{\partial R^{\nu+1}} + \underline{\dot{Z}} \frac{\partial A_Z^{\nu+1}}{\partial R^{\nu+1}} + \underline{\dot{\zeta}} \frac{\partial}{\partial R^{\nu+1}} \left(R^{\nu+1} A_\zeta^{\nu+1} \right) \right] \end{aligned} \tag{5.48}$$

In Eq.(5.47) and Eq.(5.48), we make the following approximations, respectively,

$$A_R^{\nu+1} \approx A_R^{\nu} + \Delta t \left(\underline{\dot{R}} \frac{\partial A_R^{\nu}}{\partial R^{\nu}} + \underline{\dot{Z}} \frac{\partial A_R^{\nu}}{\partial Z^{\nu}} + \underline{\dot{\zeta}} \frac{\partial A_R^{\nu}}{\partial \zeta^{\nu}} \right)$$
$$A_R^{\nu} \approx A_R^{\nu+1} - \Delta t \left(\underline{\dot{R}} \frac{\partial A_R^{\nu+1}}{\partial R^{\nu+1}} + \underline{\dot{Z}} \frac{\partial A_R^{\nu+1}}{\partial Z^{\nu+1}} + \underline{\dot{\zeta}} \frac{\partial A_R^{\nu+1}}{\partial \zeta^{\nu+1}} \right),$$

yielding

$$v_R^{\nu} = \underline{\dot{R}} - \frac{\Delta t}{2} R^{\nu} \left(\underline{\dot{\zeta}} \right)^2 - \frac{q_i \Delta t}{2 m_i} \left[\underline{\dot{Z}} B_{\zeta}^{\nu} - \underline{\dot{\zeta}} R^{\nu} B_Z^{\nu} \right]$$
$$v_R^{\nu+1} = \underline{\dot{R}} + \frac{\Delta t}{2} R^{\nu+1} \left(\underline{\dot{\zeta}} \right)^2 + \frac{q_i \Delta t}{2 m_i} \left[\underline{\dot{Z}} B_{\zeta}^{\nu+1} - \underline{\dot{\zeta}} R^{\nu+1} B_Z^{\nu+1} \right].$$

It is noted that this approximation does not follow the strict variational formalism, and hence we cannot guarantee that theories derived for variational integrators should hold when it is employed. Numerical results, however, from single particle motion seem to exhibit excellent conservation properties for constant of motion despite the approximation. Equations (5.42)–(5.43) can be approximated in the same manner to eliminate components of $\mathbf{A}$, yielding the following procedure for computing $(R^{\nu+1}, Z^{\nu+1}, \zeta^{\nu+1})$ and $(v_R^{\nu+1}, v_Z^{\nu+1}, v_{\zeta}^{\nu+1})$ given $(R^{\nu}, Z^{\nu}, \zeta^{\nu})$ and $(v_R^{\nu}, v_Z^{\nu}, v_{\zeta}^{\nu})$:

- Step 1: Solve the following system of equations for the unknowns $\underline{\dot{R}}$,$\underline{\dot{Z}}$, and $\underline{\dot{\zeta}}$

$$v_R^{\nu} = \underline{\dot{R}} - \frac{\Delta t R^{\nu}}{2} \left(\underline{\dot{\zeta}} \right)^2 - \frac{\Delta t q_i}{2 m_i} \left[\underline{\dot{Z}} B_{\zeta}^{\nu} - \underline{\dot{\zeta}} R^{\nu} B_Z^{\nu} \right] \tag{5.49}$$
$$v_Z^{\nu} = \underline{\dot{Z}} + \frac{\Delta t q_i}{2 m_i} \left[\underline{\dot{R}} B_{\zeta}^{\nu} - \underline{\dot{\zeta}} R^{\nu} B_R^{\nu} \right] \tag{5.50}$$
$$v_{\zeta}^{\nu} = \underline{\dot{\zeta}} R^{\nu} + \Delta t \underline{\dot{\zeta}} \left[\underline{\dot{R}} + \frac{\Delta t \left(\underline{\dot{R}} \right)^2}{2 R^{\nu}} \right] - \frac{\Delta t q_i}{2 m_i} \left[\underline{\dot{R}} B_Z^{\nu} - \underline{\dot{Z}} B_R^{\nu} \right] \tag{5.51}$$

- Step 2: Advance coordinates via

$$R^{\nu+1} = R^{\nu} + \Delta t \underline{\dot{R}} \tag{5.52}$$
$$Z^{\nu+1} = Z^{\nu} + \Delta t \underline{\dot{Z}} \tag{5.53}$$
$$\zeta^{\nu+1} = \zeta^{\nu} + \Delta t \underline{\dot{\zeta}} \tag{5.54}$$

- Step 3: Advance velocity components via

$$v_R^{\nu+1} = \dot{\underline{R}} + \frac{\Delta t R^{\nu+1}}{2}\left(\dot{\underline{\zeta}}\right)^2 + \frac{\Delta t q_i}{2m_i}\left[\dot{\underline{Z}}B_\zeta^{\nu+1} - \dot{\underline{\zeta}}R^{\nu+1}B_Z^{\nu+1}\right] \tag{5.55}$$

$$v_Z^{\nu+1} = \dot{\underline{Z}} - \frac{\Delta t q_i}{2m_i}\left[\dot{\underline{R}}B_\zeta^{\nu+1} - \dot{\underline{\zeta}}R^{\nu+1}B_R^{\nu+1}\right] \tag{5.56}$$

$$v_\zeta^{\nu+1} = \dot{\underline{\zeta}}\frac{(R^\nu)^2 + (R^{\nu+1})^2}{2R^{\nu+1}} + \frac{\Delta t q_i}{2m_i}\left[\dot{\underline{R}}B_Z^{\nu+1} - \dot{\underline{Z}}B_R^{\nu+1}\right]. \tag{5.57}$$

Note that this procedure requires the solution of a nonlinear system of three equations for the unknowns $\dot{\underline{R}}$,$\dot{\underline{Z}}$, and $\dot{\underline{\zeta}}$ in Step 1. Here, this is accomplished with Picard iterations. Denoting the unknowns by $\underline{\mathbf{x}} \equiv [\dot{\underline{R}}, \dot{\underline{Z}}, \dot{\underline{\zeta}}]^T$, the known velocity components by $\underline{\mathbf{v}} \equiv [v_R^\nu, v_Z^\nu, v_\zeta^\nu]^T$, and taking the operator $\mathbb{A}(\underline{\mathbf{x}})$ to represent the right hand side of Eqs.(5.49)–(5.51), we can express these equations as $\mathbb{A}(\underline{\mathbf{x}}) = \underline{\mathbf{v}}$. We note that $\mathbb{A}$ can be decomposed into linear and nonlinear parts as

$$\mathbb{A}(\underline{\mathbf{x}}) = \mathbb{L}\underline{\mathbf{x}} + \mathbb{N}(\underline{\mathbf{x}}).$$

In particular, $\mathbb{N}$ consists of the second terms of Eq.(5.49) and Eq.(5.51). The Picard iteration method proceeds as follows

$$\underline{\mathbf{x}}^0 = \mathbb{L}^{-1}\underline{\mathbf{v}}$$

$$\underline{\mathbf{x}}^i = \mathbb{L}^{-1}\left(\underline{\mathbf{v}} - \mathbb{N}\left(\underline{\mathbf{x}}^{i-1}\right)\right), \qquad i = 1, 2, ...$$

We have found this procedure to converge rapidly, with two iterations being sufficient for a wide range of time step sizes.

5.4.2 Comparison with Guiding Center Integrator

To test our integration scheme, we consider the motion of a trapped particle using the initial conditions in Table 5.2. Parameters for the magnetic field are the same as in Table 5.1. For the integration scheme in Eqs.(5.49)–(5.57), we use Eq.(5.1) expressed in cylindrical components as

$$\mathbf{B} = \frac{B_0 R_0}{Rq(r)}\left(-\frac{Z}{R_0}\hat{R} + \frac{(R - R_0)}{R_0}\hat{Z} + q(r)\hat{\zeta}\right) \tag{5.58}$$

The orbit in the (R, Z) plane and the full 3D orbit are shown in Figure 5.4. We have compared this orbit to a predictor-corrector guiding center particle integrator following the equations of motion

$$\frac{d\mathbf{R}}{dt} = v_\parallel \hat{\mathbf{b}} + \frac{m_i}{q_i B}\hat{\mathbf{b}} \times \left[v_\parallel^2 \left(\hat{\mathbf{b}} \cdot \frac{\partial}{\partial \mathbf{R}} \right) \hat{\mathbf{b}} + \mu B \frac{\partial \ln B}{\partial \mathbf{R}} \right]$$
$$\frac{dv_\parallel}{dt} = -\frac{v_\perp^2}{2} \left(\hat{\mathbf{b}} \cdot \frac{\partial \ln B}{\partial \mathbf{R}} \right),$$

where $\mathbf{R}$ is the guiding center position, μ is the magnetic moment defined by $\mu = v_\perp^2/2B$ with $v_\perp$ the magnitude of the velocity perpendicular to $\hat{\mathbf{b}}$, and $v_\parallel$ is the velocity component along $\hat{\mathbf{b}}$. Initial conditions for the guiding center integrator are given in Table 5.3. For both the guiding center integrator and our FK integrator, a time step size of $\Omega_i \Delta t = 0.125$ is taken, and the simulations are run to $\Omega_i t = 2.5 \times 10^4$. Both integrators correctly capture the trapped particle orbit and agree well with each other.

R/R_0	Z/R_0	ζ	$v_R/R_0\Omega_i$	$v_Z/R_0\Omega_i$	$v_\zeta/R_0\Omega_i$
1.176	3.912×10^{-3}	-4.258×10^{-4}	3.371×10^{-3}	3.371×10^{-3}	1.798×10^{-3}

Table 5.2: Initial conditions for FK integrator.

R/R_0	Z/R_0	ζ	$v_\parallel/R_0\Omega_i$	$B_0\mu/\left(R_0\Omega_i\right)^2$
1.180	0.000	0.000	2.212×10^{-3}	1.232×10^{-5}

Table 5.3: Initial conditions for GC integrator.

5.4.3 Constants of Motion

The conservation properties of our fully kinetic integrator are tested with two exact constants of motion that can be found for the system Eqs.(5.22)–(5.23), using the form of $\mathbf{B}$ from Eq.(5.1). These are the kinetic energy, K defined in Eq.(5.12) and the toroidal angular momentum, p_ζ defined

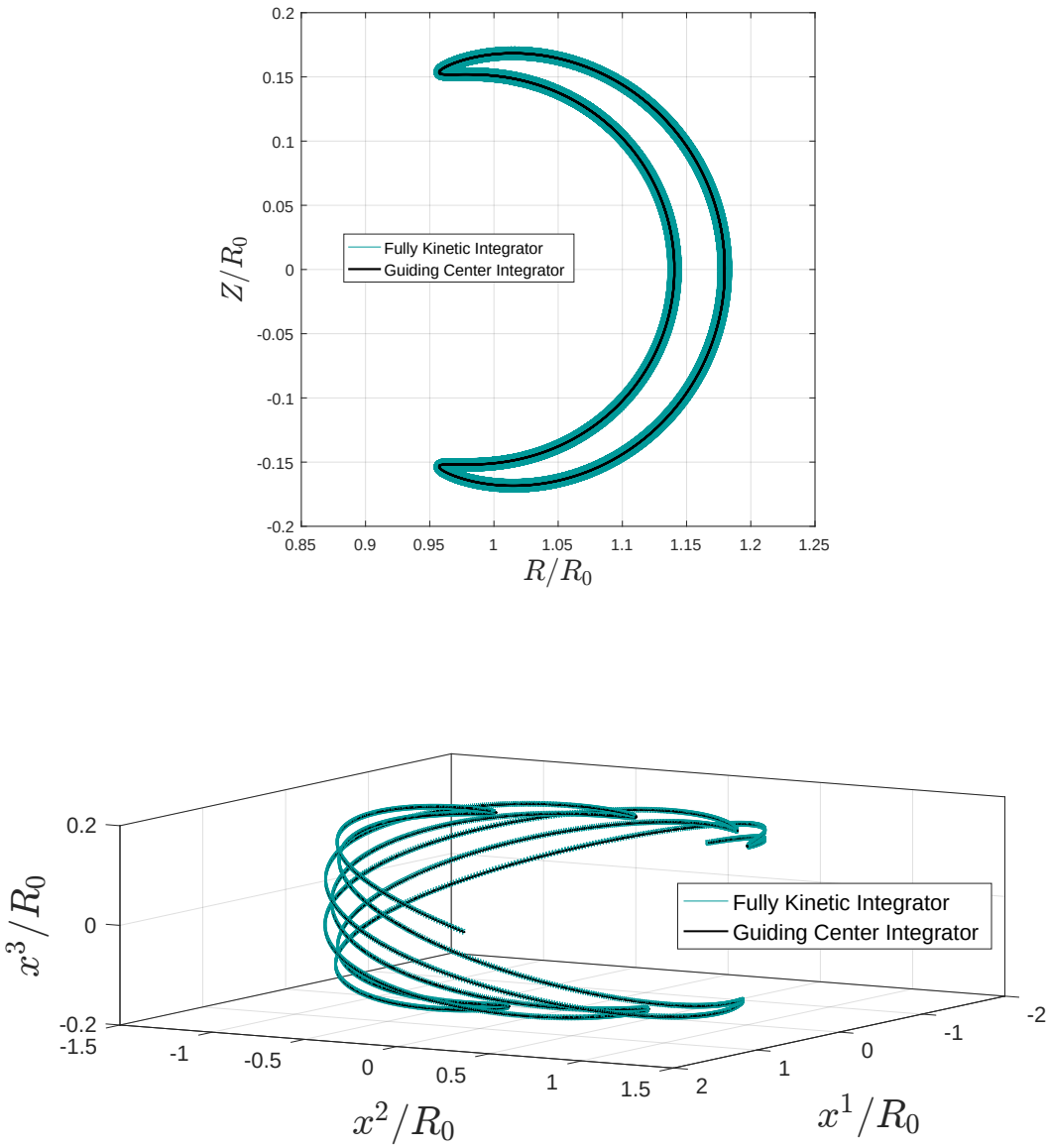

Figure 5.4: Comparison of FK Variational Integrator to Guiding Center Integrator

in Eq.(5.40). The kinetic energy can be computed from the cylindrical velocity components simply as

$$K = \frac{m_i}{2}\left(v_R^2 + v_Z^2 + v_\zeta^2\right).$$

The toroidal angular momentum is conserved due to the symmetry of **B** with respect to the toroidal angle. Its computation, however, requires the toroidal component of a vector potential. From Eqs.(5.44)–(5.46), it can be verified that a vector potential for the field model in Eq.(5.58) is given by

$$\mathbf{A} = -\frac{B_0 R_0 Z}{R}\hat{R} - \frac{B_0}{R}\int_{r_0}^{r} \frac{r'}{q(r')} dr' \hat{\zeta},$$

from which we arrive at

$$p_\zeta = m_i R v_\zeta - q_i B_0 \int_{r_0}^{r} \frac{r'}{q(r')} dr'.$$

In Figure 5.5, we examine the relative variation of K and p_ζ over a time period of 2.5×10^4 for different time step sizes. Initial conditions are taken from Table 5.2. The amount by which the conservation of these quantities is violated is characterized by bounded oscillations, with amplitudes that decrease with the time step size. Figure 5.6 shows the amplitude of these oscillations as a function of the time step size. The amplitudes are shown to decrease as $O(\Delta t^2)$ for both K and p_ζ.

5.5 Toroidal ITG Instability Simulations

In this section, we present simulation results for the FK ion model applied to the ITG instability model. The "Cyclone DIII-D base case parameter set" given in Table 5.1 is used to benchmark our algorithm. In Figure 5.7, a scan is performed measuring real frequencies and growth rates as a function of the parameter R_0/L_T, where $L_T = \kappa_T^{-1}$. The domain size is taken to be $l_x = 32\rho_i$, $l_y = 12.57\rho_i$, $l_z = 3914.4\rho_i$, and all other parameters are taken from Table 5.1. Comparisons are made with the global GEM code and good agreement is observed. For the case with $R_0/L_T = 6.9$, the real frequencies of the two codes agree within 6 per cent and the growth rates agree within 17 per cent. For the FK code, we have $\omega_R/\Omega_i = -2.40 \times 10^{-3}$ and $\gamma/\Omega_i = 6.0 \times 10^{-4}$, and for the global GEM gyrokinetic code, we have $\omega_R/\Omega_i = -2.26 \times 10^{-3}$ and $\gamma/\Omega_i = 7.0 \times 10^{-4}$. For the simulations in Figure 5.7, the following resolution was used in the FK code: $N_x = 128$, $N_y = 32$, $N_z = 48$, corresponding to $\Delta x = 0.24\rho_i$, $\Delta y = 0.39\rho_i$, and $\Delta z = 81.55\rho_i$. A time step

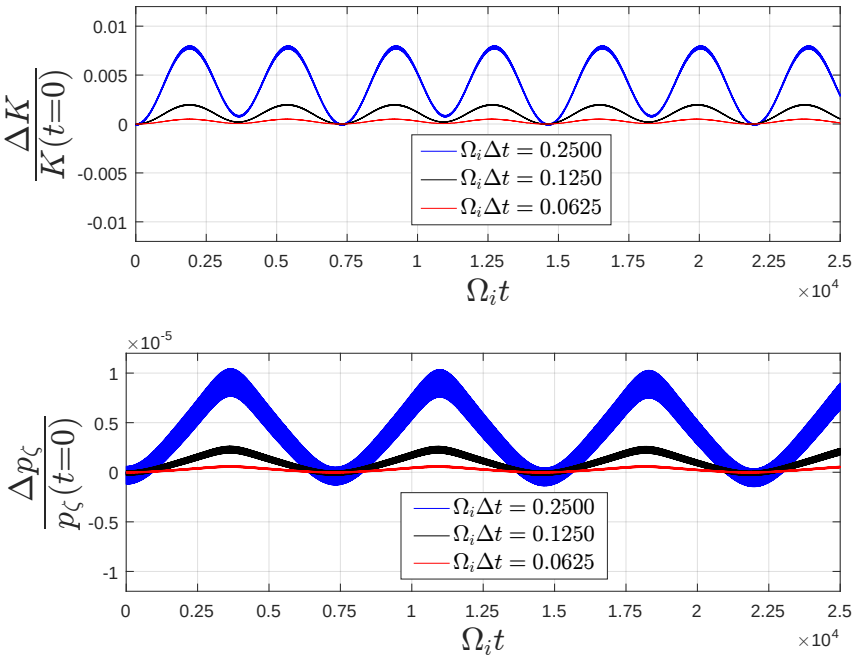

Figure 5.5: Conservation of kinetic energy and toroidal angular momentum in fully kinetic integrator.

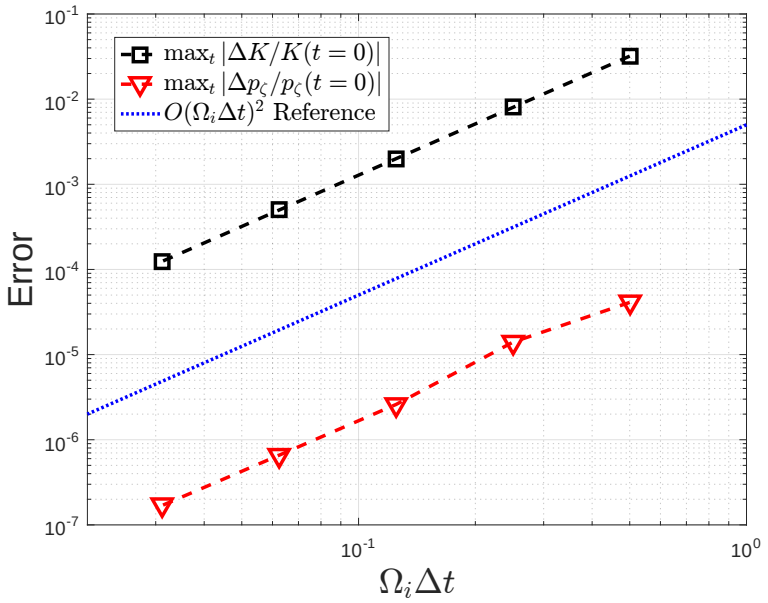

Figure 5.6: Convergence of kinetic energy and toroidal momentum conservation with $\Omega_i \Delta t$

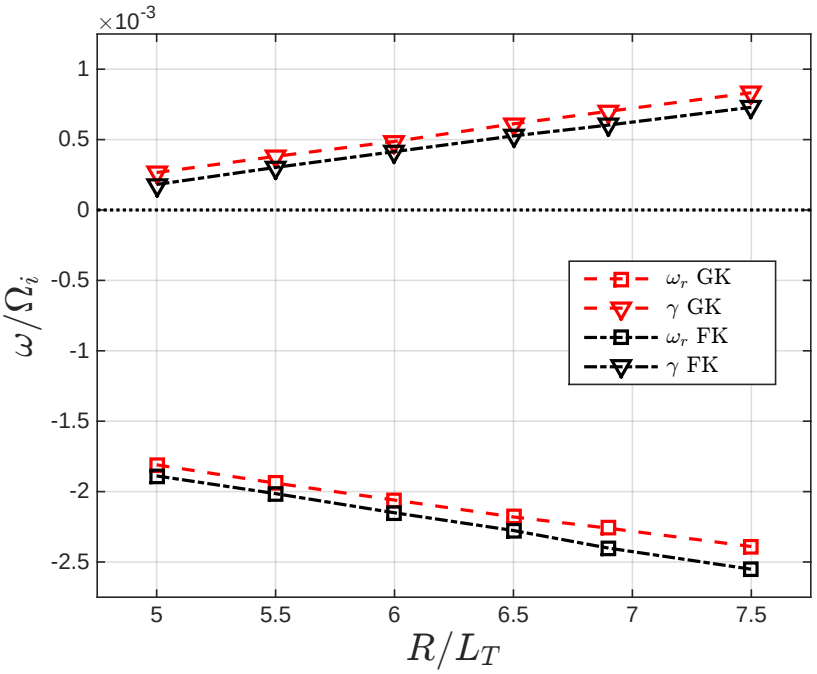

Figure 5.7: Real frequencies and growth rates as a function of R_0/L_T.

size of $\Omega_i \Delta t = 0.2$ was used with ~ 21 particles per cell. An additional test was performed for the case of $R_0/L_T = 6.9$ using the resolution $N_x = 256$, $N_y = 64$, $N_z = 96$ with $\Omega_i \Delta t = 0.125$ and ~ 21 particles per cell. This produced no significant difference in the real frequency or damping rate, suggesting that our FK ion model implementation is converged for the results in Figure 5.7.

5.6 Summary and Conclusions

In this chapter, we have explored the use of a fully kinetic ion model to simulate microinstabilities in a toroidal magnetized plasma. Key to this work was the development to include equilibrium densities in FK ion models for a weakly inhomogeneous magnetic field, which was presented in Chapter 3.4.2. Full geometric effects due to the toroidal flux tube geometry have been accounted for in the FK implementation. For this work, a particle integration scheme has been developed, based on variational principles, which is shown to provide accurate and stable orbits over long simulation times. In addition, the integration scheme has been shown to accurately conserve constants

of motion along a particles' trajectory. FK ion simulations of the toroidal ITG instability have been carried out for the first time, and good agreement was shown between the FK ion implementation and the global GEM gyrokinetic code. This work provides a starting point for developing a FK ion model that can be used to benchmark GK codes. Future work includes the addition of more elements of realism to the FK code, including nonlinear terms, electromagntic effects, and kinetic electrons.

Chapter 6

Finite Time Step and Spatial Grid Effects in δf Simulation of Warm Plasmas

The δf method for particle simulation was developed in the nineties as a way to reduce the noise from particle-in-cell (PIC) methods introduced by using discrete particles to represent continuous distribution functions over phase space [38–42]. In this algorithm, the full particle distribution function f is separated into a "background" equilibrium part f_0, which is known analytically, and a perturbed part δf which is solved numerically by evolving the equations of motion along with a particle "weight" equation for a finite number of computational particles. Previous studies regarding the numerical properties of the δf method have focused on its sampling noise properties [40, 41], but to the our knowledge, comprehensive methods for evaluating the effects introduced by the discretization schemes used with the δf method have not previously been developed.

In this chapter, we introduce a technique, motivated by the work of Langdon [82], to analyze the time integration scheme used in the δf method for a uniform, warm, periodic or infinite plasma in the linear regime. The current work is published in [23]. In the analysis, we consider the evolution of the particle weights at discrete time increments along the unperturbed particle trajectories. An end point condition on the particle motion establishes a connection between the value of δf along the characteristic followed by a Lagrangian particle and the value of δf at a fixed Eulerian point in phase space. The related Eulerian equation for δf is valid when the scheme has converged in the number of computational particles, and it includes the effects of the finite time step. An explicit expression for δf is obtained from the Eulerian equation by assuming a von Neumann-like ansatz

for all spatial and time varying quantities.

To illustrate the use of this technique, we perform a complete analysis of an implicit integration scheme applied to a kinetic ion, adiabatic electron plasma model which allows the propagation of ion acoustic waves. Here, we simply lay out the method for numerical analysis of the δf method using the test problem important in our particular application area. This analysis can be generalized and applied to other physical models, for example, to analyze the numerical properties associated with δf drift-kinetic electrons in gyrokinetic turbulence simulations. It is shown that the numerical properties of the δf method applied to the test problem are independent of a parameter characterizing the implicitness of the integration scheme. The time integration analysis is then combined with the spatial grid analysis of Langdon [83]. A modified dispersion relation including effects of both Δt and Δx is obtained from which the lowest order corrections to the real frequency and damping rate are found. Numerical solutions of the modified dispersion relation are also used to study the stability of the simulation model, and a CFL-like stability condition is found for the δf method when the ion temperature is low. To validate our results, simulations are performed and compared to the theory.

In analyzing the numerical properties of the δf method, one of our goals is to assess differences from the conventional full-f method. To address this, we compare the δf model with a full-f formulation for the same model problem, including the same implicit integration scheme. Following the analysis of Langdon, we obtain the modified dispersion relation for the full-f method. Some comments should be made regarding the linear analysis used to make comparisons of the two methods. In the full-f method, the linear correction to the number density due to a small electric field is introduced through the perturbed particle orbits. In the δf method, however, the linear correction is introduced through the particle weights, and the perturbed particle orbits account for a correction at a higher order. Hence, the time integration scheme used for the particle weight equations determine the finite time step effects on the linear dispersion relation for the δf method, whereas the time integration scheme used for the equations of motion determine the finite time step effects on the linear dispersion relation for the full-f method.

This chapter is organized as follows. In Section 6.1, we present the δf and full-f methods for Particle-in-Cell (PIC) simulations of a kinetic ion species and discuss the linearization of both methods. In Section 6.2, a field equation is introduced to close the simulation model, assuming adiabatic electrons and quasi-neutrality. The closed system allows for ion Landau damping of ion acoustic waves. In Section 6.3, our time integration analysis for the δf method is presented and applied to the implicit scheme used to advance the ions. The time integration analysis of Langdon is applied to the same implicit scheme used with the particle equations of motion in the full-f method in order to make comparisons. In Section 6.4, the spatial grid analysis of Langdon is applied to both the δf and full-f methods to derive modified dispersion relations including the combined effects of Δt and Δx. In Section 6.5, the modified dispersion relations are studied in detail, and results regarding the accuracy and stability of the numerical methods are obtained. Simulations are performed and used to validate the numerical analysis.

6.1 Full-f and δf Particle-in-Cell Methods for Vlasov Ions

We consider the Vlasov equation to describe the evolution of the distribution function f for a uniform, unmagnetized ion species with charge e

$$\frac{\partial f}{\partial t} + \mathbf{v} \cdot \nabla f + \frac{e}{m_i} \mathbf{E} \cdot \nabla_{\mathbf{v}} f = 0. \tag{6.1}$$

In this section, we present the equations used for both the full-f and δf methods for PIC simulation of Eq.(6.1). These methods are both based on evolving a system of N_p computational particles through phase space along the characteristics of Eq.(6.1). We consider simulations in which the objective of the PIC model is to obtain a number density which is coupled to a field equation for $\mathbf{E}$. A specific example of such a field equation is given in Section 6.2 and studied in detail for an implicit time integration scheme applied to the PIC model. The linearization of both PIC methods will be discussed at the end of this section.

6.1.1 Full-f Method

We first present the familiar full-f method for solving Eq.(6.1). This method is discussed in a number of references including [32, 33]. The computational particles (ions) are taken to follow the Newton-Lorentz equations of motion

$$\begin{aligned} \frac{d\mathbf{x}_p(t)}{dt} &= \mathbf{v}_p(t) \\ \frac{d\mathbf{v}_p(t)}{dt} &= \frac{e}{m_i}\mathbf{E}(\mathbf{x}_p(t), t) \end{aligned} \tag{6.2}$$

for $p = 1, ..., N_p$, and the corresponding distribution function at a grid point $\mathbf{X}_j$ is given by the PIC approximation to the Klimontovich representation

$$f_i(\mathbf{x}, \mathbf{v}, t) \approx \frac{N_i}{\Delta V N_p} \sum_{p=1}^{N_p} S_{\mathbf{x}}(\mathbf{X}_j - \mathbf{x}_p(t)) \delta_{\mathbf{v}}(\mathbf{v} - \mathbf{v}_p(t)). \tag{6.3}$$

Here, N_i is the number of physical ions to be modelled, ΔV is the volume of a grid cell, and $\delta_{\mathbf{v}}$ is a dimensional Dirac delta function with units of velocity$^{-d_v}$ with d_v the velocity dimensions for the simulation. The function $S_{\mathbf{x}}$ is called the shape function. The shape function is supported on a set of finite measure and is used to obtain the velocity moments of f_i at the grid points. By integrating Eq.(6.3) over velocity space, we have the following expression for the number density at grid point $\mathbf{X}_j$

$$n_j(t) \approx \frac{N_i}{\Delta V N_p} \sum_{p=1}^{N_p} S_{\mathbf{x}}(\mathbf{X}_j - \mathbf{x}_p(t)).$$

Typically, the same function $S_{\mathbf{x}}$ is used in Eq.(6.2) to interpolate the electric field values on grid points to a particle's location as

$$\mathbf{E}(\mathbf{x}_p(t), t) \approx \sum_j \mathbf{E}_j(t) S_{\mathbf{x}}(\mathbf{X}_j - \mathbf{x}_p(t)). \tag{6.4}$$

6.1.2 δf Method

The δf method starts with the assumption that f_i can be separated into a known time independent equilibrium part and an unknown perturbed part as $f_i = f_0 + \delta f$. Particle weights are defined for each computational particle as

$$w_p(t) \equiv \frac{\delta f(\mathbf{x}_p(t), \mathbf{v}_p(t), t)}{f_i(\mathbf{x}_p(t), \mathbf{v}_p(t), t)}.$$

The positions and velocities of the computational particles are taken to follow Eq.(6.2), as in the full-f method, and the weights are evolved according to

$$\frac{dw_p(t)}{dt} = -(1 - w_p(t))\frac{e}{m_i}\mathbf{E}(\mathbf{x}_p(t), t) \cdot \nabla_{\mathbf{v}_p} \ln f_0(\mathbf{v}_p), \tag{6.5}$$

where the approximation Eq.(6.4) is used in the PIC model. The distribution function at grid point $\mathbf{X}_j$ is then approximated as

$$f_i(\mathbf{X}_j, \mathbf{v}, t) \approx f_0(\mathbf{v}) + \frac{N_i}{\Delta V N_p} \sum_{p=1}^{N_p} w_p(t) S_{\mathbf{x}}(\mathbf{X}_j - \mathbf{x}_p(t)) \delta_{\mathbf{v}}(\mathbf{v} - \mathbf{v}_p(t)), \tag{6.6}$$

with the computational particles evolve according to Eq.(6.2) and the weights according to Eq.(6.5). An integration of Eq.(6.6) over velocity space yields for the number density at $\mathbf{X}_j$

$$n_j(t) \approx n_0 + \frac{N_i}{\Delta V N_p} \sum_{p=1}^{N_p} w_p(t) S_{\mathbf{x}}(\mathbf{X}_j - \mathbf{x}_p(t)). \tag{6.7}$$

6.1.3 Linearization of the PIC models

The time stepping analysis for both the full-f and δf methods requires a linearization of the PIC model equations with respect to a small perturbation from equilibrium. This is accomplished for the full-f method by splitting $\mathbf{x}_p$ and $\mathbf{v}_p$ into unperturbed and perturbed parts as

$$\mathbf{x}_p = \mathbf{x}_p^{(0)} + \mathbf{x}_p^{(1)}$$

$$\mathbf{v}_p = \mathbf{v}_p^{(0)} + \mathbf{v}_p^{(1)}$$

where quantities with a superscript $^{(0)}$ are independent of the electric field. The unperturbed particle orbit is then

$$\mathbf{x}_p^{(0)}(t) = \mathbf{x}_p^{(0)}(t = 0) + t\mathbf{v}_p^{(0)} \tag{6.8}$$

with $\mathbf{v}_p^{(0)}$ constant in time. The linear correction to the particle orbit is given by

$$\frac{d\mathbf{x}_p^{(1)}(t)}{dt} = \mathbf{v}_p^{(1)}(t)$$

$$\frac{d\mathbf{v}_p^{(1)}(t)}{dt} = \frac{e}{m_i}\mathbf{E}^{(1)}(\mathbf{x}_p^{(0)}(t), t)$$

where $\mathbf{E}^{(1)}$ is self consistent with the linear approximation to the number density $n_j(t) \approx n_0 + \delta n_j^{(1)}(t)$, where $\delta n_j^{(1)}(t)$ is given by

$$\delta n_j^{(1)}(t) = -\frac{N_i}{\Delta V N_p} \nabla \cdot \sum_{p=1}^{N_p} \mathbf{x}_p^{(1)}(t) S(\mathbf{X}_j - \mathbf{x}_p^{(0)}(t)). \tag{6.9}$$

This is the linearized trajectory method as described in [84].

For the δf method, the linear correction comes into the number density through the particle weights rather than through the perturbed particle orbits. Details on the linearization of the δf PIC model can be found in Appendix C. Assuming $\mathbf{x}_p^{(0)}$ satisfies Eq.(6.8) with $\mathbf{v}_p^{(0)}$ constant, the linear particle weight $w_p^{(1)}$ evolves as

$$\frac{dw_p^{(1)}(t)}{dt} = -\frac{e}{m_i} \mathbf{E}^{(1)}(\mathbf{x}_p^{(0)}(t), t) \cdot \nabla_{\mathbf{v}_p^{(0)}} \ln f_0(\mathbf{v}_p^{(0)}).$$

Here $\mathbf{E}^{(1)}$ is the electric field that is self consistent with the linear approximation to the number density $n_j(t) \approx n_0 + \delta n_j^{(1)}(t)$, where $\delta n_j^{(1)}(t)$ is given by

$$\delta n_j^{(1)}(t) = \frac{N_i}{\Delta V N_p} \sum_{p=1}^{N_p} w_p^{(1)}(t) S(\mathbf{X}_j - \mathbf{x}_p^{(0)}(t)) \tag{6.10}$$

and the following definition for $w_p^{(1)}$ applies as a result of linearization:

$$w_p^{(1)}(t) = \frac{\delta f(\mathbf{x}_p^{(0)}(t), \mathbf{v}_p^{(0)}, t)}{f_0(\mathbf{v}_p^{(0)})}. \tag{6.11}$$

When considering the discrete time PIC method, it should be kept in mind that modifications to the linear dispersion relation in the full-f method due to finite Δt result from the integration scheme used for the particle equations of motion, whereas in the δf method, modifications result from the integration scheme used for the particle weight equation. The corrections due to the perturbed particle orbits come in at a higher order in the δf method, and therefore any consistent integration scheme applied to the particle equations of motion should produce similar results at least for simulations running in the linear regime. Both PIC methods when linearized, provide approximations to the linearized Vlasov equation. The linearized Vlasov equation is simply given by

$$\frac{\partial \delta f}{\partial t} + \mathbf{v} \cdot \nabla \delta f + \frac{e}{m_i} \mathbf{E}^{(1)} \cdot \nabla_{\mathbf{v}} f_0 = 0. \tag{6.12}$$

6.2 Model for Electrons and Electric Field

For our analysis, we consider an adiabatic electron model, which when combined with a quasi-neutrality assumption, will provide an equation coupling the electrostatic $\mathbf{E}$ field with $\delta n \equiv n - n_0$, to close our simulation model. Linearization of a Boltzmann distribution yields for the perturbed electron number density

$$\delta n_e(\mathbf{x}, t) = n_0 \frac{e\phi(\mathbf{x}, t)}{T_e}$$

where $-e$ is the electron charge and T_e the electron temperature taken to be constant. Specifying $\mathbf{E} = -\nabla\phi$ and assuming quasi-neutrality $\delta n_e = \delta n_i \equiv \delta n$, we have

$$\mathbf{E}(\mathbf{x}, t) = -\frac{T_e}{e} \frac{\nabla \delta n(\mathbf{x}, t)}{n_0}. \tag{6.13}$$

Our model is then closed from δn obtained directly from the ions, which for the linear PIC models are the second terms on the right hand sides of Eq.(6.9) and Eq.(6.10). We chose this field model to study because it is the electrostatic limit of the generalized Ohm's law derived in [15] for the kinetic ion, fluid electron model. This reduced model allows for the propagation and ion Landau damping of ion acoustic waves. A dispersion relation from Vlasov theory can be derived using Eq.(6.12) and Eq.(6.13), which is used to compare the dispersion of our PIC models. For an arbitrary equilibrium distribution f_0, the dispersion relation is

$$\epsilon_0(\omega, \mathbf{k}) \equiv 1 - \frac{T_e}{m_i n_0} \mathbf{k} \cdot \int \frac{\nabla_{\mathbf{v}} f_0(\mathbf{v})}{\mathbf{k} \cdot \mathbf{v} - \omega} d\mathbf{v} = 0.$$

We assume a Maxwellian background distribution

$$f_0(v) = f_M(v) = \frac{n_0}{(2\pi)^{3/2} v_{th}^3} e^{-v^2/2v_{th}^2},$$

where we define $v_{th} \equiv \sqrt{T_i/m_i}$ with T_i being the ion temperature. In this case, we have

$$\epsilon_0(\zeta) = 1 - \frac{1}{2T} Z'(\zeta/\sqrt{2}) = 0, \tag{6.14}$$

defining the parameters T to be the ratio of ion and electron temperatures, $T = T_i/T_e$, and ζ to be the phase velocity normalized by the ion thermal velocity, $\zeta = \omega/kv_{th}$, assuming $\mathbf{k} = k\hat{x}$. Here

$Z(\theta)$ is the plasma dispersion function of Fried and Conte [46], defined by the complex integral

$$Z(\theta) = \frac{1}{\sqrt{\pi}} \int_{-\infty}^{\infty} \frac{e^{-s^2}}{(s-\theta)} ds, \qquad \text{Im } \theta > 0$$

and its analytic continuation for Im $\theta \leq 0$.

6.3 Analysis of an Implicit Time Integration Scheme

In analyzing the finite time step and spatial grid effects, discrete particle effects are ignored, assuming convergence in the number of computational particles. For the remainder of the chapter, we drop the subscript p from particle quantities, since there isn't a need to distinguish between individual particles in the analysis. A subscript ν is now used instead to index a quantity evaluated at time step $\nu\Delta t$. We consider the implicit ODE time integration scheme used in [15] with a time centering parameter α. The scheme is convergent for $0 \leq \alpha \leq 1$ and yields the familiar methods of forward Euler, trapezoidal, and backward Euler for the values of $\alpha = 0$, $\alpha = 1/2$, and $\alpha = 1$ respectively. It is a first order accurate ODE integration method for all values of α except for the special case of $\alpha = 1/2$, which is second order accurate. See for example, Chapter 6 of [85]. It is implicit for all α except for $\alpha = 0$. The implicit equations can be solved, for example, through a Picard iteration scheme or with a Jacobian-free Newton-Krylov solver [58, 61].

The time integration analysis can be regarded as either an exact analysis of the scheme applied to the linearized PIC models described in the previous section or as an approximate analysis for the nonlinear PIC methods when initialized by a small perturbation and run for a short time. The unperturbed particle orbits in our model will be reproduced exactly due to the consistency of the integration scheme, yielding

$$\mathbf{x}_{\nu}^{(0)} = \mathbf{x}_{\nu=0}^{(0)} + \nu\Delta t \mathbf{v}^{(0)} \tag{6.15}$$

where $\mathbf{v}^{(0)}$ is constant in time. The unperturbed velocity being constant in time allows for a simple analysis. The analysis can be extended to more complex models, for example a magnetized plasma model, provided that the time discretized unperturbed orbits can be solved analytically.

Since we are interested in the evolution of the distribution function rather than the individual particle trajectories, we will make the connection between a Lagrangian particle's phase space location at time step ν and the Eulerian phase space coordinates. Suppose we wish to know the distribution function at the discrete time step $\nu = N$. Taking a fixed, arbitrary point $(\mathbf{x}, \mathbf{v})$, we consider a particle with an unperturbed orbit which passes through this point and enforce that it does so at $\nu = N$. In particular, we require that

$$\mathbf{x}^{(0)}_{\nu=N} = \mathbf{x}$$

$$\mathbf{v}^{(0)}_{\nu=N} = \mathbf{v}$$

in Eq.(6.15), which gives for the unperturbed particle orbit

$$\mathbf{x}^{(0)}_{\nu} = \mathbf{x} + (\nu - N)\Delta t \mathbf{v}. \tag{6.16}$$

This can be thought of as choosing the particles with initial conditions such that they will contribute to the density in the infinitesimal region around $(\mathbf{x}, \mathbf{v})$ at time step $\nu = N$. It assumes convergence in the number of computational particles, so we can assume a continuous distribution function. Since the point $(\mathbf{x}, \mathbf{v})$ and time $\nu = N$ were chosen arbitrarily, knowing the distribution function for these arguments will give the distribution function over all of phase space and at all discrete time values.

6.3.1 Time Integration Analysis for the δf Method

Applying the time integration scheme from [15] to the δf method yields the following discrete equation for the linear particle weights

$$\frac{w^{(1)}_{\nu} - w^{(1)}_{\nu-1}}{\Delta t} = -(1-\alpha) G^{(1)}_{\nu-1}(\mathbf{x}^{(0)}_{\nu-1}, \mathbf{v}^{(0)}) - \alpha G^{(1)}_{\nu}(\mathbf{x}^{(0)}_{\nu}, \mathbf{v}^{(0)}),$$

where we have defined

$$G^{(1)}_{\nu}(\mathbf{x}^{(0)}_{\nu}, \mathbf{v}^{(0)}) \equiv \frac{e}{m_i} \mathbf{E}^{(1)}_{\nu}(\mathbf{x}^{(0)}_{\nu}) \cdot \nabla_{\mathbf{v}^{(0)}} \ln f_0(\mathbf{v}^{(0)}).$$

Noting the definition for $w^{(1)}$ in Eq.(6.11) and using the Eulerian referenced particle expression in Eq.(6.16), we obtain an Eulerian equation relating δf at the discrete time steps $\nu = N$ and

$\nu = N - 1$

$$\begin{aligned} \delta f_N(\mathbf{x}, \mathbf{v}) = \delta f_{N-1}(\mathbf{x} - \Delta t \mathbf{v}, \mathbf{v}) - \\ \Delta t \left[(1-\alpha) G^{(1)}_{N-1}(\mathbf{x} - \Delta t \mathbf{v}, \mathbf{v}) + \alpha G^{(1)}_N(\mathbf{x}, \mathbf{v}) \right] f_0(\mathbf{v}). \end{aligned} \tag{6.17}$$

Next, to obtain an explicit expression for δf, we take a von-Neumann-like ansatz, assuming that δf_N and $G^{(1)}_N$ have time and spatial dependence as

$$\delta f_N(\mathbf{x}, \mathbf{v}) = \delta f(\mathbf{k}, \mathbf{v}, z) z^N e^{i\mathbf{k}\cdot\mathbf{x}} \qquad G^{(1)}_N(\mathbf{x}, \mathbf{v}) = G^{(1)}(\mathbf{k}, \mathbf{v}, z) z^N e^{i\mathbf{k}\cdot\mathbf{x}}.$$

Here z is the amplification factor and can be written in the more familiar form $z = e^{-i\omega\Delta t}$ for a complex frequency ω. Putting the ansatz into Eq.(6.17) and using the definition of $G^{(1)}$, we obtain

$$\delta f(\mathbf{k}, \mathbf{v}, z) = \frac{e}{m_i} \left[\frac{\Delta t}{1 - z e^{i\mathbf{k}\cdot\mathbf{v}\Delta t}} - \alpha \Delta t \right] \mathbf{E}^{(1)}(\mathbf{k}, z) \cdot \nabla_{\mathbf{v}} f_0(\mathbf{v}). \tag{6.18}$$

Finally, an integration over velocity provides an expression for the linear perturbed number density

$$\delta n^{(1)}(\mathbf{k}, z) = \frac{e}{m_i} \mathbf{E}^{(1)}(\mathbf{k}, z) \cdot \int \left[\frac{\Delta t}{1 - z e^{i\mathbf{k}\cdot\mathbf{v}\Delta t}} \right] \nabla_{\mathbf{v}} f_0(\mathbf{v}) d\mathbf{v}, \tag{6.19}$$

which will be used in the spatial grid analysis and coupled to our field model in the following section.

It is interesting to note that for sufficiently well behaved f_0, the $\alpha\Delta t$ term in Eq.(6.18) does not contribute to the integral. The perturbed number density, Eq.(6.19), and therefore the modified dispersion relation will be independent of the time centering parameter α. In this work, the model is electrostatic, therefore only δn is needed in the field equation. If higher velocity moments are needed, for example in an electromagnetic model, α is expected to have important effects on the numerical properties of the PIC model. Multiplying Eq.(6.18) by $\mathbf{v}$ and integrating over velocity yields for the perturbed flux density

$$\delta n \mathbf{u}^{(1)}(\mathbf{k}, z) = \frac{e}{m_i} \int \mathbf{v} \left[\frac{\Delta t}{1 - z e^{i\mathbf{k}\cdot\mathbf{v}\Delta t}} \right] \mathbf{E}^{(1)}(\mathbf{k}, z) \cdot \nabla_{\mathbf{v}} f_0(\mathbf{v}) d\mathbf{v} + \alpha \Delta t \frac{e}{m_i} n_0 \mathbf{E}^{(1)}(\mathbf{k}, z),$$

showing that the α dependence does not necessarily vanish for velocity moments other than δn.

Continuing with our electrostatic model, for $f_0 = f_M$ in one dimension we have

$$\delta n^{(1)}(k, \omega) = \frac{ien_0}{2kT_i} E^{(1)}(k, \omega) X_{\delta f} \left(\frac{\omega}{\sqrt{2} k v_{th}}; \sqrt{2} k v_{th} \Delta t, 0 \right),$$

where $X_{\delta f}$ is defined by the complex integral

$$X_{\delta f}(\theta;\eta,\mu) = \frac{1}{\sqrt{\pi}} \int_{-\infty}^{\infty} \left[\frac{i\eta}{e^{i\eta[s(1-\mu)-\theta]} - 1} \right] \frac{d}{ds} e^{-s^2} ds, \qquad \text{Im } \theta > 0 \tag{6.20}$$

and its analytic continuation for Im $\theta \leq 0$. It is assumed that the arguments η and μ are real. Note that $X_{\delta f}(\theta;\eta,0) \to Z'(\theta)$ as $\eta \to 0$, giving the result obtained from Vlasov theory Eq.(6.14) as $\Delta t \to 0$.

6.3.2 Time Integration Analysis for the Full-f Method

Next, we will perform Langdon's time integration analysis for the implicit scheme applied to the full-f method. We will use this for making comparisons with the δf method and refer the reader to [82] for details of how the analysis is performed. The time integration scheme applied to the full-f method yields for the linear perturbed particle orbits

$$\begin{aligned} \frac{\mathbf{x}_\nu^{(1)} - \mathbf{x}_{\nu-1}^{(1)}}{\Delta t} &= (1-\alpha)\mathbf{v}_{\nu-1}^{(1)} + \alpha \mathbf{v}_\nu^{(1)} \\ \frac{\mathbf{v}_\nu^{(1)} - \mathbf{v}_{\nu-1}^{(1)}}{\Delta t} &= (1-\alpha)\frac{e}{m_i}\mathbf{E}_{\nu-1}^{(1)}(\mathbf{x}_{\nu-1}^{(0)}) + \alpha \frac{e}{m_i}\mathbf{E}_\nu^{(1)}(\mathbf{x}_\nu^{(0)}) \end{aligned}$$

The linear perturbed number density that results is

$$\delta n^{(1)}(\mathbf{k},z) = \frac{-ie}{m_i}\mathbf{E}^{(1)}(\mathbf{k},z)\cdot\mathbf{k} \int \left[\frac{\Delta t}{1 - ze^{i\mathbf{k}\cdot\mathbf{v}\Delta t}} - \alpha\Delta t \right]^2 f_0(\mathbf{v}) d\mathbf{v}. \tag{6.21}$$

For the one dimensional Maxwellian, this gives

$$\delta n^{(1)}(k,\omega) = \frac{ien_0}{2kT_i} E^{(1)}(k,\omega) X_f \left(\frac{\omega}{\sqrt{2}kv_{th}}; \sqrt{2}kv_{th}\Delta t, 0, \alpha \right),$$

where X_f is defined by the complex integral

$$X_f(\theta;\eta,\mu,\alpha) \equiv \frac{1}{\sqrt{\pi}}(1-\mu) \int_{-\infty}^{\infty} \left[\frac{i\eta}{e^{i\eta[s(1-\mu)-\theta]} - 1} + i\alpha\eta \right]^2 e^{-s^2} ds, \qquad \text{Im } \theta > 0 \tag{6.22}$$

and its analytic continuation for Im $\theta \leq 0$. It is assumed that the arguments η, μ and α are real. Again, we have that $X_f(\theta;\eta,0,\alpha) \to Z'(\theta)$ as $\eta \to 0$, yielding the result obtained from Vlasov theory Eq.(6.14).

6.4 Finite Time Step and Spatial Grid Dispersion Relations

In this section, we combine the time integration analyses for the δf and full-f methods with the spatial grid analysis in [83] to obtain modified dispersion relations for our model problem which include the effects of both Δt and Δx for a one dimensional periodic spatial grid. For the remainder of the chapter, we have $\mathbf{k} = k\hat{x}$ and integration over the y and z directions is assumed. We begin by summarizing the main ideas of the spatial grid analysis and discuss the appropriate transforms for simulations on a grid with period L_x.

6.4.1 Transforms for a Periodic Grid

For the analysis, we must consider both continuum and discrete quantities over the spatial domain and their Fourier representations. The Fourier representation of a continuum quantity $P(x)$ is to be interpreted as a Fourier series (FS) coefficient. The transform pair is given by

$$P(x) = \frac{1}{L_x} \sum_k P(k) e^{ikx} \tag{6.23}$$

$$P(k) = \int_0^{L_x} P(x) e^{-ikx} dx, \tag{6.24}$$

where the sum in Eq.(6.23) is over an infinite number of allowed values of k. The allowed values for a FS are $k = 2\pi m/L_x$ for each $m \in \mathbb{Z}$. In our model, the continuum quantities include the linear perturbed number density of point particles $\delta n^{(1)}(x)$, the electric field interpolated to the particle locations $E^{(1)}(x)$, and the shape function $S(x)$.

A discrete quantity G_j, which is defined on the grid points, has a discrete Fourier transform (DFT). The transform pair is given by

$$G_j = \frac{1}{L_x} \sum_k G(k) e^{ikX_j} \tag{6.25}$$

$$G(k) = \sum_{j=0}^{N_x - 1} G_j e^{-ikX_j} \Delta x, \tag{6.26}$$

where N_x is the number of grid points and the sum in Eq.(6.25) is over a finite number of allowed values of k. The allowed values of k in a DFT are $k = 2\pi m/L_x$ for each $m \in \{-N_x/2+1, -N_x/2+$

$2, ..., 0, 1, ...N_x/2\}$. The discrete quantities in our model include the perturbed number density of finite sized particles sampled on grid point, denoted $\tilde{\delta n}_j$, and the electric field defined on the grid points $\tilde{E}_j$.

6.4.2 The Shape Function

The shape function $S_{\mathbf{x}}$, which in one dimension we take as $S_{\mathbf{x}} = S(x/\Delta x)$, is used to interpolate between discrete and continuum quantities in the simulation model. To perform the spatial grid analysis, we relate the Fourier representations of $\tilde{\delta n}$ to $\delta n^{(1)}$ and $E^{(1)}$ to $\tilde{E}$. As in [83], we have

$$\tilde{\delta n}(k) = \sum_q S(k_q \Delta x) \delta n^{(1)}(k_q), \tag{6.27}$$

where $k_q = k - 2\pi q/\Delta x$ with the summation over all $q \in \mathbb{Z}$. The presence of $S(k\Delta x)$ accounts for the finite size of the computational particles, and the summation over spatial aliases accounts for the discrete sampling on the grid points. For the electric field, we have

$$E^{(1)}(k) = S(-k\Delta x)\tilde{E}(k), \tag{6.28}$$

where the presence of $S(k\Delta x)$ accounts for the interpolation to the locations of the particles.

The shape function is typically taken to be a B-Spline function. For illustration, we consider a linear B-Spline for our model given explicitly by

$$S(x) = \begin{cases} 1 - |x| & : |x| \leq 1 \\ 0 & : |x| > 1. \end{cases}$$

The FS coefficients of S are given by

$$S(k\Delta x) = \mathrm{dif}^2\left(\frac{k\Delta x}{2}\right), \qquad \mathrm{dif}(\theta) \equiv \frac{\sin\theta}{\theta} \tag{6.29}$$

for each allowed value of k.

6.4.3 Modified Dispersion Relations

We now use the spatial grid analysis outlined above to derive modified dispersion relations for the δf and full-f methods to include the effects of Δt and Δx. We first illustrate the technique

with the δf method and then simply present the result for the full-f method. Beginning with Eq.(6.19), we plug into Eq.(6.27) and replace $E^{(1)}$ with $\tilde{E}$ using Eq.(6.28). Since $\tilde{E}$ is periodic in Fourier space, it can be pulled out of the summation, yielding

$$\tilde{\delta n}(k,z) = \frac{e}{m_i}\tilde{E}(k,z)\sum_{q=-\infty}^{\infty} S(k_q\Delta x)S(-k_q\Delta x)\int_{-\infty}^{\infty}\left[\frac{\Delta t}{1-ze^{ik_q v\Delta t}}\right]\frac{\partial f_0}{\partial v}dv. \tag{6.30}$$

Next, we use a discrete version of our field model, Eq.(6.13), to relate $\tilde{\delta n}$ and $\tilde{E}$. We consider a discrete spatial model in which derivatives are taken spectrally, so the DFT version of Eq.(6.13) is simply

$$\tilde{E}(k,z) = -ik\frac{T_e}{en_0}\tilde{\delta n}(k,z). \tag{6.31}$$

In this case, the spatial derivative corresponds to a multiplication by ik in the DFT. If another method is used to compute the spatial derivative, this would need to be accounted for in the analysis. For example, a spatial derivative calculated from a centered finite difference scheme would correspond to a multiplication by $ik\mathrm{dif}(k\Delta x)$ in the DFT [83].

Using Eq.(6.29), Eq.(6.30), and Eq.(6.31), we arrive at the modified dispersion relation for the δf method

$$\epsilon_{\delta f}(k,z) \equiv 1 + \frac{kT_e}{m_i n_0}\sum_{q=-\infty}^{\infty}\mathrm{dif}^4\left(\frac{k_q\Delta x}{2}\right)\int_{-\infty}^{\infty}\left[\frac{i\Delta t}{1-ze^{ik_q v\Delta t}}\right]\frac{\partial f_0}{\partial v}dv = 0, \tag{6.32}$$

which for $f_0 = f_M$ gives

$$\epsilon_{\delta f}(\zeta) = 1 - \frac{1}{2T}\sum_{q=-\infty}^{\infty}\mathrm{dif}^4\left(\frac{k_q\Delta x}{2}\right)X_{\delta f}\left(\frac{\zeta}{\sqrt{2}};\sqrt{2}kv_{th}\Delta t,\frac{2\pi q}{k\Delta x}\right) = 0. \tag{6.33}$$

with T and ζ defined as in Eq.(6.14). Repeating the above process using the full-f linear perturbed number density, Eq.(6.21), gives the modified dispersion relation

$$\epsilon_f(k,z) \equiv 1 + \frac{kT_e}{m_i n_0}\sum_{q=-\infty}^{\infty}\mathrm{dif}^4\left(\frac{k_q\Delta x}{2}\right)k_q\int_{-\infty}^{\infty}\left[\frac{\Delta t}{1-ze^{ik_q v\Delta t}} - \alpha\Delta t\right]^2 f_0 dv = 0, \tag{6.34}$$

which for $f_0 = f_M$ gives

$$\epsilon_f(\zeta) = 1 - \frac{1}{2T}\sum_{q=-\infty}^{\infty}\mathrm{dif}^4\left(\frac{k_q\Delta x}{2}\right)X_f\left(\frac{\zeta}{\sqrt{2}};\sqrt{2}kv_{th}\Delta t,\frac{2\pi q}{k\Delta x},\alpha\right) = 0. \tag{6.35}$$

6.5 Analysis of the Modified Dispersion Relations

In this section, we analyze the modified dispersion relations Eqs.(6.32)–(6.35) to obtain results regarding the numerical accuracy and stability of the δf and full-f PIC methods. We study the accuracy of the real frequency and damping rate using a perturbation method applied to the dispersion relations with Maxwellian equilibrium distributions Eq.(6.33) and Eq.(6.35). The stability of the methods is examined analytically for a cold ion plasma and numerically for a finite temperature Maxwellian plasma.

6.5.1 Dispersion Accuracy

To study the accuracy of the real frequency and damping rate in a Maxwellian plasma for our PIC methods, we compare the scaled phase velocities ζ obtained from Eq.(6.33) or Eq.(6.35) to the Vlasov result ζ_0 obtained from Eq.(6.14). We assume that ζ has a regular double perturbation series in the small parameters $\epsilon_1 = kv_{th}\Delta t$ and $\epsilon_2 = k\Delta x$ given as

$$\zeta = \zeta_0 + \epsilon_1\zeta_{(1,0)} + \epsilon_2\zeta_{(0,1)} + \epsilon_1^2\zeta_{(2,0)} + \epsilon_1\epsilon_2\zeta_{(1,1)} + \epsilon_2^2\zeta_{(0,2)} + ...$$

This form can be plugged into Eq.(6.33) or Eq.(6.35). The modified dispersion relation is then expanded in a double Taylor series in ϵ_1 and ϵ_2 and powers of $\epsilon_1^n\epsilon_2^m$ are collected. Performing this procedure with Eq.(6.33) yields for the δf method $\zeta_{(1,0)} = \zeta_{(0,1)} = \zeta_{(1,1)} = 0$, giving second order correction terms of

$$\zeta - \zeta_0 \sim \frac{\sqrt{2}}{6Z''(\zeta_0/\sqrt{2})}\left[2T(k\Delta x)^2 - (kv_{th}\Delta t)^2\right]. \tag{6.36}$$

We note that the Vlasov theory yields a non-dispersive ion acoustic wave, but numerical dispersion is introduced in the discrete model from Δt and Δx. An examination of the signs of the real and imaginary parts for the terms on the right hand side shows the finite time step will act to increase the frequency and weaken the damping. The finite spatial step will have the opposite effect. Taking the ratio $v_{th}\Delta t/\Delta x = \sqrt{2T}$ will balance the effects and result in a higher order of accuracy.

We validate the expression Eq.(6.36) by performing linear δf simulations varying the size of $kv_{th}\Delta t$ for a fixed value of $k\Delta x = \pi/8$. The relative difference in the real frequency, $\omega_R = \mathrm{Re}(\omega)$,

and damping rate, $\gamma = \mathrm{Im}(\omega)$, between the values predicted in the Vlasov theory and those produced in simulations are measured and plotted in Figure 6.1. In the simulations, we choose $T = 0.1$ which provides a low damping rate, so measurements can be made accurately. A large number of computational particles ($N_p = 2097152$) are used to make the errors due to the finite number of particles small compared to the error due to $\Delta t \neq 0$ and $\Delta x \neq 0$. To further reduce errors associated with discrete particle effects, we use the Hammersley set (bit-reversed numbers) [32] [86] in the particle loading process. This allows us to simulate Landau-damped ion acoustic modes for long periods of time and obtain accurate measurements of ω_R and γ. The simulation error results are in excellent agreement with the error predicted from numerically solving Eq.(6.33) and taking the difference with the solution of Eq.(6.14). We refer to this difference as the theoretical numerical error. The asymptotic result Eq.(6.36) is also shown to be valid for small $kv_{th}\Delta t$. Finally, the simulation results also confirm that the numerical dispersion is independent of α for the δf method.

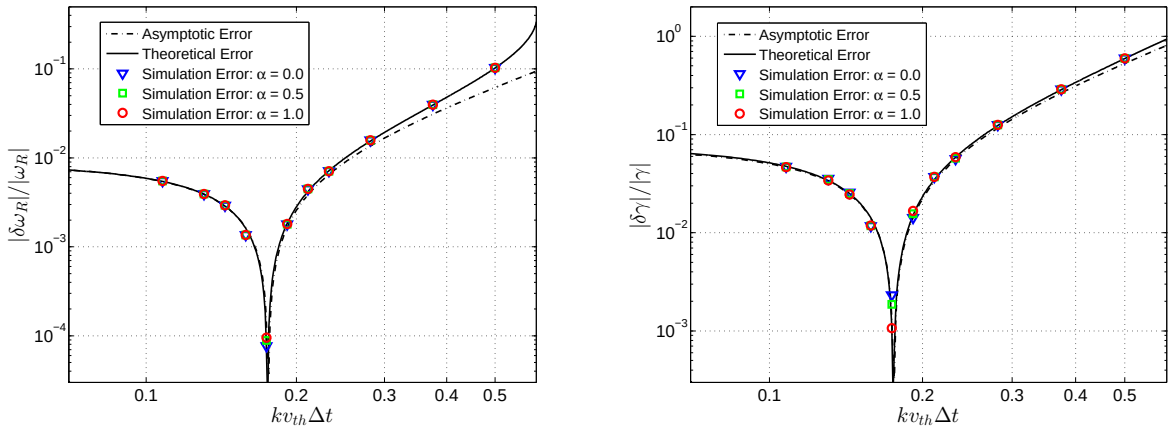

(a) Relative error in real frequency

(b) Relative error in damping rate

Figure 6.1: Simulation results varying the size of $kv_{th}\Delta t$ for the δf method are compared with the theoretical numerical error and the asymptotic error for values of $\alpha = 0, 1/2$, and 1. It can be seen that errors decrease rapidly near the region where $v_{th}\Delta t/\Delta x = \sqrt{2T}$. As $kv_{th}\Delta t$ continues to decrease past this region, the error is due to finite $k\Delta x$.

Repeating this analysis for the full-f method using Eq.(6.35), we find the correction to ζ at

the lowest order to be

$$\zeta - \zeta_0 \sim \frac{\sqrt{2}}{6Z''(\zeta_0/\sqrt{2})}\left[\frac{12i(2\alpha-1)}{\zeta_0}(T+1)(kv_{th}\Delta t) + 2T(k\Delta x)^2\right] \tag{6.37}$$

showing the method to produce results which are first order accurate in time for all α except $\alpha = 1/2$. The effect of Δx is again to lower the frequency and strengthen the damping. The effect of Δt is more difficult to analyze directly from Eq.(6.37) and is dependent on both T and α. For $\alpha = 1/2$, the full-f method will produce results which are second order accurate in time. The correction to ζ is then given by

$$\zeta - \zeta_0 \sim \frac{\sqrt{2}}{3Z''(\zeta_0/\sqrt{2})}\left[(kv_{th}\Delta t)^2 + T(k\Delta x)^2\right]. \tag{6.38}$$

Again, we compare the results of Eq.(6.37) and Eq.(6.38) with simulations varying the size of $kv_{th}\Delta t$. The same values for N_p and $k\Delta x$ are used as with the δf method. These results are presented in Figure 6.2. Finally, we test the convergence of the δf and full-f methods in $k\Delta x$,

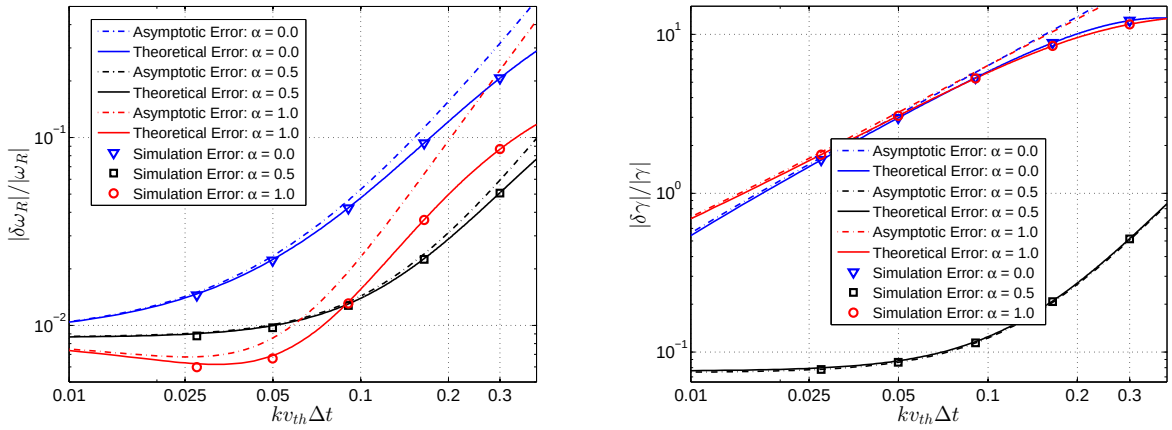

(a) Relative error in real frequency

(b) Relative error in damping rate

Figure 6.2: Simulation results varying the size of $kv_{th}\Delta t$ for the full-f method are compared with the theoretical numerical error and the asymptotic error, including second order terms, for values of $\alpha = 0, 1/2$, and 1.

fixing $kv_{th}\Delta t = 0.075$ and $\alpha = 1/2$. The results are presented in Figure 6.3.

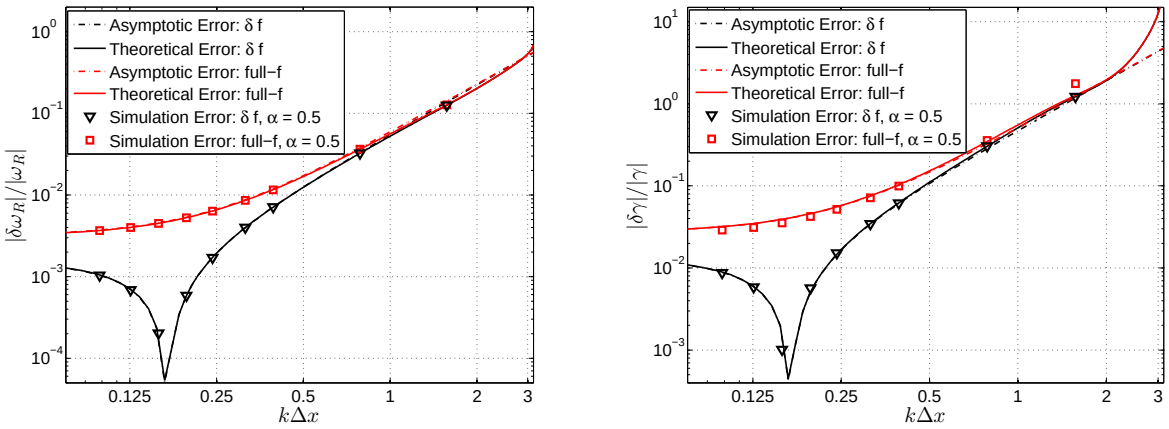

(a) Relative error in real frequency

(b) Relative error in damping rate

Figure 6.3: Simulation results varying the size of $k\Delta x$ for both the δf and full-f methods are compared with the theoretical numerical error and the asymptotic error.

6.5.2 Numerical Stability Analysis for Cold Ions

Next, we consider how the full-f and δf PIC methods behave in the cold ion limit, which allows for a straight-forward analysis of the modified dispersion relations. In the next section, we will examine the stability properties with increasing ion temperature. For the cold ion stability analysis, we begin with the δf method, choosing $f_0(v) = n_0\delta(v)$ in Eq.(6.32). With this choice, the velocity integration and the summation can be performed exactly, and we are left with a quadratic equation for the amplification factor z given by

$$(1-z)^2 + z(kc_s\Delta t)^2 \mathrm{dif}\left(\frac{k\Delta x}{2}\right)\cos\left(\frac{k\Delta x}{2}\right) = 0, \tag{6.39}$$

where $c_s \equiv \sqrt{T_e/m_i}$ is the ion sound speed. The solution to Eq.(6.39) gives stability restrictions on $k\Delta x$ and $kc_s\Delta t$ from the requirement that $|z| \leq 1$. The region in this parameter space that will produce stable solutions is shown in Figure 6.4. A simple condition to ensure stability at any wave number can be given by

$$c_s\frac{\Delta t}{\Delta x} \leq 1.483,$$

which is obtained by finding the maximum possible slope of a line segment through parameter space connecting the points $(0,0)$ and $(\pi, kc_s\Delta t)$ and contained entirely in the region of linear

stability. This is in a form similar to a Courant-Friedrichs-Lewy (CFL) condition [87], which is not typically observed when using implicit time integration schemes. For the full-f method, choosing

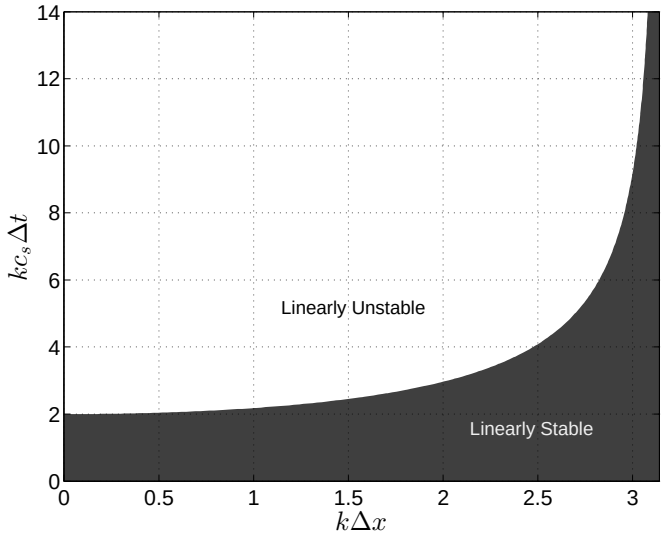

Figure 6.4: The cold ion stability region for the δf method is plotted. The shaded area represents regions in the parameter space $(k\Delta x, kc_s\Delta t)$ which will result in stable simulations.

$f_0(v) = n_0\delta(v)$ in Eq.(6.34) gives the following equation for the amplification factor

$$(1-z)^2 + (1-\alpha+\alpha z)^2(kc_s\Delta t)^2 \mathrm{dif}\left(\frac{k\Delta x}{2}\right)\cos\left(\frac{k\Delta x}{2}\right) = 0.$$

Solving this equation gives for the square modulus of either root

$$|z|^2 = \frac{k\Delta x + (kc_s\Delta t)^2(1-\alpha)^2\sin(k\Delta x)}{k\Delta x + (kc_s\Delta t)^2\alpha^2\sin(k\Delta x)},$$

which is greater than unity when $\alpha < 1/2$ and less than unity when $\alpha > 1/2$, independent of $kc_s\Delta t$ and $k\Delta x$. Hence the cold ion stability of the full-f method is determined by the implicitness of the scheme, as is usually expected, and no CFL condition is present.

6.5.3 Numerical Stability Analysis for Warm Ions

A stability analysis for the warm Maxwellian equilibrium distribution is more difficult, requiring the numerical solutions of Eq.(6.33) and Eq.(6.35). A discussion on the numerical solution of

integrals of similar form to Eq.(6.20) and Eq.(6.22) can be found in the appendix of [82]. A search for the boundary of the stability region is performed by numerically solving the dispersion relations over a region of the parameter space $(k\Delta x, kv_{th}\Delta t)$ and determining the contours for which $|z| = 1$. Stability conditions of the form

$$r \equiv v_{th}\frac{\Delta t}{\Delta x} \leq C_{max}$$

are then determined from the stability region boundaries to ensure stability at all present wave numbers. Here, C_{max} is the Courant number [87], which depends on T for warm ions.

6.5.3.1 Warm Ion Stability for the δf Method

The stability region boundaries for the δf method are shown in Figure 6.5 for various values of T. It is observed that the δf method shows better stability as T is increased. The unstable regions become smaller for higher temperatures and vanish altogether for temperatures above a critical value between $T = 0.6$ and $T = 0.7$. Courant numbers are given in Table 6.1 for the

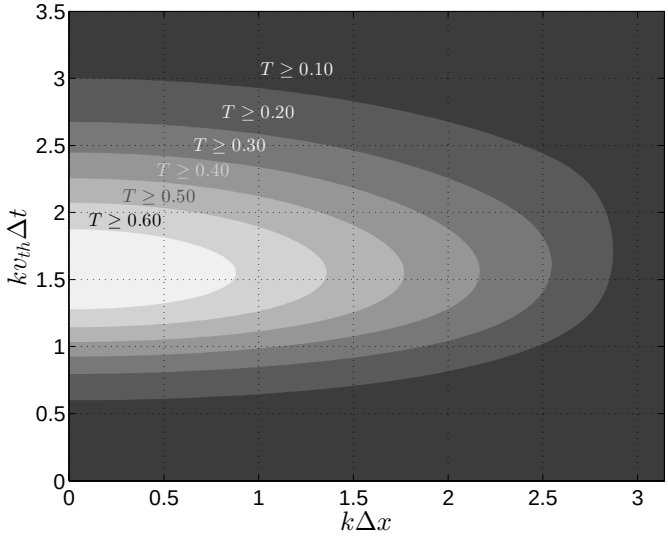

Figure 6.5: Stability regions for the δf method are plotted for various values of T. The different shaded areas represent regions in the parameter space $(k\Delta x, kv_{th}\Delta t)$ which will result in stable simulations for T above the indicated value.

different values of T, along with the first mode to become unstable as r is increased past C_{max}.

Finally, a predicted instability for $T = 0.3$ is demonstrated by performing the simulations shown in Figures 6.6 and 6.7. The initial conditions are taken such that each non-zero wave number in the DFT begins with a finite perturbation, as discussed in Appendix D. The simulation in Figure 6.6 is observed to be stable at all wave numbers with $r = 0.62$. In Figure 6.7, $r = 0.66$ and the modes near $k\Delta x = 1.96$ are shown to exhibit exponential growth. This is in agreement with the predicted instability for $r > 0.64$. It is observed from the numerical solution of Eq.(6.33) and simulations that $\omega_R \Delta t = \pi$ at the onset of the instability in the δf method. This is thought to be due to inadequate temporal resolution of the ion acoustic wave for the first unstable DFT wave number, since the physical wave from Eq.(6.14) has a real frequency exceeding $\pi/\Delta t$.

T	C_{max}	$k\Delta x$
0.10	0.40	2.27
0.20	0.51	2.19
0.30	0.64	1.96
0.40	0.82	1.66
0.50	1.09	1.31
0.60	1.73	0.87
0.70	∞	-

Table 6.1: Courant numbers (C_{max}) are given for warm δf ions for various values of T, along with the first discrete mode to become unstable ($k\Delta x$) as r is increased past C_{max}.

6.5.3.2 Warm Ion Stability for the Full-f Method

For the full-f method, it is observed that unconditional stability is maintained for $\alpha \geq 0.5$ as temperature is increased. For $\alpha < 0.5$, simulations are no longer unconditionally unstable, but instead develop stability regions in $(k\Delta x, kv_{th}\Delta t)$ space. Again stability is improved as T is increased, and for fixed values of $\alpha < 0.5$, there are critical temperatures for which the unstable regions vanish making the method unconditionally stable. An example of the finite temperature stability regions is shown in Figure 6.8 for $\alpha = 0.250$. The critical temperature occurs between $T = 0.18$ and $T = 0.20$. Courant numbers are given in Table 6.2 for $\alpha = 0.125, 0.250$, and 0.375 at different values of T. Finally, a predicted instability for $\alpha = 0.250$ at $T = 0.14$ is demonstrated by

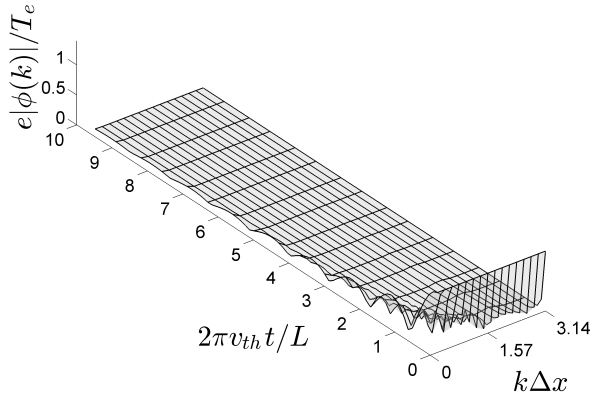

(a) Time history of DFT modes of $e\phi/T_e$

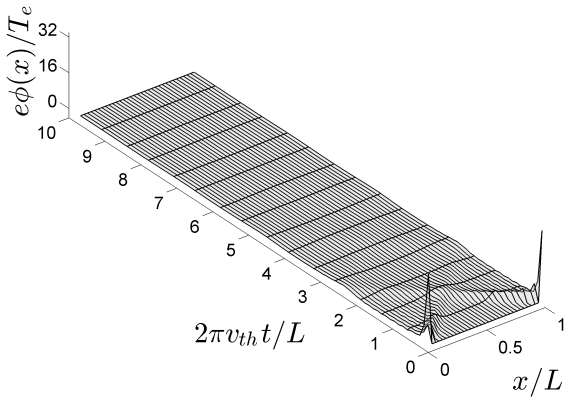

(b) Time history of $e\phi/T_e$ in real space

Figure 6.6: δf simulation for $T = 0.3$ and $r = 0.62$. The initial condition is taken to give a finite perturbation to each non-zero wave number in the DFT. The simulation is stable at all wave numbers, in agreement with the theory which predicts stability for $r < 0.64$.

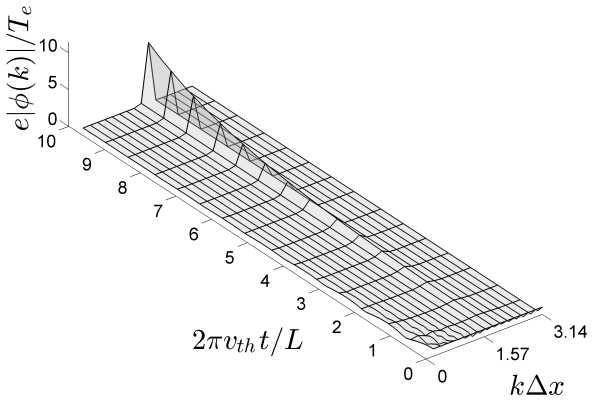

Figure 6.7: δf simulation for $T = 0.3$ and $r = 0.66$. The time history of the DFT modes is shown with the initial condition taken to give a finite perturbation to each non-zero wave number in the DFT. Exponential growth of the modes near $k\Delta x = 1.96$ is observed for $r = 0.66$, in agreement with the predicted instability for $r > 0.64$.

performing the simulations shown in Figures 6.9 and 6.10. The initial conditions are again taken to excite each non-zero wave number in the DFT with a finite perturbation. The simulation in Figure 6.9 is observed to be stable for $r = 0.16$. In Figure 6.10, $r = 0.24$ and the modes near $k\Delta x = 0.91$ are shown to grow with time. This is in agreement with the predicted instability for $r > 0.20$. It is

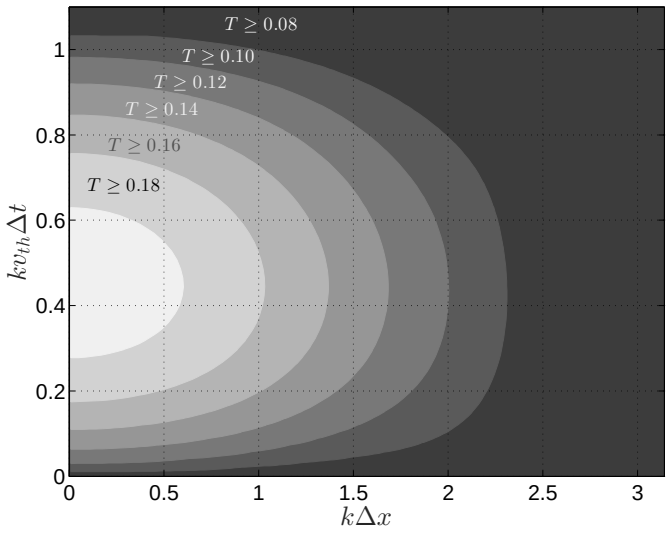

Figure 6.8: Stability regions for the full-f method with $\alpha = 0.25$ are plotted for various values of T. The different shaded areas represent regions in the parameter space $(k\Delta x, kv_{th}\Delta t)$ which will result in stable simulations for T above the indicated value.

observed that the instabilities for the full-f method occur for values $\omega_R \Delta t < \pi$. The physical wave from Eq.(6.14) can be resolved on the time "grid" for the first unstable DFT wave number in this case, having a real frequency less than $\pi/\Delta t$.

$\alpha = 0.125$

T	C_{max}	$k\Delta x$
0.08	0.02	0.85
0.10	0.04	0.92
0.12	0.07	0.97
0.14	0.12	0.98
0.16	0.19	0.95
0.18	0.28	0.88
0.20	0.45	0.74
0.22	1.05	0.40
0.24	∞	-

$\alpha = 0.250$

T	C_{max}	$k\Delta x$
0.08	0.02	0.84
0.10	0.06	0.91
0.12	0.11	0.94
0.14	0.20	0.91
0.16	0.33	0.82
0.18	0.68	0.56
0.20	∞	-
0.22	∞	-
0.24	∞	-

$\alpha = 0.375$

T	C_{max}	$k\Delta x$
0.08	0.05	0.83
0.10	0.13	0.86
0.12	0.28	0.77
0.14	1.48	0.25
0.16	∞	-
0.18	∞	-
0.20	∞	-
0.22	∞	-
0.24	∞	-

Table 6.2: Courant numbers (C_{max}) are given for warm full-f ions for various values of T and $\alpha < 1/2$, along with the first discrete mode to become unstable ($k\Delta x$) as r is increased past C_{max}.

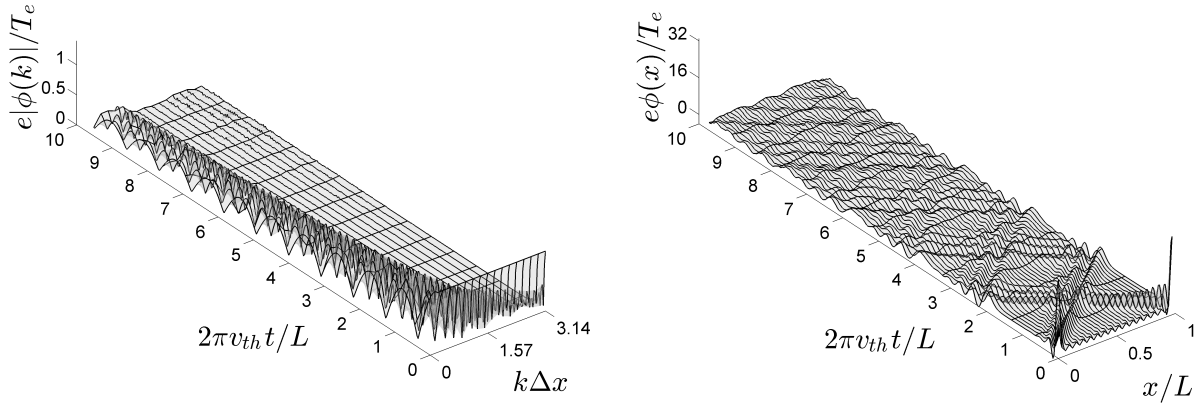

(a) Time history of DFT modes of $e\phi/T_e$

(b) Time history of $e\phi/T_e$ in real space

Figure 6.9: Full-f simulation for $T = 0.14$, $\alpha = 0.25$, and $r = 0.16$. The initial condition is taken to give a finite perturbation to each non-zero wave number in the DFT. The simulation is stable at all wave numbers, in agreement with the theory which predicts stability for $r < 0.20$.

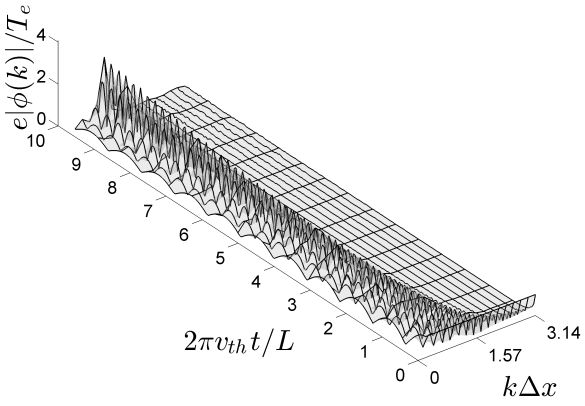

Figure 6.10: Full-f simulation for $T = 0.14$, $\alpha = 0.25$, and $r = 0.24$. The time history of the DFT modes is shown with the initial condition taken to give a finite perturbation to each non-zero wave number in the DFT. Exponential growth of the modes near $k\Delta x = 0.91$ is observed for $r = 0.24$, in agreement with the predicted instability for $r > 0.20$.

6.6 Summary

In this chapter, we have developed a theoretical framework for analyzing implicit and explicit time integration schemes applied to δf method PIC models. This work is easily combined with the

spatial grid analysis of Langdon to provide modified dispersion relations to include the numerical effects of both Δt and Δx. The analysis is illustrated for the adjustable time centering implicit scheme [15]. A significant challenge is to analyze the resulting modified dispersion relations that include finite Δt and Δx. We used a perturbative method to obtain lowest order corrections to the real frequency and damping rate due to Δt and Δx. This provides a theory for the accuracy of the simulations and can also provide some insights on the stability of various δf schemes. Further exploring the issue of numerical stability, we find that a CFL condition exists in the δf method PIC model at low ion temperatures, independent of the parameter α, which characterizes the implicitness of the scheme. We note that this unusual behavior occurs only for implicit δf PIC with low temperature ions. Full-f PIC does not exhibit this behavior and can be made unconditionally stable with sufficient implicitness. For cold ions, this condition can become restrictive for increasing grid resolution. The CFL condition for this particular model illustrates an unusual issue that may be encountered when using the δf method. In particular, it is possible for implicit schemes to provide no additional stability.

Chapter 7

Summary and Discussion

In this thesis, we have advanced the development of fully kinetic (FK) ion models, based on evolving the full form of the Newton-Lorentz equations of motion, to be used for low-frequency magnetized plasma simulations. Such models offer formal simplicity over higher order gyrokinetic (GK) models and can provide an important validation tool or replacement for GK ion models in regimes where the GK ordering assumptions may be in question. The new work presented in this thesis begins with analytical studies performed for a slab ion temperature gradient (ITG) instability model, comparing the use of FK ions and GK ions. Dispersion relations were derived for each model. The dispersion relation for the FK ion model was shown to reduce to the dispersion relation for the GK ion model under the GK ordering assumptions. This gives us confidence that the same low frequency normal modes are captured in both models; hence, the FK ion model is appropriate to be used in comparison studies with gyrokinetics.

In addition to the low frequency normal modes, the FK ion slab ITG model allows for the propagation of ion Bernstein modes at frequencies near the harmonics of the ion gyro-frequency. These high frequency, undamped modes are a potential source of difficulty in the numerical simulations using the FK ion model. This was the case when we focused on the simulation of ion Landau damped ion acoustic waves, taking a spatially homogeneous equilibrium distribution. Large amplitude ion Bernstein modes were present in the simulations, obscuring the low frequency physics when FLR effects were included. This motivated the study of the FK ion acoustic wave model as an initial value problem using the Laplace transform method in order to obtain information about the

relative amplitudes of the normal modes in the continuous model. The theory derived was found to accurately predict the amplitudes of each normal mode in the simulation, indicating that the large Bernstein modes were consistent with the model and not spurious numerical effects. Nevertheless, for comparison purposes it is desirable to be able to isolate the low frequency fluctuations in the simulations. Towards this goal, an implicit orbit averaging/sub-cycling algorithm was explored in which the particle system and field equations are advanced with separate time step sizes. The orbit averaging/sub-cycling algorithm was shown to accurately produce FLR effects for the low frequency ion acoustic wave while reducing the undesirable effects of the high frequency ion Bernstein modes. In addition, a reformulation of the implicit electrostatic field model was found to introduce numerical damping of the high frequencies. The use of GPUs with the orbit averaging/sub-cycling algorithm was also explored in this work and a speedup factor of ~ 48 was achieved compared to an equivalent serial CPU implementation. The use of GPUs therefore holds promise for handling the more expensive particle integration associated with the FK ion model.

An extension to the slab ITG model was developed in this thesis for including equilibrium gradients for a plasma in a weakly inhomogeneous background magnetic field. This extended model was then implemented to simulate the toroidal ITG instability with FK ions for the first time. Key to this work was the development of a particle integration scheme based on variational principles. The integration scheme was shown to produce accurate particle orbits in a toroidal magnetic field for long simulation times. In addition, the integrator was shown to accurately conserve constants of motion. The FK toroidal ITG implementation was benchmarked with the global GEM gyrokinetic code and good agreement was observed for the real frequencies and damping rates, giving us confidence in our implementation. Future directions for this work include the implementation of nonlinear terms, electromagnetic effects, and kinetic electrons.

Finally, in the course of this work on FK ion models, we have developed for the first time a comprehensive method for evaluating the effects introduced by the discretization schemes applied to the δf particle-in-cell method. Using this method, a complete numerical analysis was performed of an implicit integration scheme applied to the ion acoustic wave model. A full-f particle-in-

cell method applied to the same model was analyzed as well for comparison purposes using the methods of Langdon [82, 83]. It was demonstrated that the two methods can exhibit very different numerical properties even when similar integration schemes are applied. An interesting property of the implicit scheme applied to the δf method was also revealed by this analysis. When only the perturbed number density is present in the field equations, the implicitness of the scheme offers no additional stability. This effect was confirmed with simulations and was the motivation for reformulating the field model to include a perturbed flux density for the orbit averaging/sub-cycling scheme.

Bibliography

[1] F. Reif. Fundamentals of Statistical and Thermal Physics. McGraw-Hill, 1965.

[2] N. A. Krall and A. W. Trivelpiece. Principles of Plasma Physics. McGraw-Hill, 1973.

[3] S. Brunner. Global Approach to the Spectral Problem of Microinstabilities in Tokamak Plasmas Using a Gyrokinetic Model. PhD thesis, École Polytechnique Fédérale de Lausanne, 1997.

[4] W. Horton. Rev. Mod. Phys., 71:735, 1999.

[5] M. A. Beer. Gyrofluid Models of Turbulent Transport in Tokamaks. PhD thesis, Princeton University, 1995.

[6] E. A. Frieman and L. Chen. Phys. Fluids, 25:502, 1982.

[7] P. H. Rutherford and E. A. Frieman. Phys. Fluids, 11:569, 1968.

[8] J. B. Taylor and Hastie R. J. Plasma Phys., 10:479, 1968.

[9] W. W. Lee. Phys. Fluids, 26:556, 1983.

[10] W. W. Lee. J. Comput. Phys., 72(1):243, 1987.

[11] T. S. Hahm, L. Wang, and J. Madsen. Phys. Plasmas, 16:022305, 2009.

[12] A. M. Dimits. Phys. Plasmas, 19:022504, 2012.

[13] M. Artun and W. M. Tang. Phys. Plasmas, 1:2682, 1994.

[14] A. J. Brizard. Phys. Plasmas, 2:459, 1995.

[15] J. Cheng, S. E. Parker, Y. Chen, and D. Uzdensky. J. Comput. Phys., 245:364, 2013.

[16] Y. Chen and S. E. Parker. Phys. Plasmas, 16:052305, 2009.

[17] D. D. Schnack, J. Cheng, D. C. Barnes, and S. E. Parker. Phys. Plasmas, 20:062106, 2013.

[18] X. Kong, M. Huang, C. Ren, and V. Decyk. J. Comput. Phys., 230:1676, 2011.

[19] V. K. Decyk and T. V. Singh. Comput. Phys. Comm., 182:641, 2011.

[20] G. Chen, L. Chacón, and D. C. Barnes. J. Comput. Phys., 231:5374, 2012.

[21] V. K. Decyk and T. V. Singh. Comput. Phys. Comm., 185:708, 2014.

[22] B. Sturdevant, S.E. Parker, Y. Chen, and B. Hause. J. Comput. Phys., 316:519, 2016.

[23] B. Sturdevant and S.E. Parker. J. Comput. Phys., 305:647, 2016.

[24] Chen F. Introduction to Plasma Physics and Controlled Fusion. Springer, 1984.

[25] R. J. Goldston and P. H. Rutherford. Introduction to Plasma Physics. Institute of Physics Publishing, 1995.

[26] R. Fitzpatrick. Plasma Physics. 2011.

[27] P. L. Sulem. Fields Institute Communications, 46:109, 2005.

[28] R. G. Littlejohn. J. Math. Phys., 20:2445, 1979.

[29] R. G. Littlejohn. Phys. Fluids, 24:1730, 1981.

[30] R. G. Littlejohn. J. Math. Phys., 23:742, 1982.

[31] A. I. Morozov and L. S. Solov'ev. Rev. of Plasma Phys., 2:201, 1966.

[32] C. K. Birdsall and A. B. Langdon. Plasma Physics via Computer Simulation. McGraw-Hill, 1985.

[33] J. M. Dawson. Rev. Mod. Phys., 55 No. 2:403, 1983.

[34] G. Lapenta. Particle In Cell Methods with Applications to Simulations in Space Weather. 2011.

[35] H. D. Victory and E. J. Allen. SIAM J. Numer. Anal., 28 (5):1207, 1991.

[36] K. Ganguly and H. D. Victory. SIAM J. Numer. Anal., 26:249, 1989.

[37] H. D. Victory, G. Tucker, and K. Ganguly. SIAM J. Numer. Anal., 28:955, 1991.

[38] S. E. Parker and W. W. Lee. Phys. Fluids B, 5:77, 1993.

[39] A. M. Dimits and W. W. Lee. J. Comput. Phys., 107:309, 1993.

[40] G. Hu and J. A. Krommes. Phys. Plasmas, 1:863, 1994.

[41] A. Y. Aydemir. Phys. Plasmas, 1:822, 1994.

[42] M. Kotschenreuther. Bull. Am. Phys. Soc., 34:2107, 1993.

[43] P. N. Guzdar, L. Chen, W. M. Tang, and P. H. Rutherford. Phys. Fluids, 26:673, 1983.

[44] I. Bernstein. Phys. Rev., 109:10, 1958.

[45] M. Abramowitz and I. Stegun. Handbook of Mathematical Functions. United States Department of Commerce, National Bureau of Standards, Washington D. C., 1964.

[46] B. D. Fried and S. D. Conte. The Plasma Dispersion Function. Academic Press, New York, 1961.

[47] W. Wan, S. E. Parker, Y. Chen, Z. Yan, R. J. Groebner, and P. B. Snyder. Phys. Rev. Lett., 109:185004, 2012.

[48] W. Wan, S. E. Parker, Y. Chen, R. J. Groebner, Z. Yan, A. Y. Pankin, and S. E. Kruger. Phys. Plasmas, 20:055902, 2013.

[49] Y. Chen, S. E. Parker, G. Rewoldt, S. Ku, G. Y. Park, and C-S. Chang. Phys. Plasmas, 15:055905, 2008.

[50] J. Chowdhury, Y. Chen, W. Wan, S. E. Parker, W. Guttenfelder, and J. M. Canik. Phys. Plasmas, 23:012513, 2016.

[51] J. P. M. Schmitt. Phys. Rev. Lett., 31 (16):982, 1973.

[52] J. P. Boris. Proc. Fourth Conf. Num. Sim. Plasmas. Naval Res. Lab., Wash., D.C., 1970.

[53] B. I. Cohen, R. P. Freis, and V. Thomas. J. Comput. Phys., 45:345, 1982.

[54] B. I. Cohen, T. A. Brengle, D. B. Conley, and R. P. Freis. J. Comput. Phys., 38:45, 1980.

[55] B. I. Cohen and R. P. Freis. J. Comput. Phys., 45:367, 1982.

[56] A. Friedman, S. E. Parker, S. L. Ray, and C. K. Birdsall. J. Comput. Phys., 96:54, 1991.

[57] S. E. Parker, A. Friedman, S. L. Ray, and C. K. Birdsall. J. Comput. Phys., 107:388, 1993.

[58] G. Chen, L. Chacón, and D. C. Barnes. J. Comput. Phys., 230:7018, 2011.

[59] L. Chacón, G. Chen, and D. C. Barnes. J. Comput. Phys., 233:1, 2013.

[60] C. T. Kelley. Iterative Methods for Linear and Nonlinear Equations. SIAM, 1995.

[61] S. Markidis and G. Lapenta. J. Comput. Phys., 230:7037, 2011.

[62] G. Chen, L. Chacón, C. A. Leibs, D. A. Knoll, and W. Taitano. J. Comput. Phys., 258:555, 2014.

[63] PGI. CUDA Fortran Programming Guide and Reference. Version 2015.

[64] L. I. Rudakov and R. Z. Sagdeev. Sov. Phys. Dokl., 6:415, 1961.

[65] B. Coppi, H. P. Rosenbluth, and R. Z. Sagdeev. Phys. Rev. Lett., 17:377, 1966.

[66] S. E. Parker, C. Kim, and Y. Chen. Phys. Plasmas, 6(5):1709, 1999.

[67] S. E. Parker, W. W. Lee, and R. Santoro. Phys. Rev. Lett., 71:2042, 1993.

[68] R. Sydora, V. Decyk, and J. Dawson. Plasma Phys. Controlled Fusion, 38:A281, 1996.

[69] S. E. Parker, H. Mynick, M. Artun, V. Decyk, J. Kepner, W. W. Lee, and W. Tang. Phys. Plasmas, 3:1959, 1996.

[70] A. M. Dimits and et al. Phys. Plasmas, 7(3):969, 2000.

[71] Y. Chen and S. E. Parker. J. Comput. Phys., 220:839–855, 2007.

[72] R. D. Hazeltine and J. D. Meiss. Plasma Confinement. Dover Publications, 2003.

[73] W. D'haeseleer, W. Hitchon, J. Callen, and J. Shohet. Flux Coordinates and Magnetic Field Structure. Springer-Verlag Berlin Heidelberg, 1991.

[74] G. E. P. Box and M. E. Muller. Ann. Math. Stat., 29, 2:610, 1958.

[75] G. Casella, C. Robert, and M. Wells. Institute of Mathematical Statistics Lecture Notes - Monograph Series, 45:342–347, 2004.

[76] R. L. Miller, J. M. Chu, Y. R. Greene, Lin-Lui, and R. E. Waltz. Phys. Plasmas, 5:973, 1999.

[77] J. E. Marsden and M. West. Acta Numerica, page 357, 2001.

[78] E. Hairer, C. Lubich, and G. Wanner. Geometric Numerical Integration. Springer-Verlag Berlin Heidelberg, 2002.

[79] M. West. Variational Integrators. PhD thesis, California Institute of Technology, 2004.

[80] M. Krauss. Variational Integrators in Plasma Physics. PhD thesis, Technishe Universitat Munchen, 2013.

[81] L. Verlet. Phys. Rev., 159:98, 1967.

[82] A. B. Langdon. J. Comput. Phys., 30:202, 1979.

[83] A. B. Langdon. J. Comput. Phys., 6:247, 1970.

[84] J. A. Byers. Proc. Fourth Conf. Num. Sim. Plasmas. Naval Res. Lab., Wash., D.C., 1970.

[85] K. E. Atkinson. An Introduction to Numerical Analysis. Wiley, second edition, 2004.

[86] J. M. Hammersley and D. C. Handscomb. Monte Carlo Methods. Methuen, 1964.

[87] R. Courant, K. Friedrichs, and H. Lewy. Mathematische Annalen, 100:32, 1928.

[88] D. A. Wunsch. Complex Variables with Applications, 3rd Edition. Pearson, 2005.

Appendix A

Justification for Contour Deformation in the Inverse Laplace Transform

The justification for the contour deformation used to obtain Eq.(4.10) follows from the analyticity of the functions F, G, and H defined by the sums

$$F(u;a,b) = \sum_{n=-\infty}^{\infty} Z(u+an)I_n(b)e^{-b}$$
$$G(u;a,b) = \sum_{n=-\infty}^{\infty} Z'(u+an)I_n(b)e^{-b}$$
$$H(u;a,b) = \sum_{n=-\infty}^{\infty} nZ(u+an)I_n(b)e^{-b},$$

where $u \in \mathbb{C}$, $a \in \mathbb{R}$, and $b \in \mathbb{R}_{>0}$, with

$$\mathbb{R}_{>0} = \left\{ x \in \mathbb{R} \middle| x > 0 \right\}.$$

In the series definitions, Z is the plasma dispersion function of Fried and Conte, which is analytic over the whole complex plane, and I_n is the n^{th} modified Bessel function of the first kind. To prove the analyticity of these functions, we begin with the following lemma.

Lemma A.1. *The plasma dispersion function is bounded by a function depending only on* $\mathrm{Im}(w)$ *as*

$$|Z(w)| \leq 2(1 + \sqrt{\pi}e^{\mathrm{Im}(w)^2})$$

for all $w \in \mathbb{C}$.

Proof. We begin with an integral definition for Z, which is valid for all complex arguments

$$Z(w) = 2ie^{-w^2} \int_{-\infty}^{iw} e^{-t^2} dt.$$

Setting $w = x + iy$ and taking the contour to be the straight path from $w = -\infty$ to $w = -y$ along the real axis, joined with the straight path from $w = -y$ to $w = -y + ix$ parallel to the imaginary axis, we have

$$Z(x+iy) = 2ie^{-(x+iy)^2}\left(\int_{-\infty}^{-y} e^{-s^2}ds + i\int_0^x e^{-(y-is)^2}ds\right).$$

From this expression, the following bound is readily obtained:

$$|Z(x+iy)| \leq 2\int_{-\infty}^{-y} e^{y^2-s^2}ds + 2\int_0^{|x|} e^{s^2-x^2}ds.$$

The first integral can be bounded by extending the upper limit of integration to $+\infty$. For the second integral, we have

$$\int_0^{|x|} e^{s^2-x^2}ds \leq \int_0^{|x|} e^{sx-x^2}ds = \frac{1-e^{-x^2}}{|x|}.$$

This function is bounded at $x = 0$, since $1 - e^{-x^2} \sim O(x^2)$. In addition, it remains bounded for all $x \in \mathbb{R}$, since

$$\frac{1-e^{-x^2}}{|x|} = \frac{\int_0^{|x|} 2te^{-t^2}dt}{|x|} \leq \sqrt{2}e^{-1/2} < 1.$$

The inequality then follows. □

Theorem A.1. *The series of analytic functions*

$$\sum_{n=-\infty}^{\infty} Z(u+an)I_n(b)e^{-b}$$

with $a \in \mathbb{R}$ and $b \in \mathbb{R}_{>0}$ is uniformly convergent over the domain in the complex plane defined by $D = \{u \in \mathbb{C} \big| -y_0 < \mathrm{Im}(u) < y_0\}$ for any $y_0 > 0$. Since uniform convergence of a series of analytic functions guarantees analyticity of the sum, the function F is an analytic function of u over D. Furthermore, the series of analytic functions

$$\sum_{n=-\infty}^{\infty} Z'(u+an)I_n(b)e^{-b}$$

also converges to an analytic function in D, which is equal to the derivative of F. Hence, G is an analytic function of u over D and $G = F'$.

Proof. The proof follows from Lemma A.1 and the Weierstrass M-test. Each term in the series is bounded as

$$|Z(u+an)I_n(b)e^{-b}| \leq 2(1+\sqrt{\pi}e^{\mathrm{Im}(u)^2})I_n(b)e^{-b} \leq 2(1+\sqrt{\pi}e^{y_0^2})I_n(b)e^{-b}$$

in D. Furthermore, the modified Bessel function series gives

$$\sum_{n=-\infty}^{\infty} 2(1+\sqrt{\pi}e^{y_0^2})I_n(b)e^{-b} = 2(1+\sqrt{\pi}e^{y_0^2}) < \infty.$$

The Weierstrass M-test therefore guarantees uniform convergence of the series. The analyticity of F in D follows directly from the uniform convergence of its series definition. Uniform convergence of the series also allows term by term differentiation to obtain a series which converges to the derivative of the sum in D. This follows from a standard theorem in complex analysis. See, for example, Chapter 5 of [88]. □

Theorem A.2. *The series of analytic functions*

$$\sum_{n=-\infty}^{\infty} nZ(u+an)I_n(b)e^{-b}$$

with $a \in \mathbb{R}$ and $b \in \mathbb{R}_{>0}$ is uniformly convergent over D. Since uniform convergence of a series of analytic functions guarantees analyticity of the sum, H is an analytic function of u over D.

Proof. The proof again follows from Lemma A.1 and the Weierstrass M-test. Each term in the series is bounded as

$$\begin{aligned}
|nZ(u+an)I_n(b)e^{-b}| &\leq 2(1+\sqrt{\pi}e^{\mathrm{Im}(u)^2})|nI_n(b)|e^{-b} \\
&\leq b(1+\sqrt{\pi}e^{\mathrm{Im}(u)^2})|I_{n-1}(b)-I_{n+1}(b)|e^{-b} \\
&\leq b(1+\sqrt{\pi}e^{\mathrm{Im}(u)^2})\left(I_{n-1}(b)+I_{n+1}(b)\right)e^{-b}.
\end{aligned}$$

in D. The second inequality follows from the identity

$$\frac{2n}{b}I_n(b) = I_{n-1}(b) - I_{n+1}(b),$$

and the third inequality is an application of the triangle inequality with $I_n(b) > 0$ for $b > 0$. The modified Bessel function series gives

$$\sum_{n=-\infty}^{\infty} b(1+\sqrt{\pi}e^{\mathrm{Im}(u)^2})\left(I_{n-1}(b)+I_{n+1}(b)\right)e^{-b} = 2b(1+\sqrt{\pi}e^{y_0^2}) < \infty.$$

The Weierstrass M-test therefore guarantees uniform convergence of the series. The analyticity of H in D follows directly from the uniform convergence of its series definition. □

The contour deformation is justified since $\phi_{\mathbf{k}}(p)$ can be expressed as:

$$\frac{e\phi_{\mathbf{k}}}{T_e}(p) = \frac{\frac{A_0}{i\sqrt{2}k_{\parallel}\rho_i}F\left(\frac{ip/\Omega_i}{\sqrt{2}k_{\parallel}\rho_i};a,b\right)}{1-\frac{\theta}{2}G\left(\frac{ip/\Omega_i}{\sqrt{2}k_{\parallel}\rho_i};a,b\right)-\frac{\theta}{\sqrt{2}k_{\parallel}\rho_i}H\left(\frac{ip/\Omega_i}{\sqrt{2}k_{\parallel}\rho_i};a,b\right)},$$

taking the parameters to be $a = \frac{1}{\sqrt{2}k_{\parallel}\rho_i}$ and $b = k_{\perp}^2\rho_i^2$. Since the proofs in Theorems A.1 and A.2 apply to an arbitrarily large portion of the complex plane, we consider in particular the domain $D' = \{p \in \mathbb{C} : -R_0 \leq \mathrm{Re}(p) \leq R_0\}$, where R_0 is chosen such that $R_0 > \max(\alpha, \sigma)$, as illustrated in Figure A.1. Then $D'/\{p_j\}$ defines a domain in which the contour of Figure 4.1 a) can be continuously deformed into that of Figure 4.1 b), without crossing any singularities of $\phi_{\mathbf{k}}$.

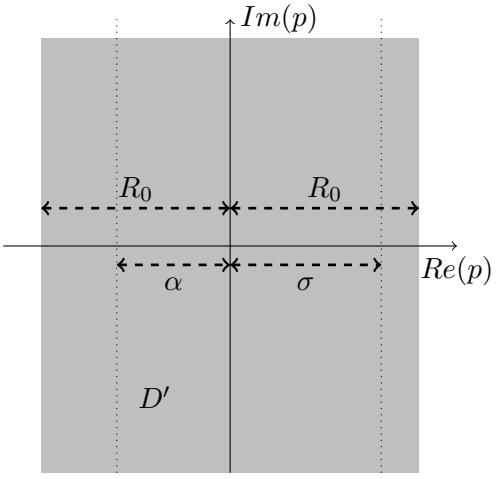

Figure A.1: The domain $D' = \{p \in \mathbb{C} : -R_0 < \mathrm{Re}(p) < R_0\}$, where $R_0 > \max(\alpha, \sigma)$.

Appendix B

A Brief Overview of Discrete Variational Mechanics

Here, we derive the discrete Euler-Lagrange equations, which provides the foundation for the integrator used for the equilibrium orbits in Chapter 5. The derivation is along the same lines as that of the continuous theory. Similar derivations can be found in a number of references including [77] [80].

B.1 Discrete Euler-Lagrange Equations

Beginning with a Lagrangian $\mathcal{L}$ given as a function of generalized coordinates $q = (q_1, q_2, ..., q_N)$ and generalized velocities $\dot{q} = (\dot{q_1}, \dot{q_2}, ..., \dot{q_N})$, we assume a setting in which time is discretized uniformly by Δt. We denote the generalized coordinates and generalized velocities at time $t = \nu \Delta t$ by q^ν and $\dot{q}^\nu$ respectively and define a discrete Lagrangian, $\mathcal{L}_d$, to be an approximation of the time integral of $\mathcal{L}$ between two discrete time points, i.e.

$$\mathcal{L}_d(q^\nu, q^{\nu+1}) \approx \int_{t^\nu}^{t^{\nu+1}} \mathcal{L}(q, \dot{q}) dt, \tag{B.1}$$

where some quadrature rule is used in the approximation. There is some flexibility in how the right hand side is approximated, with these choices determining the form of $\mathcal{L}_d$ and the resulting integration scheme. It is typical to approximate $\dot{q}$ by

$$\dot{q} \approx \frac{q^{\nu+1} - q^\nu}{\Delta t} \qquad \text{for} \qquad t \in [\nu \Delta t, (\nu + 1)\Delta t] \,.$$

With this approximation, common choices for the quadrature in Eq.(B.1) include the trapezoidal rule, for which

$$\mathcal{L}_d(q^\nu, q^{\nu+1}) = \frac{\Delta t}{2}\mathcal{L}\left(q^\nu, \frac{q^{\nu+1}-q^\nu}{\Delta t}\right) + \frac{\Delta t}{2}\mathcal{L}\left(q^{\nu+1}, \frac{q^{\nu+1}-q^\nu}{\Delta t}\right)$$

or the midpoint rule, yielding

$$\mathcal{L}_d(q^\nu, q^{\nu+1}) = \Delta t\mathcal{L}\left(\frac{q^\nu+q^{\nu+1}}{2}, \frac{q^{\nu+1}-q^\nu}{\Delta t}\right).$$

In what follows, we assume that the approximation used in Eq.(B.1) depends only on the generalized coordinates from two time steps $(q^\nu, q^{\nu+1})$, but otherwise do not specify the form. Next, we define the discrete action over the interval $t \in [0, N\Delta t]$ to be a sum of discrete Lagrangians as

$$S_d = \sum_{\nu=0}^{N-1} \mathcal{L}_d(q^\nu, q^{\nu+1}). \tag{B.2}$$

In analogy with Hamilton's principle in continuous Lagrangian mechanics, we assume specified states at times t_0 and t_N and require the discrete time trajectory $\{q^\nu\}_{\nu=0}^N$ to be such that the variation in the discrete action vanishes. Taking the variation of Eq.(B.2), we have

$$\delta S_d = \delta \sum_{\nu=0}^{N-1} \mathcal{L}_d(q^\nu, q^{\nu+1}) = \sum_{\nu=0}^{N-1}\left[\frac{\partial}{\partial q^\nu}\mathcal{L}_d(q^\nu, q^{\nu+1})\cdot\delta q^\nu + \frac{\partial}{\partial q^{\nu+1}}\mathcal{L}_d(q^\nu, q^{\nu+1})\cdot\delta q^{\nu+1}\right].$$

Setting δS_d equal to zero and noting that $\delta q^0 = \delta q^N = 0$, we have

$$\sum_{\nu=1}^{N-1}\frac{\partial}{\partial q^\nu}\mathcal{L}_d(q^\nu, q^{\nu+1})\cdot\delta q^\nu + \sum_{\nu=0}^{N-2}\frac{\partial}{\partial q^{\nu+1}}\mathcal{L}_d(q^\nu, q^{\nu+1})\cdot\delta q^{\nu+1} = 0.$$

A shift of index in the second summation yields

$$\sum_{\nu=1}^{N-1}\frac{\partial}{\partial q^\nu}\left[\mathcal{L}_d(q^\nu, q^{\nu+1}) + \mathcal{L}_d(q^{\nu-1}, q^\nu)\right]\cdot\delta q^\nu = 0. \tag{B.3}$$

Since Eq.(B.3) holds for any variation in the trajectory, it follows that

$$\frac{\partial}{\partial q^\nu}\left[\mathcal{L}_d(q^\nu, q^{\nu+1}) + \mathcal{L}_d(q^{\nu-1}, q^\nu)\right] = 0, \tag{B.4}$$

which is the discrete analog of the Euler-Lagrange equations.

B.2 Position-Momentum Form

An equivalent form of Eq.(B.4) which has analogies to the Hamiltonian formulation of mechanics is obtained by defining the discrete momentum by

$$p^{\nu} = -\frac{\partial}{\partial q^{\nu}}\mathcal{L}_d(q^{\nu}, q^{\nu+1}) = \frac{\partial}{\partial q^{\nu}}\mathcal{L}_d(q^{\nu-1}, q^{\nu}).$$

Equation (B.4) can then be expressed in the position-momentum form as

$$p^{\nu} = -\frac{\partial}{\partial q^{\nu}}\mathcal{L}_d(q^{\nu}, q^{\nu+1}) \tag{B.5}$$

$$p^{\nu+1} = \frac{\partial}{\partial q^{\nu+1}}\mathcal{L}_d(q^{\nu}, q^{\nu+1}). \tag{B.6}$$

Assuming (q^{ν}, p^{ν}) are given, Eq.(B.5) is first solved to obtain $q^{\nu+1}$, after which $p^{\nu+1}$ can be obtained simply by plugging into Eq.(B.6). The position-momentum form provides the starting point for the integration scheme presented in Chapter 5.

Appendix C

Linearization of the δf Method

To linearize the δf method, we let ϵ be a parameter representing the perturbation size at $t = 0$. For example, ϵ may be present in an initial condition as

$$w_p(t = 0) = \epsilon g(\mathbf{x}_p(t = 0), \mathbf{v}_p(t = 0)).$$

where $g(\mathbf{x}, \mathbf{v}) \sim O(1)$. We assume that all quantities in the model are analytic in ϵ around the unperturbed system and denote the ϵ dependence of a time dependent quantity by $\psi(t; \epsilon)$. The unperturbed system, corresponding to $\epsilon = 0$, is given by

$$\mathbf{E}_j(t; 0) = \mathbf{0}, \qquad \delta n_j(t; 0) = 0, \qquad w_p(t; 0) = 0, \qquad \mathbf{v}_p(t; 0) = \mathbf{v}_p^{(0)}, \qquad \mathbf{x}_p(t; 0) = \mathbf{x}_p^{(0)}(t).$$

This allows an expansion in ϵ as

$$\begin{aligned}
\mathbf{E}_j(t; \epsilon) &= \epsilon \mathbf{E}_j^{(1)}(t) + ... \\
\delta n_j(t; \epsilon) &= \epsilon \delta n_j^{(1)}(t) + ... \\
w_p(t; \epsilon) &= \epsilon w_p^{(1)}(t) + ... \\
\mathbf{v}_p(t; \epsilon) &= \mathbf{v}_p^{(0)} + \epsilon \mathbf{v}_p^{(1)}(t) + ... \\
\mathbf{x}_p(t; \epsilon) &= \mathbf{x}_p^{(0)}(t) + \epsilon \mathbf{x}_p^{(1)}(t) + ...
\end{aligned} \tag{C.1}$$

We note that for a quantity $\psi(t; \epsilon)$ to be accurately approximated as

$$\psi(t;\epsilon) \approx \psi^{(0)}(t) + \epsilon\psi^{(1)}(t),$$

it is necessary that $\epsilon^m \psi^{(m)}(t) \ll \psi^{(0)}(t) + \epsilon\psi^{(1)}(t)$ for all $m \geq 2$. This requirement, however, is not guaranteed to hold uniformly in time for the linearized model. The linearized model, therefore, should only be expected to accurately model the behavior of the nonlinear system on short time scales after a small perturbation.

Proceeding with the expansion in Eq.(C.1), we compute the perturbed number density at grid point $\mathbf{X}_j$ from Eq.(6.7), including terms to $O(\epsilon)$. We have

$$\delta n_j(t;\epsilon) = \frac{N_i}{\Delta V N_p} \sum_{p=1}^{N_p} w_p(t;\epsilon) S_{\mathbf{x}}(\mathbf{X}_j - \mathbf{x}_p(t;\epsilon)) = \epsilon \frac{N_i}{\Delta V N_p} \sum_{p=1}^{N_p} w_p^{(1)}(t) S_{\mathbf{x}}(\mathbf{X}_j - \mathbf{x}_p^{(0)}(t)) + O(\epsilon^2),$$

yielding

$$\delta n_j^{(1)}(t) = \frac{N_i}{\Delta V N_p} \sum_{p=1}^{N_p} w_p^{(1)}(t) S_{\mathbf{x}}(\mathbf{X}_j - \mathbf{x}_p^{(0)}(t)). \tag{C.2}$$

Next, to compute $w_p^{(1)}(t)$, we plug Eq.(C.1) into the nonlinear particle weight equation Eq.(6.5) and expand to $O(\epsilon)$. This gives

$$\frac{dw_p^{(1)}(t)}{dt} = -\frac{e}{m_i} \mathbf{E}^{(1)}(\mathbf{x}_p^{(0)}(t), t) \cdot \nabla_{\mathbf{v}_p^{(0)}} \ln f_0(\mathbf{v}_p^{(0)}), \tag{C.3}$$

where $\mathbf{E}^{(1)}(\mathbf{x}_p^{(0)}(t), t)$ is the $O(\epsilon)$ term of the interpolated electric field

$$\mathbf{E}^{(1)}(\mathbf{x}_p^{(0)}(t), t) = \sum_j \mathbf{E}_j^{(1)}(t) S_{\mathbf{x}}(\mathbf{X}_j - \mathbf{x}_p^{(0)}(t)).$$

We note that Eq.(C.2) and Eq.(C.3) require only the computation of the unperturbed particle orbits. This is in contrast to the linearization of the full-f method, which requires the first order perturbations of the particle orbits. Plugging Eq.(C.1) into Eq.(6.2), we have for the unperturbed particle orbits, simply,

$$\frac{d\mathbf{x}_p^{(0)}(t)}{dt} = \mathbf{v}_p^{(0)}$$
$$\frac{d\mathbf{v}_p^{(0)}}{dt} = 0.$$

Finally, for the first order electric field at grid point $\mathbf{X}_j$, we plug Eq.(C.1) into a discretized version of Eq.(6.13). This yields

$$\mathbf{E}_j^{(1)}(t) = \frac{T_e}{en_0}\mathbf{D}\delta n_j^{(1)}(t),$$

where $\mathbf{D}$ is a discrete gradient operator.

Appendix D

Initialization

In our tests of numerical stability, an initial condition of the form

$$f(x, v, t = 0) = \left(1 + \frac{\delta n^{(1)}(x, t = 0)}{n_0}\right) f_0(v) \tag{D.1}$$

is used for both the δf and full-f PIC simulations, where $\delta n^{(1)}(x, t = 0)$ is chosen to excite each non-zero wave number in the DFT with a finite perturbation. To initialize the perturbed density such that the DFT is approximately constant across the non-zero wave numbers, the filtering due to the shape function must be accounted for. To counter this effect, a Fourier filter $H(k)$ is used with the FS of the initial condition. The filter defined by:

$$H(k) = \begin{cases} \frac{1}{S(k)} & : \quad k \in (-\frac{\pi}{\Delta x}, \frac{\pi}{\Delta x}] \setminus \{0\} \\ 0 & : \quad k \in (-\infty, -\frac{\pi}{\Delta x}] \cup \{0\} \cup (\frac{\pi}{\Delta x}, \infty) \end{cases}$$

works well for this purpose.

D.1 δf initialization

For the linear δf simulations, the initial density perturbation is chosen as

$$\delta n^{(1)}(x, t = 0) = A \; n_0 \; \mathrm{Re}\left\{\sum_k H(k) e^{ikx}\right\}.$$

where A is the amplitude at which we wish to excite the DFT modes. Notice from D.1, we have

$$\frac{\delta f(x, v, t = 0)}{f_0(v)} = \frac{\delta n^{(1)}(x, t = 0)}{n_0}.$$

Therefore to implement this initial condition for the linear δf simulations, the unperturbed particle positions $x_p^{(0)}$ are loaded uniformly in space and the particle weights are initialized by

$$w_p^{(1)}(t=0) = A \text{ Re}\left\{\sum_k H(k) e^{ikx_p^{(0)}(t=0)}\right\}.$$

D.2 Full-f initialization

For the linear full-f simulations, the initial density perturbation is related to the perturbed particle positions through

$$\delta n^{(1)}(x, t=0) = -\frac{\partial P^{(1)}(x, t=0)}{\partial x},$$

where

$$P^{(1)}(x, t=0) = \int_{-\infty}^{\infty} x^{(1)}(x, v, t=0) f_0(v) dv.$$

By choosing $x^{(1)}$ to be independent of v at $t = 0$, this is simply

$$P^{(1)}(x, t=0) = n_0 \; x^{(1)}(x, t=0).$$

The initial particle position perturbation is taken as

$$x^{(1)}(x, t=0) = A \text{ Re}\left\{\sum_{k\neq 0} \frac{iH(k)}{k} e^{ikx}\right\},$$

and the initial particle velocity perturbation is taken as zero. To implement this initial condition then, the unperturbed particle positions $x_p^{(0)}$ are loaded uniformly in space, and the perturbed particle data is initialized by

$$x_p^{(1)}(t=0) = A \text{ Re}\left\{\sum_{k\neq 0} \frac{iH(k)}{k} e^{ikx_p^{(0)}(t=0)}\right\},$$

and

$$v_p^{(1)}(t=0) = 0.$$